DISSERTATION

CHANGES IN SHORTWAVE SOLAR RADIATION UNDER LOCAL AND TRANSPORTED WILDFIRE SMOKE PLUMES: IMPLICATIONS FOR AGRICULTURE, SOLAR ENERGY, AND AIR QUALITY APPLICATIONS

Submitted by

Kimberley A. Corwin

Department of Atmospheric Science

In partial fulfillment of the requirements

For the Degree of Doctor of Philosophy

Colorado State University

Fort Collins, Colorado

Summer 2024

Doctoral Committee:

Advisor: Emily Fischer

Jeffrey Pierce
Christine Chiu
Chelsea Corr-Limoges
Jesse Burkhardt

ABSTRACT

CHANGES IN SHORTWAVE SOLAR RADIATION UNDER LOCAL AND TRANSPORTED WILDFIRE SMOKE PLUMES: IMPLICATIONS FOR AGRICULTURE, SOLAR ENERGY, AND AIR QUALITY APPLICATIONS

The emission and transport of pollutants from wildfires is well-documented, particularly at the surface. However, smoke throughout the atmospheric column affects incoming shortwave solar radiation with potentially wide-ranging consequences. By absorbing and scattering light, smoke changes the amount and characteristics of shortwave radiation–a resource that controls plant photosynthesis, solar energy generation, and atmospheric photochemical reactions. In turn, these influence ecological systems as well as air quality and human health. This dissertation examines how wildfire smoke alters boundary layer and surface-level shortwave radiation in ways that are relevant for agricultural, energy, and air quality applications.

First, I present an analysis of smoke frequency and smoke-driven changes in the total and diffuse fraction (DF) of photosynthetically active radiation (PAR; 400-700 nm) at the surface. I compare PAR and PAR DF on smoke-impacted and smoke-free days during the agricultural growing season from 2006 to 2020 using data from 10 ground-based radiation monitors and satellite-derived smoke plume locations. I show that, on average, 20% of growing season days are smoke-impacted and that smoke prevalence has increased over time ($r = 0.60$, $p < 0.05$). Smoke frequency peaks in the mid to late growing season (i.e., July, August), particularly over the northern Rocky Mountains, Great Plains, and Midwest. I find an increase in the distribution of PAR DF on smoke-impacted days, with larger increases at lower cloud fractions. On clear-sky days, daily average PAR DF increases by 10 percentage points when smoke is present. Spectral

analysis of clear-sky days shows smoke increases DF (average: +45%) and decreases total irradiance (average: −6%) across six wavelengths measured from 368 to 870 nm. Optical depth measurements from ground and satellite observations both indicate that spectral DF increases and total spectral irradiance decreases with increasing smoke plume optical depth. My analysis provides a foundation for understanding smoke's impact on PAR, which carries implications for agricultural crop productivity under a changing climate.

Second, I examine smoke's impact on two key measures used to assess a location's baseline solar resource availability for solar energy production: direct normal (DNI) and global horizontal (GHI) irradiance. I quantify smoke-driven changes in DNI and GHI at different spatial and temporal scales across the contiguous U.S. (CONUS) using radiative transfer model output and satellite-based smoke, aerosol, and cloud observations. Importantly, I expand the scale of previous studies on smoke and solar energy by including areas primarily affected by dilute, aged, transported smoke plumes in addition to areas with dense, fresh, local smoke plumes. I show that DNI and GHI decrease as smoke frequency increases at the state, regional, and national scale. DNI is more sensitive to smoke with sizable losses persisting downwind of fires. Although large reductions in GHI are possible close to fires, mean GHI declines minimally (< 5%) due to transported smoke. Overall, GHI–the main resource used for photovoltaic energy production–remains a relatively stable resource across most of CONUS even in extreme fire seasons, which is promising given U.S. solar energy goals.

Third, I investigate smoke-driven changes in surface-level and boundary layer downwelling actinic flux (F↓)–a crucial component of determining the rate of photooxidation in the atmosphere. I present a case study of changes in F↓ at 550 nm (process validation) and 380 nm (NO_2 photolysis) along a research flight through the California Central Valley during the

2018 Western Wildfire Experiment for Cloud Chemistry, Aerosol Absorption, and Nitrogen (WE-CAN) aircraft campaign. F↓ was measured onboard via the HIAPER Airborne Radiation Package (HARP), and I use the National Center for Atmospheric Research (NCAR) Tropospheric Ultraviolet and Visible (TUV) Radiation Model to compute F↓ under smoke-free and smoke-impacted conditions. Modeling F↓ with TUV facilitates calculating the change in F↓ and provides a means of assessing F↓ at altitudes not sampled by the aircraft, such as the ground. I find that the smoke-impacted F↓ from TUV aligns closely with HARP observations: all modeled fluxes are within 20% of measurements at 550 nm and 85% are within 20% of measurements at 380 nm. The average modeled-to-measured ratios ($\bar{F}\downarrow_{550}$=0.96; $\bar{F}\downarrow_{380}$=0.89) indicate that TUV minorly underestimates the observed F↓. On average, observed $F\downarrow_{380}$ decreased 26%, 17%, and 9% at 0-0.5 km, 0.5-1 km, and 1-1.5 km, respectively, while TUV estimates larger reductions of 41%, 26%, and 19% at the same altitudes. At the ground-level, I calculate a 47% decrease in $F\downarrow_{380}$ using TUV, which is likely an upper bound given the model slightly underestimates observations. As wildfire smoke increases with climate change, understanding how smoke aloft changes photochemistry is increasingly important for constraining future air quality.

ACKNOWLEDGEMENTS

I would like to thank my advisor Dr. Emily Fischer for her constant support over the last four years. You never wavered in encouraging me and believing that I could make it to this finish line. Thank you for always challenging me to become a better scientist and a more effective researcher and communicator. Thank you especially for teaching me to keep move forward when I'm stuck in the weeds and looking for perfection. Sometimes we all need a guide to find the big picture again. I feel so fortunate for the opportunity to learn from and collaborate with you. Additionally, I would like to thank all my former advisors for setting me on an incredible foundation for becoming a scientist: Drs. Britt Argow, Jean-Daniel Stanley, and Brittany Brand. You all taught me how to be a scientist and how to communicate my research effectively. Emily, Brittany, and Britt: you taught me to be a strong woman in science, to advocate for myself, and to strive to make science more welcoming for others. Jean-Daniel: you taught me about balance in life, the difference between vocation and avocation, and that where you start doesn't dictate the destination. For these reasons and so much more, I'm forever grateful to all of you and your incredible mentorship.

I would also like to thank my committee members Drs. Jeffrey Pierce, Christine Chiu, Chelsea Corr-Limoges, and Jesse Burkhardt as well as my co-authors Drs. Paul Stackhouse, Amit Munshi, Sam Hall, and Kirk Ullman. I appreciate your mentorship and all your help in strengthening my research and this dissertation.

Finally, thank you to my family and friends for your support on this journey. I couldn't have done it without you all being there to listen, commiserate, and cheer me on over the years.

Most of all, I'd like to thank my partner Dr. Joshua Hewitt for being my favorite companion and always believing in me even when I faltered. Your steadiness and support mean the world to me.

The following acknowledgements are adapted from the individual articles presented in Chapters 2-4. The research in Chapters 2 and 3 was based upon work supported by the National Science Foundation under Grant 1828902. Additionally, for Chapter 2, I would like to thank the UVMRP program director Dr. Wei Gao, Becky Olson, and the rest of the UVMRP staff (https://uvb.nrel.colostate.edu/UVB/) for maintaining the UVMRP instrument network and database as well as for assisting with data retrieval. Thank you to Drs. Jeffrey R. Pierce and J. Christine Chiu for advice on data products and subject matter expertise, and thanks to Dr. Joshua Hewitt for statistical discussions. The research in Chapters 3 and 4 was supported by the Future Investigators in NASA Earth and Space Science and Technology (FINESST) award under Grant 80NSSC22K1539. Additional funding for the work in Chapter 4 was provided by the US National Science Foundation (NSF award numbers: AGS-1650786, AGS-1650275, AGS-1950327, and AGS-1652688) and the US National Oceanic and Atmospheric Administration (NOAA) under award number NA17OAR4310010. This material is based upon work supported by the National Center for Atmospheric Research, which is a major facility sponsored by the National Science Foundation under Cooperative Agreement No. 1852977.

DEDICATION

I would like to dedicate this dissertation to my grandfather, Frederick J. Brown (1919-2020) who always taught me to "keep up the good work" and, most importantly, to "keep smilin'!"

TABLE OF CONTENTS

CHAPTER 1

INTRODUCTION[1]

1.1 INTRODUCTION TO WESTERN U.S. WILDFIRES SMOKE EMISSIONS

Historically, the United States (U.S.) wildfire season ranges from April through September, starting first in the Southwestern states of Arizona and New Mexico before shifting north into California, and eventually reaching Oregon, Washington, Idaho, and Montana (Westerling et al., 2003). Since the mid-1980s, higher spring and summer temperatures, earlier snowmelt, and increased fuel aridity are extending wildfire seasons and leading to longer-burning fires with larger burn areas (Abatzoglou & Williams, 2016; Westerling, 2016; Westerling et al., 2006). U.S. wildfire activity initially increased mainly in the forested Northern Rocky Mountains (Westerling et al., 2006), but much of the recent growth has occurred in the Pacific Northwest and Southwest (Westerling, 2016). Continued increases in fire weather days are projected to be emblematic of future wildfire conditions in the U.S. and globally (Abatzoglou et al., 2021; Higuera & Abatzoglou, 2021).

The growth in wildfire activity has also resulted in increased wildfire smoke emissions (Ford et al., 2018; Yue et al., 2013) that are causing measurable changes in atmospheric properties over the U.S. (Buchholz et al., 2022; e.g., Xue et al., 2021). For example, near the surface, fine particulate matter ($PM_{2.5}$) attributable to anthropogenic sources is declining over the U.S. due to regulations that have substantially reduced anthropogenic emissions over the last three decades (Ridley et al., 2018; 2017, 2019). At the same time, studies of surface $PM_{2.5}$ concentrations show that wildfire smoke emissions are offsetting the reductions in $PM_{2.5}$ caused

[1] Adapted from the introductions of the three journal articles presented in Chapters 2-4 of this dissertation. See individual chapters for full citations (Corwin et al., 2022, *JGR*; Corwin et al., under review, *Nature Comm*; Corwin et al., in prep, *JGR*).

by declining anthropogenic emissions, particularly in the Pacific Northwest (McClure & Jaffe, 2018; O'Dell et al., 2019). Future projections of $PM_{2.5}$ support climate-driven wildfire emissions becoming the dominant source of summertime $PM_{2.5}$ in the western U.S. during the 21st century (Ford et al., 2018; Val Martin et al., 2015). Accounting for population change—which influences land use, fire suppression, and human-caused fire ignitions—Ford et al. (2018) estimate that over half the total $PM_{2.5}$ across the contiguous U.S. (CONUS) will stem from wildfire emissions by 2100 under two climate scenarios (RCP4.5 and RCP8.5). Recent studies of aerosol optical depth (AOD), which accounts for aerosols throughout the atmospheric column, indicate similar trends (e.g., Hallar et al., 2017; McClure & Jaffe, 2018).

Existing smoke climatologies show that wildfire smoke from the western U.S. travels far from active fire sources to affect the atmospheric column and air quality nationally (Brey et al., 2018; Kaulfus et al., 2017; O'Dell et al., 2021). Brey et al. (2018) provide a detailed smoke climatology for North America from 2007-2014. The three largest smoke-producing regions in the U.S. are the Northwest, Southwest, and Rocky Mountains. Smoke from these regions is almost exclusively from wildland fires. Combined, these three regions along with western Canadian provinces are the major contributors to smoke over the Great Plains, Midwest, Southern Plains, Northeast, and Mid-Atlantic. The Southeast, on the other hand, is primarily affected by locally-derived smoke. Despite documenting the widespread reach of wildfire smoke, existing smoke climatologies were compiled prior to the severe North American wildfire seasons of 2018, 2020, 2021, and 2023 (Brey et al., 2018; Kaulfus et al., 2017). The increasing abundance and far reaching transport of such smoke motivates a need to understand not only how local, surface-level smoke affects human systems, but also how transported smoke aloft can affect society, particularly given recent extreme wildfire seasons.

1.2 Introduction to Smoke-Radiation Interactions

Significant research is directed toward understanding how aerosols impact radiative transfer, especially given the climate implications associated with large uncertainties in aerosol radiative forcing (Forster et al., 2007). Aerosols influence the Earth system directly by scattering and absorbing radiation as well as indirectly by modulating the properties and evolution of clouds. These direct and indirect interactions determine the magnitude of cooling (i.e., negative forcing) attributable to aerosols in the climate system. In addition to climate impacts, aerosol-radiation interactions influence any system that relies on light as a primary resource, including agriculture, energy production, and air quality.

In this dissertation, I focus on how absorption and scattering by wildfire smoke changes direct, diffuse, and total downwelling radiation. Direct beam radiation travels from the top of the atmosphere to the surface without being scattered, and when perpendicular to a surface, is referred to as the Direct Normal Irradiance (DNI). Diffuse radiation, or Diffuse Horizontal Irradiance (DHI), refers to the light scattered by air molecules, aerosols, and cloud droplets in the atmosphere (Petty, 2006). Combined, the direct and diffuse components comprise the total irradiance, or Global Horizontal Irradiance (GHI). While absorption decreases total downwelling irradiance, scattering changes the ratio of direct-to-diffuse irradiance by increasing the diffuse fraction (DF). Scattering can also reduce downwelling irradiance by increasing reflectance to space. Changes to the total and DF of light also affects actinic flux, which describes the flux of photons through a point in the atmosphere from any direction and drives the rate of photolytic reactions (Madronich & Flocke, 1999). More details on each of these measures will be discussed in the relevant chapters.

Optical properties typically used to describe aerosol-radiation interactions include the refractive index, single scattering albedo (SSA), scattering phase function (P (cos Θ), where Θ is the scattering angle), Angstrom exponent (α), and aerosol optical depth (AOD) (Liou, 2002; Petty, 2006). The refractive index is a complex number that describes the absorbing (imaginary) and scattering (real) nature of a particle or molecule. The SSA and phase function describe the scattering behavior, indicating the ratio of scattering to total extinction and the angular distribution of scattering, respectively. The spectral dependence of extinction is described by α, which can be used as an indication of aerosol particle size. AOD is a measure of column-total extinction at a specific wavelength and depends on the refractive index and size distribution of aerosols. Importantly, optical properties vary by wavelength, aerosol species, atmospheric conditions, and emission conditions.

Carbonaceous aerosols, particularly light-absorbing organic (brown) carbon, result in wildfire smoke exhibiting a spectral dependence that favors stronger absorption at shorter wavelengths (e.g., in the ultraviolet (UV) spectral region) and weaker absorption at longer wavelengths (Kirchstetter et al., 2004; Lewis et al., 2008). The extent of spectral dependence varies based on the proportion of black carbon, brown carbon, and inorganic aerosols such as SO_4 present in the smoke (Bian et al., 2020; Lewis et al., 2008; Y. H. Park et al., 2020). Smoke aerosol composition depends on a wide range of factors that influence smoke's physical and optical properties, including differences in fire regime (flaming vs. smoldering), meteorological conditions (e.g., relative humidity), fuel composition, environmental conditions, and plume age and transport (Alonso-Blanco et al., 2014; Bian et al., 2020; Chakrabarty et al., 2023; Corr et al., 2012; He & Carmichael, 1999; Hodshire, Akherati, et al., 2019; Hodshire, Bian, et al., 2019; Y. H. Park et al., 2020; Ramnarine et al., 2019; Reid et al., 2005). For example, Bian et al. (2020)

characterized smoke composition and optical properties across the U.S. using ground-based observations, determining that smoke in the Pacific Northwest and Southwest regions is more absorbing and less scattering than smoke in the Southeast. Bian et al. attribute the increased scattering in the Southeast to higher relative humidity and SO_4 fractions leading to hygroscopic growth. Also, black carbon fractions are likely lower in the Southeast where smoldering fires and prescribed burns dominate as opposed to the flaming wildfire conditions prevalent in the West. Additionally, SSA on smoke-impacted days can vary due to changes in the dust fraction and aerosol size distribution. In terms of spectral dependence, mean SSA decreases with increasing wavelength in the Pacific Northwest and Southwest, but in the Southeast, mean SSA decreases with increasing wavelength in the visible and increases with increasing wavelength in the near infrared. The range of variability in smoke optical properties carries important implications for studying the radiative impacts of smoke. As such, my goal with this dissertation is to explore smoke-radiation interactions across longer temporal and larger spatial scales to incorporate a diverse range of smoke properties. I focus mainly on the longwave ultraviolet (UV) and visible portions of the solar spectrum, which are strongly affected by wildfire smoke and of particular importance for photosynthesis, solar energy, and atmospheric oxidation processes.

1.3 Introduction to Implications of Shortwave Radiation Changes

Although an extensive body of literature focuses on the health impacts of smoke emissions and transport, smoke's impact on human systems via changes to the amount and characteristics of shortwave radiation remains understudied. Shortwave radiation is a resource that controls plant photosynthesis, solar energy generation, and atmospheric photochemical reactions, which influence food and energy systems as well as air quality and human health.

1.3.1 Plant Productivity

Plant health depends on the total and DF of photosynthetically active radiation (PAR; 400-700 nm), which plants use for photosynthesis. Studies of aerosol impacts on various ecosystems indicate that plant productivity can improve due to increased radiation use efficiency (Kanniah et al., 2012) under elevated PAR DF, as long as extreme declines in total PAR are avoided. Knohl and Baldocchi (2008) leveraged observations from a forest in Germany and a canopy process model to show that photosynthesis improves with increasing DF and reaches an optimum level when the diffuse component is 45% of the total. At higher DFs, aerosols can substantially reduce total PAR and negate or overwhelm the photosynthetic benefits resulting from increased DF. To investigate similar effects in crops, Greenwald et al. (2006) used radiative transfer and crop yield models to simulate maize, wheat, and rice yields under different aerosol loadings. Results showed that aerosol impacts on crop yields varied depending on cloud conditions. Total PAR decreased with the addition of aerosol on both clear and overcast days, but DF only increased meaningfully under clear-sky conditions. Simulations of locations with infrequent cloud cover, like California's Central Valley, showed improvements in plant radiation use efficiency with aerosols. Similarly, Schiferl and Heald (2018) modeled the potential global effects of PM and ozone on maize, rice, and wheat crops under present-day (2010) and future (2050) conditions. Simulations suggested that the beneficial effects of PM on DF counteract much of ozone's detrimental effects on plants and that declining anthropogenic emissions due to improved pollution controls may negatively impact crops in areas with historically high PM.

Recently, studies focusing on wildfire smoke have demonstrated similar impacts during individual wildfire seasons. McKendry et al. (2019) examined changes in carbon fluxes associated with radiation changes due to a 2015 wildfire smoke event in southwestern British

Columbia, Canada. Plant productivity and photosynthesis increased at a coniferous forest site and a wetland site under smoke with AOD ≤ 2. However, when smoke became too optically dense the forested site, which had a more complex canopy system experienced reductions in productivity. Hemes et al. (2020) studied how agricultural and wetland plant productivity in California's Central Valley varied between a low and high smoke year using eddy covariance measurements and empirical modeling. In this case study, the increase in PAR DF due to wildfire smoke resulted in a near doubling of the efficiency with which plants used the available light. Ecosystem productivity increased by 1.2-4.2%, but productivity depended on how much PAR DF increased relative to the reduction in total PAR. Despite the evidence of benefits to plant productivity from smoke-driven increases in PAR DF, questions remained as to the degree to which smoke affects total and PAR DF over larger areas and longer time frames. I work to quantify these changes over larger scales in Chapter 2 of this dissertation.

1.3.2 Solar Energy

DNI and GHI are used to assess the solar resource potential for concentrating solar-thermal power (CSP) and photovoltaic (PV) power production. PV installations provide the bulk of U.S. solar energy, and the response of PV panel technologies to diffuse light varies (Munshi et al., 2018). Peak spectral responsivity of PV panels ranges from the ultraviolet to the near-infrared (< 1200 nm) and is primarily centered in the visible range (Dirnberger et al., 2015; Field, 1997), meaning there is overlap between panel and wildfire smoke spectral curves.

Previous research on aerosols and PV generation focused on anthropogenic pollution and dust, and demonstrated that $PM_{2.5}$ reduces PV generation via atmospheric attenuation and panel soiling. Li et al. (2017) showed an annual average (peak) decline of 20-25% (34%) in point-of-array irradiance across northern and eastern China due to attenuation by air pollution. Li et al.

(2020) concluded that PM reduces PV output by over 50% in heavily polluted and desert regions around the world, but identified soiling as being responsible for over two-thirds of lost output. In some regions, the impact of PM on PV capacity factors is similar to the impact of clouds (Li et al., 2020). Research on dust's detrimental effects on PV technologies is extensive and spans nearly seventy years (Sarver et al., 2013). Yet, wildfire smoke, air pollution, and dust interact differently with solar radiation due to variations in absorption and scattering behaviors.

Recent studies have linked lower PV output to wildfire smoke in specific case studies. Perry and Troccoli (2015) found that average (peak) PV output decreased 7% (27%) at a solar lab in Canberra, Australia on a clear-sky afternoon when smoke from a controlled burn (AOD 0.25) drifted overhead. Gómez-Amo et al. (2019) calculated an 34% average decline in PV output over two smoke-impacted days in Valencia, Spain. Donaldson et al. (2021) estimated that PV capacity declined 9-11% at an AOD of 0.5, 29-30% at an AOD 2.5, and 37-50% at an AOD of 4.5 at ten southern California sites during the 2020 wildfire season. While demonstrating the scale of smoke impacts on PV output, the first two studies examined only a single fire event, solar plant, and location, while the third was limited geographically and to conditions during a record-breaking wildfire season. Generalizing these findings will require knowing how PV output varies with plume number, extent, timing, and thickness; PV panel configurations and materials; fuel composition; and local meteorology. In Chapter 3 of this dissertation, I focus on extending the scale of analyses of smoke impacts on solar resources to include multiple wildfires seasons and regions, inherently incorporating a diverse set of smoke plumes.

1.3.3 Air Quality

Changes in actinic flux impact the rate of photooxidation in the atmosphere, which controls the formation and destruction of many atmospheric pollutants. Smoke has been shown

to reduce photolysis rates (Lill et al., 2022) and increase NO_2 lifetimes (Lindaas et al., 2017), both features consistent with smoke-driven reductions in actinic flux. The change in actinic flux driven by smoke can vary throughout the day with evidence of NO_2 photolysis decreasing at high solar zenith angles (low sun) and increasing at low solar zenith angles (high sun) due to greater scattering (Baylon et al., 2018). As noted above, such changes also depend on the aerosol properties. Changes in NO_2 photolysis are important for controlling NO_x levels and the tropospheric ozone cycle, two criteria pollutants that cause adverse health effects (e.g., Nuvolone et al., 2018). In Chapter 4 of this dissertation, I aim to provide greater detail on how smoke changes surface-level and near-surface actinic flux given direct observations throughout the boundary layer.

1.4 Overview of Dissertation Chapters and Goals

This dissertation advances our understanding of how wildfire smoke alters boundary layer and surface-level shortwave radiation in ways that are relevant for agricultural, energy, and air quality applications. In the three studies presented in Chapters 2-4, I integrate observations and modeled data to isolate smoke-driven changes at multiple spatial and temporal scales, including a novel examination of the impact of transported wildfire smoke on baseline solar resources. My research is rooted in observations from ground, aircraft, and satellite-based instruments that characterize atmospheric radiation, aerosol and chemical composition, and the location of smoke plumes. I leverage existing data from radiative transfer models to demonstrate smoke-driven changes in operational datasets and design custom model runs as a means of bridging observational gaps. My main objective is to quantify changes in key radiation metrics (total PAR, PAR DF, DNI, GHI, and actinic flux) due to wildfire smoke as a foundation for further studies on smoke-driven changes in agriculture, energy, and air quality.

Chapter 2 is adapted from a manuscript published in the *Journal of Geophysical Research: Atmospheres* (Corwin et al., 2022b). In Chapter 2, I quantify smoke-driven changes in surface-level PAR at ten agriculturally important locations across CONUS. Chapter 2 asks (a) how wildfire smoke varies spatially and temporally during the growing season across the U.S. and (b) how total PAR and PAR DF at the surface vary with wildfire smoke. This work builds on previous wildfire smoke climatologies (Brey et al., 2018), model-based assessments of DF and plant productivity (e.g., Schiferl & Heald, 2018), and observed aerosol-radiation-productivity relationships across a range of ecosystems (e.g., McKendry et al., 2019). My findings demonstrate a trend of abundant and increasing smoke over agriculturally productive areas as well as smoke's potentially beneficial impacts on PAR DF in areas with few or no clouds.

Chapter 3 is adapted from a manuscript under review for publication in *Nature Communications*. In Chapter 3, I examine how baseline solar resources fluctuated across historical smoke conditions based on output from a commonly used operational solar radiation model. I compare these variations to observed smoke locations and aerosol properties and contrast smoke- and cloud-driven changes. My primary aim in this study is to quantify the impact of daily smoke-driven irradiance changes on monthly mean (i.e., baseline) DNI and GHI for both local plumes of fresh, near-surface, dense smoke and transported plumes of dilute, lofted, aged smoke. My inclusion of areas primarily affected by transported smoke over multiple years represents a unique contribution to the existing literature on smoke and solar energy. Through daily, monthly, and multi-year analyses at state and national scales, I find that resources for CSP production are more vulnerable to local and transported smoke whereas PV production–the dominant source of U.S. solar energy–remains relatively stable under transported smoke plumes.

Chapter 4 is adapted from a manuscript in preparation for publication in the *Journal of Geophysical Research: Atmospheres*. In Chapter 3, I estimate smoke-driven changes in downwelling actinic flux at altitudes throughout the boundary layer and at the surface using field measurements and a radiative transfer model. My goal is to answer two questions: 1) to what extent does wildfire smoke change downwelling actinic flux at the peak wavelength for NO_2 photolysis (380 nm), and 2) how well does TUV characterize changes in downwelling actinic flux under smoke-impacted conditions given the limited nature of field observations? My findings indicate that smoke can drive substantial reductions in actinic flux at the surface and that reductions decrease rapidly with altitude. Additionally, modeled results may require bias corrections to align with measurements but, ultimately, show promise for expanding these assessments beyond locations with direct measurements. Characterizing surface-level changes in actinic flux is an important step toward better constraining the photolysis rates used by chemical transport models to predict pollutant (e.g., ozone) evolution in a smoke-filled boundary layer.

Chapter 5 summarizes my findings from the previous chapters as well as high-level takeaways. I also outline potential future research stemming from the studies conducted for this dissertation.

CHAPTER 2

SMOKE-DRIVEN CHANGES IN PHOTOSYNTHETICALLY ACTIVE RADIATION DURING THE U.S. AGRICULTURAL GROWING SEASON[2]

2.1 INTRODUCTION

As noted in the introduction, increasing wildfire activity is leading to greater wildfire smoke emissions with important implications for aerosol-radiation interactions over CONUS. By changing surface shortwave radiation levels, aerosols, including those from wildfires, can influence Earth systems that rely on radiation to function, such as plant productivity. Plants specifically rely on PAR, which are wavelengths of light extending from 400 to 700 nm.

The direct component of PAR benefits sunlit leaves, whereas diffuse radiation is able to reach shaded leaves and boost overall canopy light use efficiency and productivity, particularly when sunlit leaves reach saturation (Kanniah et al., 2012; Knohl & Baldocchi, 2008; Roderick et al., 2001; Sinclair et al., 1992). Reducing total PAR via aerosol absorption can negatively impact plant productivity, but increasing the DF via aerosol scattering can result in more efficient use of available light, a phenomenon known as the diffuse radiation fertilization effect (DRFE) (Greenwald et al., 2006; Kanniah et al., 2012; Knohl & Baldocchi, 2008; Schiferl & Heald, 2018). The degree to which the DRFE benefits productivity depends on the tradeoff between decreasing total PAR and increasing PAR DF as well as on plant traits such as canopy structure, leaf area index, and photosynthetic pathway (e.g., C3 or C4), which determine the extent of shaded leaves and light saturation (Kanniah et al., 2012). Few studies examine wildfire smoke's impact on the DRFE, but the existing literature indicates that understanding how smoke affects

[2] Adapted from Corwin, K. A., Corr, C. A., Burkhardt, J., & Fischer, E. V. (2022). Smoke-Driven Changes in Photosynthetically Active Radiation During the U.S. Agricultural Growing Season. *Journal of Geophysical Research, D: Atmospheres*, *127*(23). https://doi.org/10.1029/2022JD037446

surface radiation may be important for productivity (Hemes et al., 2020; Lee et al., 2022; McKendry et al., 2019). Therefore, large-scale longitudinal studies of smoke-radiation interactions that are based on observational data are needed to better understand smoke's impact on ecosystems and, given the prevalence of smoke over agricultural land, on food systems (Brey et al., 2018).

We present an analysis of smoke trends and associated changes to surface-level shortwave radiation at 10 sites across the contiguous U.S. from 2006 to 2020. We leverage observational data from ground-based radiation measurements and satellite observations of wildfire smoke, clouds, and AOD to examine (a) how wildfire smoke varies spatially and temporally during the growing season across the U.S. and (b) how total PAR and PAR DF at the surface vary with wildfire smoke. We focus our analysis on the main agricultural growing season (April–September) in the U.S. and over agriculturally important regions.

2.2 METHODS

This analysis leverages radiation, smoke plume, cloud, and aerosol data sets from ground and satellite observations. Detailed descriptions of each data set are presented in the following sections. Data processing and analysis are summarized in Figure 2.1.

2.2.1 UVMRP Shortwave Radiation Data

The United States Department of Agriculture's (USDA) UV-B Monitoring and Research Program (UVMRP) (Bigelow et al., 1998; USDA n.d.); https://uvb.nrel.colostate.edu/UVB) observes surface-level solar radiation using a network of 38 active sites across the U.S., Canada, South Korea, and New Zealand. Most monitoring sites (34) are distributed across the continental U.S. in agriculturally important regions as the program's primary goal is to develop a UV-B

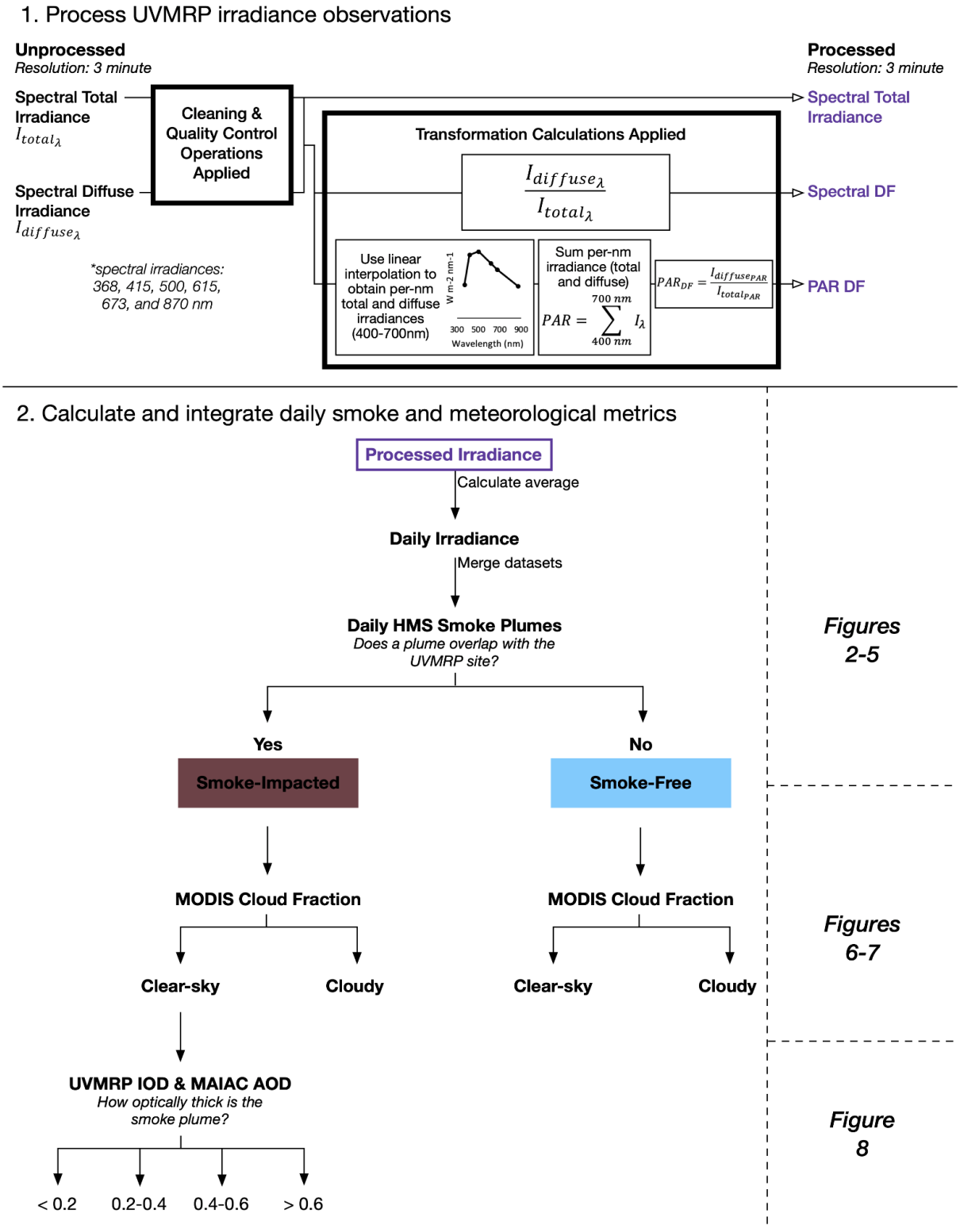

Figure 2.1: Diagram summarizing data processing and integration for the irradiance (UVMRP), smoke plume (HMS), cloud (MODIS), and optical depth (UVMRP & MAIAC) data sets used for this analysis.

climatology to better understand how UV-B radiation impacts agricultural crop and animal production (Bigelow et al., 1998). We focus on data from 10 UVMRP sites (Table 2.1) distributed across eight U.S. regions (map in Figure 2.5) that are largely similar to the EPA regions and were analyzed in the Brey et al. (2018) smoke climatology. These sites were selected in consultation with UVMRP staff and provide broad spatial coverage of the predominant smoke trajectories in the contiguous U.S. The Davis, CA and Pullman, WA sites are located near large western wildfires and primarily experience optically thick and fresh smoke conditions. These two sites are also located in the Southwest and Northwest, respectively, which are the regions experiencing some of the largest increases in wildfire activity (Westerling, 2016). The northern sites in Poplar, MT, Fargo, ND, and Grand Rapids, MN are impacted by large, aged, laterally extensive, and persistent smoke plumes transported from fires in the western U.S. and Canada (Brey et al., 2018). The north-south distribution of sites captures a range of plume conditions as the northern sites are located below the core of these aged plumes and the southern sites are closer to the edges. The Geneva, NY site is included because smoke-impacted days are infrequent and the smoke reaching NY is generally much older and optically thinner. Finally, the

Table 2.1: Description of UVMRP Site Locations and Data Availability

Site	Location	Region[a]	Smoke indicator[b]	Irradiance (total and DF)[c]	IOD[c]	AOD[d]	CF[e]	Complete records[f]	Smoke-free days	Smoke-impacted days
Davis, California	38.53°N, 121.78°W	Southwest (SW)	99%	97%	99%	89%	100%	85%	1,952	383
Pullman, Washington	46.76°N, 117.19°W	Northwest (NW)	99%	94%	78%	70%	100%	52%	1,038	392
Poplar, Montana	48.31°N, 105.10°W	Rocky Mountain (RM)	99%	91%	98%	66%	100%	60%	1,112	526
Pawnee, Colorado	40.81°N, 104.76°W	Rocky Mountain (RM)	99%	77%	75%	70%	100%	51%	1,161	228
Fargo, North Dakota	46.90°N, 96.81°W	Great Plains (GP)	99%	91%	92%	59%	100%	50%	827	556
Billings, Oklahoma	36.60°N, 97.49°W	Southern Plains (SP)	99%	87%	82%	67%	100%	52%	1,083	350
Grand Rapids, Minnesota	47.18°N, 93.53°W	Midwest (MW)	99%	93%	97%	51%	100%	47%	806	491
Bondville, Illinois	40.05°N, 88.37°W	Midwest (MW)	99%	81%	84%	53%	100%	42%	825	329
Starkville, Mississippi	33.47°N, 88.78°W	Southeast (SE)	99%	79%	79%	61%	100%	42%	1,023	125
Geneva, New York	42.88°N, 77.03°W	Northeast (NE)	99%	90%	97%	53%	100%	48%	1,107	201

Note. Analyses that contain a subset of the data products listed used the maximum number of data points available. At each site, 100% coverage of 15 growing seasons equals 2,745 days.

[a]Regions from Brey et al. (2018). [b]HMS smoke product. [c]UVMRP irradiance and instantaneous cloud-aerosol optical depth product. [d]MAIAC aerosol optical depth product. [e]MODIS cloud fraction product. [f]The percentage of records (days) at each site that have a smoke indicator and irradiance, IOD, AOD, and CF data. The number of smoke-impacted and smoke-free days with complete records is indicated in the last two columns.

Starkville, MS site introduces an analysis of smoke in the Southeast, which has a distinctly different source (i.e., local agricultural fires) and different optical properties (Bian et al., 2020; Brey et al., 2018). These sites are also located close to agricultural areas and, except for the CA site, distant from major metropolitan areas that contribute to aerosol loading. We refer to these sites by their geographical region code listed in Table 2.1.

Each UVMRP station is equipped with two multifilter rotating shadow-band radiometers (MFRSR) that measure total horizontal and diffuse-horizontal solar irradiance at seven wavelength passbands with a three-minute temporal resolution. The ultraviolet instrument (UV-MFRSR) measures irradiance at 300, 305, 311, 317, 325, 332, and 368 nm with a full-width at half maximum (FWHM) of 2 nm. The visible instrument (VIS-MFRSR) measures irradiance at 415, 500, 615, 673, 870, and 940 nm with an FWHM of 10 nm. The simultaneous collection of total and diffuse irradiance by the same MFRSR instrument allows for the real-time calculation of spectrally resolved direct normal irradiance which supports continued calibration via Langley analysis (Harrison et al., 1994) and the determination of total optical depth and instantaneous cloud-aerosol combined optical depth at the same temporal resolution. Langley calibration eliminates concerns that independent sensor drift could bias DF calculations. Drift may impact total PAR calculations, but all UVMRP sites maintain broadband PAR pyranometers for independent validation of total PAR. Calibration and validation details are available in Bigelow et al. (1998). As an operational program, the UVMRP provides routine maintenance and calibration of sensors to ensure reliable and relatively consistent data products for public use; however, the instrument fleet is aging as coverage spans nearly three decades at some sites.

We examined 15 years (2006–2020) of irradiance records for the 10 sites in Table 2.1. We limited our study to the six UV- and VIS-MFRSR bands that provide full coverage of the

PAR wavelength range: 368, 415, 500, 615, 673, and 870 nm. We performed extensive data cleaning and quality control operations that are described in detail below. The time-intensive and site-specific nature of the data cleaning processes necessitated restricting the analysis to the 10 sites selected. From the remaining three-minute UVMPR records, we calculated daily average values for the following variables: total spectral irradiance, spectral DF, total PAR irradiance, PAR DF, and instantaneous cloud-aerosol combined optical depth (IOD). All analyses were performed using daily average values for integration with satellite smoke, aerosol, and cloud products. An outline of the data processing and integration steps with associated figures is provided in Figure 2.1.

For data cleaning and quality control, we removed missing data and records with quality control flags that indicated whole instrument or individual channel damage or degradation. We only considered records for which irradiance data were available across all six wavelengths of interest. Occasional gaps exist due to instrument damage or maintenance. After implementing quality controls, we removed any records where the solar zenith angle was greater than 75° to reduce noise at times near sunrise and sunset. We removed all records containing negative irradiance values in the total, direct, and diffuse component and any time periods when all spectrally resolved total irradiance values equal zero.

Data anomalies were present across multiple sites and years, characterized by irradiance values that far exceeded the peak solar irradiance at the measured wavelengths. These anomalies impacted all bands on either the UV- or VIS-MFRSR but occurred infrequently, affecting only 0.09% of the nearly 8.29 million three-minute cleaned records across all 10 sites. To ensure that only physically reasonable values were included in the analysis, we removed records with total irradiances in excess of threshold values. Since the UVMRP site in New Mexico observes some

of the highest irradiance values and lowest cloud interference in the network, we used data from the New Mexico UVMRP site to approximate the maximum spectral irradiance possible for use as a network threshold. We removed all records with an irradiance greater than 110% of the maximum spectrally resolved irradiance recorded in New Mexico from 2006 to 2020. As such, we remove records that exceed the following thresholds: 1.26 W/m2 for 368 nm, 2.42 W/m2 for 415 nm, 2.53 W/m2 for 500 nm, 2.42 W/m2 for 615 nm, 2.27 W/m2 for 673 nm, and 1.37 W/m2 for 870 nm. Overall, the volume of data available helps reduce the impact of anomalies removed during the data cleaning process.

Ultimately, we are interested in understanding how the overall DF of PAR varies, which requires estimating the total and diffuse irradiance over the entire 400–700 nm range. We performed a linear interpolation between six adjacent wavelength bands spanning 368–870 nm to estimate the per-nanometer irradiance from 400 to 700 nm for both total and diffuse irradiance (Figure 2.1). While the solar spectrum is not linear, we can approximate the overall shape of the spectral curve using these six closely spaced MFRSR bands, especially since the 500 nm channel nearly captures the peak wavelength of solar irradiance. We summed the interpolated values to obtain total and diffuse PAR. A comparison of the interpolated total PAR values to total PAR measured by a collocated broadband PAR LI-190SA Quantum Sensor from LI-COR for a subset of years (2015–2019) at the Pawnee, CO site is included in the Appendix A1 (Figure A1.1). Finally, we identified and removed a small subset of days with fewer than 170 three-minute observations (i.e., fewer than 8.5 hr of data; Figure A1.2) and averaged all calculated PAR and retrieved spectral values to the daily level. The resulting site-specific data availability ranged from 77% to 97% (Table 2.1).

2.2.2 Hazard Mapping System (HMS) Smoke Plume Data

The HMS (https://www.ospo.noaa.gov/Products/land/hms.html) operated by the National Oceanic and Atmospheric Administration's (NOAA) National Environmental Satellite, Data, and Information Service (NESDIS) uses data from polar orbiting and geostationary satellites to provide daily operational smoke plume extents across North America in near real-time. The HMS became operational in 2003 for the U.S. and Canada, expanding to full North American coverage with the incorporation of Mexico and Central America in 2006 (Ruminski et al., 2006). Spatial coverage of the HMS spans from 14.6°N to 72°N and 50°W to 170°W and captures each region's primary biomass burning season. Smoke plumes are identified and outlined manually by analysts using 2 km or finer resolution visual-band imagery from the GOES satellites. Analysts rely on a series of images taken throughout the day, but primarily those near sunset and sunrise when smoke plumes are most visible. Occasionally, analysts reference observations from polar-orbiting satellites to identify smoke as well as use infrared bands to distinguish between clouds and smoke (Rolph et al., 2009).

Multiple limitations characterize the HMS smoke plume data and impact potential uses of the data. Because the smoke product relies on visible imagery, no information about smoke plume location or extent is available at night. Analysts make no attempt to identify the smoke's source. As such, smoke plumes may originate from wildfires, agricultural burning, or prescribed burning. Areas with high albedos, such as snow, pose a challenge for identifying smoke particles. The HMS also struggles to distinguish between clouds and smoke due to the reliance on visual imagery, and although infrared channels can help, untangling when clouds obscure smoke is a challenge. Similarly, smoke can be difficult to discern from anthropogenic haze, particularly when smoke becomes lofted, travels far from its source, and mixes with pollutants. Overall, the

greatest uncertainties are in determining the location of the edge of the plume, where smoke may be optically thinner or mixed with haze. Edge detection issues due to smoke-haze mixing are most likely to occur at the SE site, but the shifts in PAR DF presented here show little sensitivity to the number of smoke-impacted days at the SE site (Text A1.1). Ultimately, these limitations make the HMS smoke product a conservative estimate of smoke plume number and extent (Brey et al., 2018).

We use the HMS smoke product to distinguish between smoke-free and smoke-impacted days at each UVMRP station. We use the HMS shapefiles, extract the smoke plume polygons, and determine if a polygon overlaps with a UVMRP station. Site-specific results for growing season days are merged with the associated daily average radiation metrics for analysis (Figure 2.1). HMS data coverage is 99% at all UVMRP sites as missing data between 1 April and 30 September for 2006–2020 impact all sites equally.

2.2.3 MODIS Cloud Fraction Data

The Moderate Resolution Imaging Spectroradiometer (MODIS) instrument provides daily satellite imagery from the National Aeronautics and Space Administration Earth Observing System's Terra and Aqua satellites. The MODIS level-3 gridded atmosphere daily global joint product (MOD08_D3, MYD08_D3) (Platnick et al., 2015) provides average CF at a spatial resolution of 1 × 1°. Terra and Aqua overpasses capture morning (~10:30 a.m. local time) and afternoon (~1:30 p.m. local time) conditions, respectively. We calculate a daytime CF by averaging the CF values from the morning and afternoon retrievals for each day at each site. The absence of observations in the early morning and late afternoon when the solar zenith angle is large is expected to be less important for applications of the current work (e.g., crop growth). Additionally, the resolution of MODIS products captures the region surrounding UVMRP sites

but may not represent the exact conditions observed by the MFRSR. For example, irradiance and optical depth measurements can be heavily influenced by an optically thick but isolated cloud over the site while the satellite-observed CF will remain low. The temporal resolution helps mitigate the impact of rapidly changing cloud cover on daily average irradiance and optical depth measurements. Finally, using MODIS to determine cloud cover under smoke-impacted conditions poses a challenge because MODIS algorithms struggle to distinguish clouds from smoke, leading to the misclassification of optically thick smoke as cloud cover. However, smoke-impacted days with high CFs (>0.8) make up only 3.4% of all days across the 10 UVMRP sites selected and 1.1% of days that also have UVMRP radiation data available. As such, we expect that cloud-smoke confusion is a minor issue at most sites we examine. We note where cloud-smoke misclassification may impact our analyses in Sections 9 and 10.

2.2.4 Multi-Angle Implementation of Atmospheric Correction (MAIAC) AOD Data

The MAIAC (Lyapustin & Wang, 2018a) algorithm determines AOD using MODIS data from both the Terra and Aqua satellites. Described in detail by Lyapustin and Wang (2018b) and Lyapustin et al. (2018), MAIAC leverages the different spatial and temporal variability of land surfaces and aerosols to improve cloud masking capabilities and retrieve high resolution (1 km) AOD. Land cover can change quickly over short distances but remains relatively stable over short periods of time. In contrast, aerosols are relatively uniformly distributed spatially (i.e., in 1 × 1 km grids) but can change rapidly over a short period of time. MAIAC uses time series analysis of the land surface reflectance to identify recent clear-sky land cover conditions and detect changes due to clouds or aerosols.

More precisely, MAIAC transforms the 1 km gridded L1B MODIS data into 1,200 km2 tiles corresponding to the MODIS sinusoidal grid. Terra and Aqua overpasses are combined, and

the number of orbits recorded for each tile ranges from 1 to 2 at the equator to up to 16 at higher latitudes. MAIAC uses a sliding window technique to store MODIS imagery from previous days and identify a recent clear-sky reference image for each 1 km grid cell. MAIAC compares the most recent image to the clear-sky reference to construct a cloud mask and then performs a smoke test to reduce the misclassification of optically thick plumes as clouds and ensure an AOD retrieval. The smoke test compares changes in the deep blue (0.412 μm) shortwave band to reflectance at longer red (0.646 μm) and blue (0.466 μm) wavelengths. Smoke increases attenuation in the 0.412 μm band because of greater multiple scattering by aerosols and stronger shortwave absorption by organic carbon. If smoke is detected, MAIAC retrieves an AOD even if the cloud mask indicates a possibly cloudy pixel. Otherwise, MAIAC AOD is only retrieved for clear-sky conditions. The improved cloud detection and screening with MAIAC allows for more accurate AOD computations. MAIAC has been shown to correspond well with AERONET measurements (Lyapustin et al., 2018) and outperform the Dark Target and Deep Blue AOD retrieval algorithms on multiple metrics (Jethva et al., 2019). Although MAIAC provides an improved cloud mask, CF values are not included in the product. As such, we rely on the MODIS level 3 CF data as described in Section 4.

We use the 550 nm AOD retrievals available in the daily atmosphere MAIAC product (MCD19A2) to calculate an average daily AOD for all growing season days from 2006 to 2020. We include data from both the morning (Terra) and afternoon (Aqua) orbits in our calculations to better characterize the overall daytime average AOD. After identifying which MODIS tile contains each of the 10 UVMRP sites in Table 2.1, we identify the 1 km grid cell (pixel) containing the site location. We extract the overlapping pixel and the 16 nearest neighbors to create a 5 × 5 km box around each site. Given our focus on smoke plumes, which often exhibit

high spatial variability, we include possibly cloudy skies in our analysis in addition to the clear-sky best quality AOD values.

2.3 Results and Discussion

2.3.1 Monthly Average Smoke Frequency During the Growing Season

Smoke frequency and timing varies regionally across the continental U.S. between April and September, the primary agricultural growing season (Figure 2.2). At the start of the growing season, smoke-impacted days are infrequent but most common in the SP, GP, and western MW (see Table 2.1 or Figure 2.5 for regional codes). The particularly high frequency of smoke over eastern Kansas in April (~25% of days) coincides with the Flint Hills region. Prescribed fires are used to preserve Flint Hills grasslands in the spring with the bulk of the burning occurring in April (Baker et al., 2019; Möhler & Goodin, 2012). In May, smoke-impacted days remain infrequent and still mainly occur in the SP, GP, and MW. The higher frequency of smoke-impacted days in the SP and GP in the early growing season may result from smoke transported from southern Mexico and Central America where fire starts are common in April and May (Peppler et al., 2000; Rogers & Bowman, 2001; J. Wang et al., 2009; S. C. Wang et al., 2018). In June, an increase in smoke-impacted days is evident over Arizona and New Mexico, which is consistent with earlier fire start times (Westerling et al., 2003) and the predominance of local smoke (Brey et al., 2018) in this region. Fire starts shift north and northwest as the season progresses (Westerling et al., 2003), which results in increasingly frequent locally sourced smoke over California and the NW and RM regions in July and August. At the same time, almost all areas of the GP and MW, which are major agricultural regions, experience smoke overhead for at least 30% of August days, which is consistent with findings in Brey et al. (2018) that smoke is transported into these regions from the SW, NW, RM, and Canada. Locations in the northern

RM and GP regions, including western Montana and North Dakota, experience smoke on nearly 60% of all August days on average. Ultimately, smoke frequency peaks during the mid to late growing season across most of the U.S. due to large western wildfires. Smoke-impacted days decline in September, persisting mostly over California and the NW where local fires continue to produce smoke (Westerling et al., 2003).

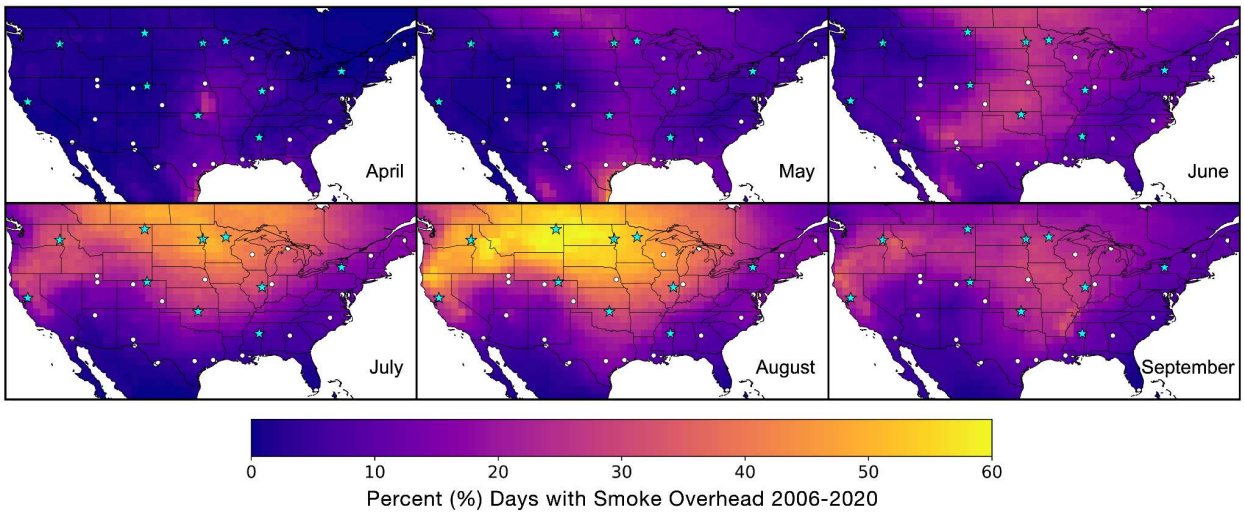

Figure 2.2: Average percentage of smoke-impacted days per growing season month (April–September) from 2006 to 2020 based on the overlap of the HMS Smoke Product plume polygons with the centroid of a 1° grid. Blue stars indicate the 10 sites analyzed here and the white circles show the remaining UVMRP network sites in the contiguous U.S. A map showing the regional divisions and codes is provided in Figure 2.5 for reference, and the regional code associated with each of the 10 sites analyzed (blue stars) is provided in Table 2.1.

Similar to the HMS trends shown in Figure 2.2, the 10 UVMRP sites demonstrate distinct differences in monthly smoke frequency across the 15 years of growing seasons analyzed (Figure 2.3). At all sites, smoke impacts an average of 20% of all growing season days, ranging from 4% in April to 38% in August (Figure A1.3). Smoke-impacted days are most common in the mid to late growing season across sites in all regions except the SE. Smoke becomes increasingly more frequent as the growing season progresses with a peak in August at all sites where the smoke primarily stems from wildfires in the western U.S. (i.e., SW, NW, and RM; Brey et al., 2018) and Canada. Northern sites in the RM, GP, and MW regions experience the most smoke-

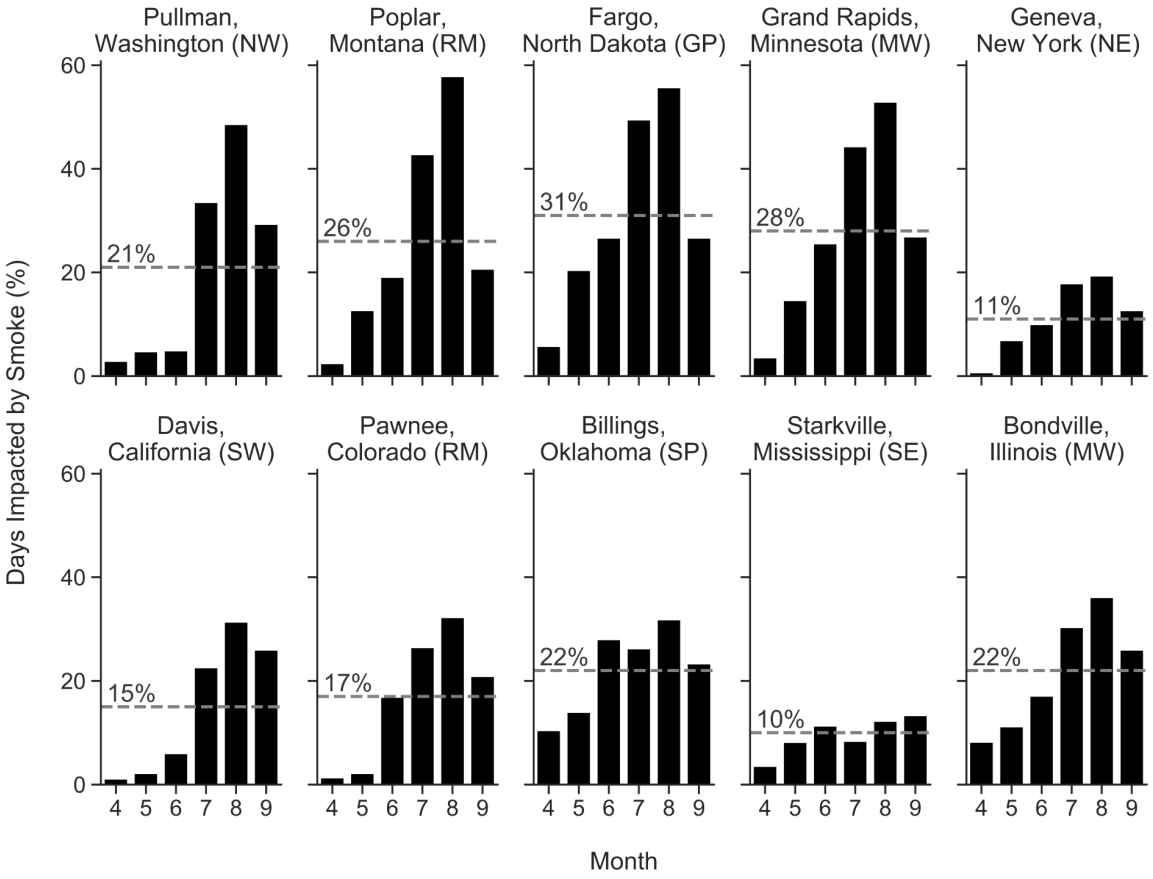

Figure 2.3: Overall (dashed line) and monthly (black bars) percentage of growing season (April–September) days impacted by smoke at each UVMRP site from 2006 to 2020. The top row corresponds to more northern sites and the bottom to more southern sites with western sites on the left and eastern sites on the right. Each site's region is indicated in parentheses.

impacted days during the growing season with over a quarter (26%–31%) of all days, and over half (53%–58%) of all August days, characterized by smoke overhead. Sites in the SW, NW, and southern RM regions experience similar monthly smoke patterns, but the magnitude of smoke frequencies is lower (average: 15%–21%). The SW and NW sites tend to experience smoke from local sources compared to the northern RM, GP, and MW regions where smoke from multiple regions is transported overhead, leading to more smoke-impacted days (Brey et al., 2018).

The NE and SE sites experience the least number of smoke-impacted days across the 10 UVMRP locations (Figure 2.3). The NE site is characterized by temporal smoke patterns similar

to those found at other sites, which is consistent with the similar smoke origins documented by Brey et al. (2018). The SE site, however, shows minimal variability in smoke frequency between May and September, a distinctly different smoke pattern consistent with a change in smoke origin. In the SE, smoke is primarily sourced from local agricultural fires as opposed to fires in the SW, NW, RM, or Canada, which are the dominant source of smoke for other regions (Brey et al., 2018).

2.3.2 Interannual Variability of Smoke Overhead During the Growing Season Between 2006 and 2020

Between 2006 and 2020, the 10 UVMRP sites experienced smoke overhead on 20% of growing season days on average (Figure 2.4). However, sizable interannual variability in smoke exposure is evident in Figure 2.4; annual smoke frequencies at the 10 stations range from 12% to 31% of growing season days. Multiple heavy smoke years are included in the record, including 2012 and 2018, which result in 31% and 30% smoke-impacted days, respectively. The percentage of growing season days impacted by smoke increases over time with a positive Pearson's correlation coefficient of 0.60 (p-value <0.05). Such an increase in smoke frequency is consistent with increasing wildfire frequency, burn area, and season length (Abatzoglou & Williams, 2016; Westerling, 2016; Westerling et al., 2006).

Figure 2.5 shows that smoke affects all sites during the growing season across all years from 2006 to 2020. The northern RM, GP, and MW sites are located far downwind of western wildfires but generally experience higher percentages of smoke-impacted days (26%–31%) during the growing season than do sites in the SW, NW, and southern RM (15%–21%) that are closer to fires. Northern and Midwestern sites face smoke from multiple western U.S. regions

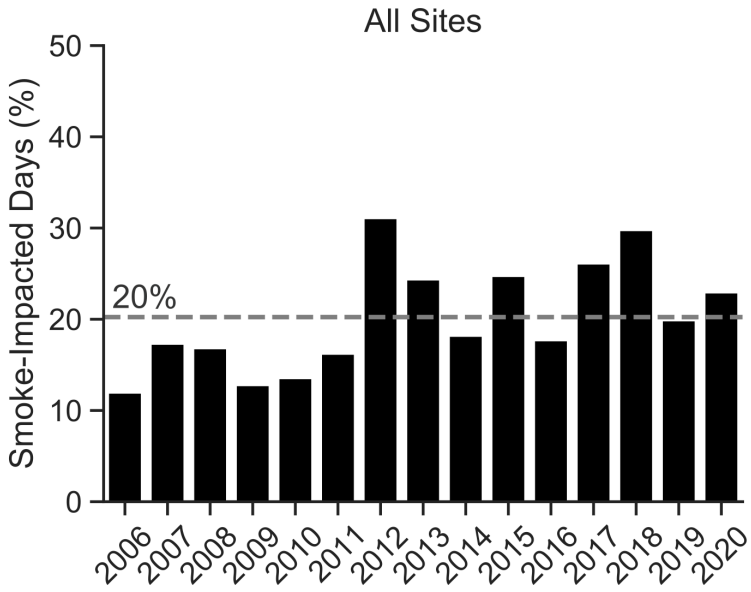

Figure 2.4: Overall (dashed line) and yearly (black bars) percentage of days during the growing season (April–September) from 2006 to 2020 with smoke present in the atmospheric column above the 10 UVMRP sites analyzed.

and Canada. Smoke frequency peaks at the SW and southern RM sites during locally severe wildfire seasons. The 2008, 2018, and 2020 wildfire seasons were some of the worst in California state history, and the percentage of smoke-impacted days is 18% points higher in these high smoke years (30%) than the average across all other years (11%). Similarly, Colorado's severe wildfire seasons in 2012, 2018, and 2020 increased smoke-impacted days by 24% points on average (high smoke average: 36%; low smoke average: 12%). Even within different regions, smoke frequency varies substantially with latitude. In the RM region, the interannual trends differ between the Montana and Colorado sites. The former is more consistently impacted during the growing season while the latter shows distinct peaks in exposure amid overall fewer smoke days. In the MW, the Minnesota site in the north also generally experiences more smoke-impacted days than the Illinois site further south. These northern sites are located within the predominant transport path for smoke from the SW, NW, and western Canada. The Colorado site is along the southern edge and the Illinois site is along

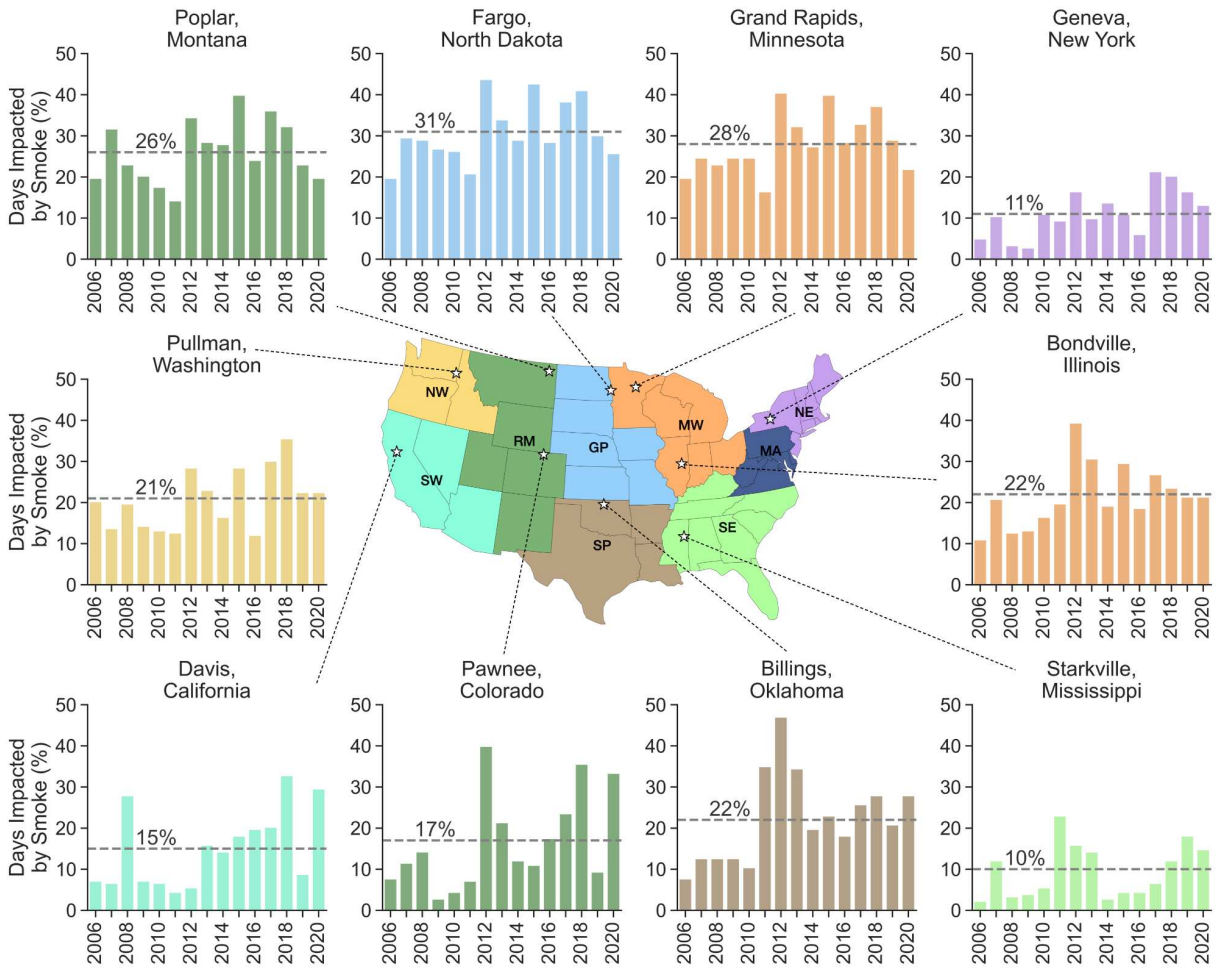

Figure 2.5: Overall (dashed line) and yearly (region-colored bars) percentage of smoke-impacted days during the growing season (April–September) at each UVMRP site analyzed showing the spatial and temporal variability of wildfire smoke across the U.S. from 2006 to 2020. The colored regions correspond to those used by Brey et al. (2018) and are largely similar to the U.S. EPA regions. Table 2.1 shows the regional assignments for each UVMRP site.

the southeastern edge of the primary smoke pathways from large western wildfires (Figure 2.2), resulting in lower smoke frequencies. However, the peaks in smoke frequency at the Colorado site highlight the importance of local wildfires in determining annual smoke exposure at this southern RM site.

2.3.3 Impact of Smoke on PAR DF Under Variable Cloud Conditions

Figure 2.6 compares PAR DF on all study days at all sites based on smoke and cloud conditions to approximate the relative importance of the smoke. Linear regression analyses

(Figure 2.6a) show that daily PAR DF increases with increasing CF for both smoke-impacted (DF = 0.50 CF + 0.31, $r = 0.78$, $p < 0.0001$) and smoke-free (DF = 0.64 CF + 0.20, $r = 0.89$, $p < 0.0001$) days. PAR DF on smoke-impacted days increases the most under clear-sky conditions (+0.10; Figure 2.6b). This 10-percentage point increase in clear-sky PAR DF results in a PAR DF equivalent to what is experienced on smoke-free days with a CF of 0.16. PAR DF reaches 0.5 at a CF of 0.39 on a smoke-impacted day as opposed to at a CF of 0.47 on a smoke-free day. As cloud cover increases, smoke's relative influence on scattering decreases, resulting in progressively smaller increases in PAR DF on smoke-impacted days. When daily CF reaches 0.74, PAR DF no longer increases with the addition of smoke (Figure 2.6b).

Similar trends are evident in an analysis of individual sites (Figure A1.4). Daily PAR DF at each site increases on smoke-impacted days, particularly those with minimal to no clouds. On clear-sky days, the site-specific increase in PAR DF (ΔPAR DFSmoke) with smoke ranges from 0.05 to 0.14. The greatest increase in clear-sky PAR DF occurs at sites in the NW (0.14) and SW (0.13), which are closer to large wildfire ignitions. Sites further east and south in the GP, SP, MW, and SE exhibit smaller increases in clear-sky PAR DF with smoke (0.05–0.09). Sites in the RM and NE experience increases in clear-sky PAR DF from 0.10 to 0.12. Smoke-impacted days correspond to an increase in PAR DF across all CFs at two sites: California and Colorado. At the other sites, PAR DF increases with smoke until high CF conditions are reached with this CF threshold ranging from 0.52 at the Illinois site to 1 at the Washington site. At all sites, the rate at which smoke increases PAR DF declines with increasing CF. Overall, smoke corresponds to higher PAR DF across more CF conditions at sites in the SW, NW, and RM regions, which are located closer to large western wildfires.

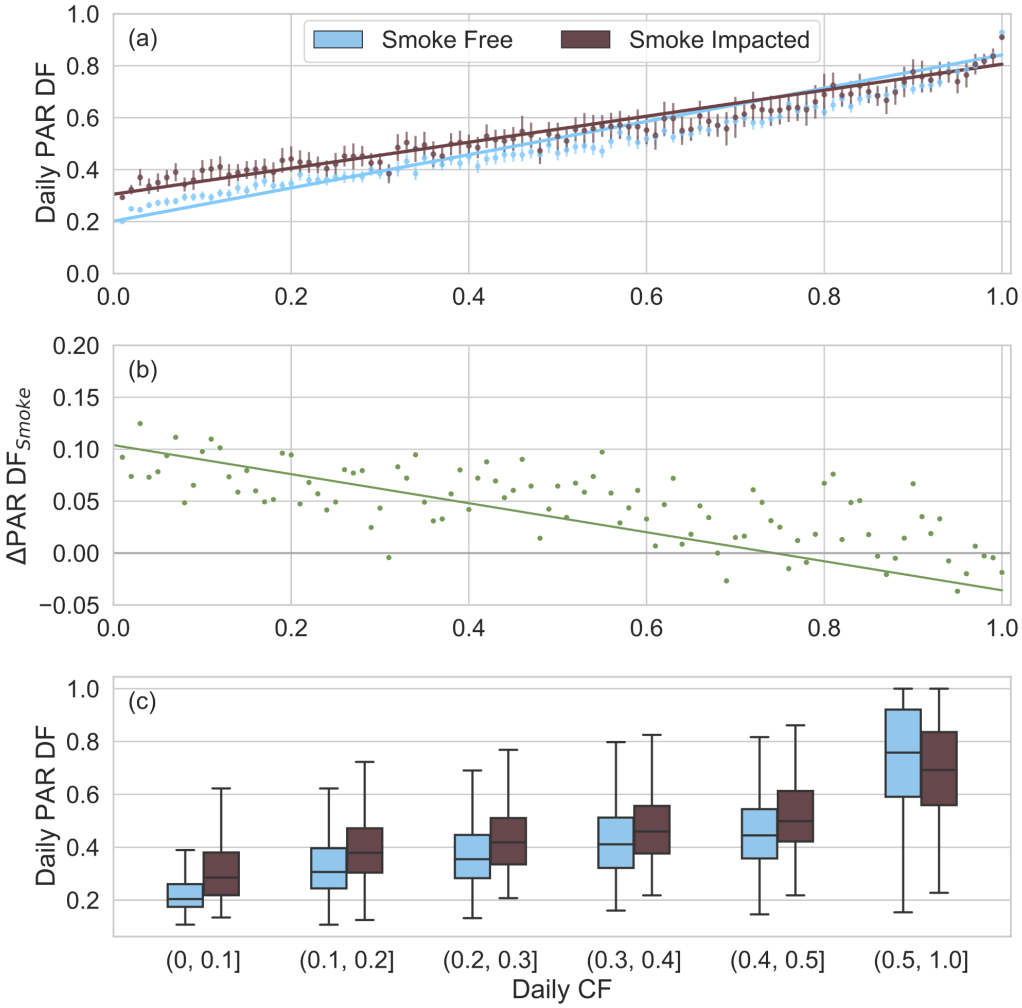

Figure 2.6: (a) Daily PAR DF based on daily cloud fraction (CF) on smoke-impacted (brown) and smoke-free (blue) days. Lines show the results of a linear regression analysis using data from all growing season days and all sites from 2006 to 2020 on smoke-impacted (PAR DF = 0.50CF + 0.31, $r = 0.78$, $p < 0.0001$, n = 4,868) and smoke-free (PAR DF = 0.64CF + 0.20, $r = 0.89$, $p < 0.0001$, n = 19,031) days. Data variability is visualized as points representing the average daily PAR DF in each CF bin (interval = 0.01) and vertical lines displaying the 95% confidence intervals for each point. (b) Change in daily PAR DF (ΔPAR DFSmoke) between smoke-impacted and smoke-free days across all CFs. The green line shows the difference between the two linear regression lines in panel a and the green points show the difference between the average daily PAR DF for each CF bin (interval = 0.01). (c) Distribution of daily PAR DF on smoke-impacted (brown) and smoke-free (blue) days grouped by daily CF at an interval of 0.1 up to a CF of 0.5. Days when CF exceeds 0.5 are combined given the reduced impact of smoke on DF at high CFs (panel b). This approach better highlights the shifts in DF at low CFs. The midline refers to the median, and the whiskers indicate the spread of all remaining data excluding outliers. Outliers are defined as PAR DF values falling outside 1.5 times the interquartile range. The bottom and top of the boxes represent the lower and upper quartile, respectively.

Figure 2.6c shows how the distribution of daily PAR DF varies by CF and focuses on days with minimal cloud cover (CF $\leq$ 0.5) since Figure 2.6b shows these days exhibit the largest increase in PAR DF. A clear upward shift in the PAR DF distribution occurs on smoke-impacted days with a CF at or below 0.5. Data from days with CF > 0.5 are grouped together and show that smoke fails to increase PAR DF at high CFs. Much of the interquartile range for smoke-impacted days overlaps with that for smoke-free days with the addition of smoke. We expect the impact of smoke on PAR DF to decline with increasing CF as scattering from clouds overwhelms the contribution of smoke scattering to PAR DF.

As noted in Section 2.2.3, the MODIS cloud detection algorithms have struggled historically to distinguish between optically thick smoke plumes and clouds. Although infrequent, smoke-cloud confusion can have important consequences for assessing the radiative effects of smoke as cloud optical depths can far exceed AODs. Days when MODIS misclassifies a smoke plume as a cloud are considered smoke-impacted in HMS but shifted to higher CF values in Figure 2.6. Artificially increasing CF on smoke-impacted days with high optical depths lowers the average optical depth for days with low CFs but has minimal impact on the optical depth of high CF days. Since optically thick smoke is expected to increase PAR DF more than optically thin smoke, decreasing the number of optically thick smoke-impacted days at low CFs may result in lower average PAR DF at low CFs. These effects would be particularly pronounced for clear-sky days with optically thick smoke. If these days with optically thick smoke were redistributed across lower CFs, we would expect to see a larger increase in PAR DF on smoke-impacted days than Figure 2.6 shows. As such, the results shown in Figure 2.6 represent a conservative estimate of smoke's radiative effects.

2.3.4 Impact of Smoke on Spectral DF and Total Spectral Irradiance Under Cloud Free Conditions

Given that smoke-driven increases in PAR DF are greatest under clear-sky conditions, we present a more detailed spectral analysis of DF and total irradiance on clear-sky days (CF < 0.01) in Figures 2.7 and 2.8. In total, 3,506 clear-sky records are available across all sites and years, and 28% of those records represent smoke-impacted days (Table A1.1). We expect the number of clear-sky days to be a conservative estimate due to the potential for smoke-cloud misclassification as discussed in Sections 2.2.3 and 2.3.3. A plurality (36%) of clear-sky records are from the Davis, CA site in the SW. To assess the sensitivity of the overall analysis to the CA site, we also examined how our results changed with the inclusion and exclusion of the CA site. Results of this analysis show the same directional trends as in Figure 2.7 with minimal changes in the magnitude of increase or decrease in spectral DF (+0.01) and total irradiance (−0.01 W/m2), respectively. Herein, we present results from the analysis across all sites.

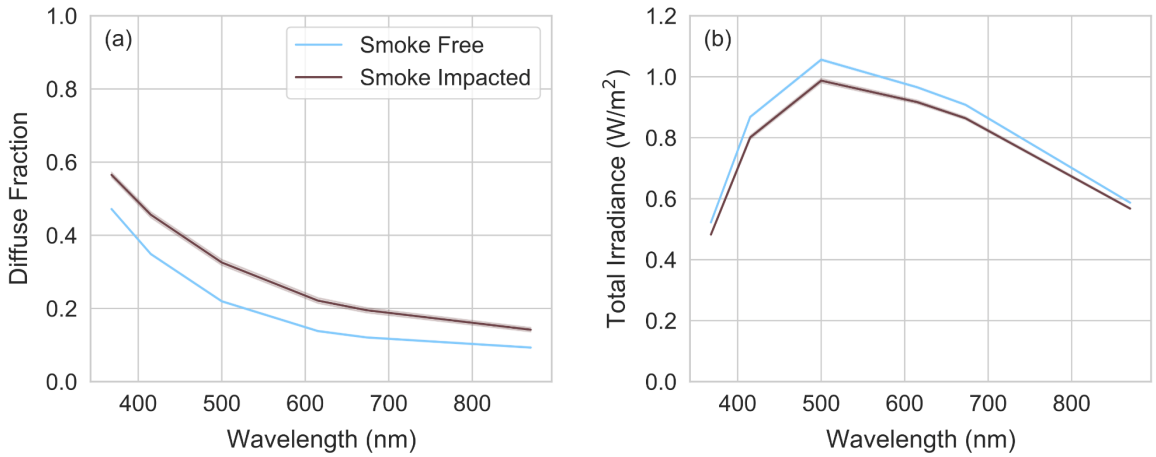

Figure 2.7: Variation in spectral diffuse fraction (a) and total spectral irradiance (b) at six multifilter rotating shadow-band radiometer (MFRSR) measured wavelengths on smoke-impacted (brown) and smoke-free (blue) clear-sky days during the growing season across all 10 sites ($n_{smoke\text{-}free}$ = 2,518; $n_{smoke\text{-}impacted}$ = 988). The solid lines indicate the average value. Shading shows the 95% confidence interval, but due to the large number of observations, the confidence intervals on both smoke-free and smoke-impacted days are relatively narrow and shading is barely visible.

Across the six MFRSR wavelengths measured between 368 and 870 nm, spectral DF is higher (Figure 2.7a) and total spectral irradiance is lower (Figure 2.7b) on smoke-impacted clear-sky days. The increase in spectral DF is greatest at 415 and 500 nm (+0.11) and least at 870 nm (+0.05). In the visible range, Mie scattering by smoke aerosols and absorption by brown carbon and NO_2 are more efficient at shorter wavelengths, preferentially increasing the diffuse component and decreasing total irradiance, respectively. As such, both processes work to increase DF at shorter wavelengths, which means that systems reliant on shorter wavelengths in the visible range will be more strongly impacted by smoke than those reliant on longer wavelengths. The reduction in total spectral irradiance is also greatest at 415 and 500 nm (−0.07 W/m^2) and least at the shortest (368 nm: −0.04 W/m^2) and longest wavelengths (870 nm: −0.02 W/m^2). Spectral DF increases on average by 45% (range: 20%–62%) and total spectral irradiance decreases on average by 6% (range: 3%–8%) with smoke at these 10 sites.

Isolating smoke-impacted clear-sky days, Figure 2.8 shows the impact of smoke plume optical thickness on DF and total irradiance at the spectral level. We use optical depth data derived from the site-specific ground-based MFRSR measurements (Figure 2.8a/b) and satellite retrievals (Figure 2.8c/d) to compare resulting trends based on observation platform. The former relies on optical depths calculated using Langley analysis and represents instantaneous cloud-aerosol optical depths (IOD). The latter are AOD computed using the MAIAC algorithm to minimize smoke-cloud confusion and ensure AOD retrieval on smoke-impacted days. However, limiting this analysis to clear-sky days as defined by the MODIS CF may result in the exclusion of a small number of clear-sky days with optically thick smoke, reducing the number of days in the high optical depth (>0.6) bin.

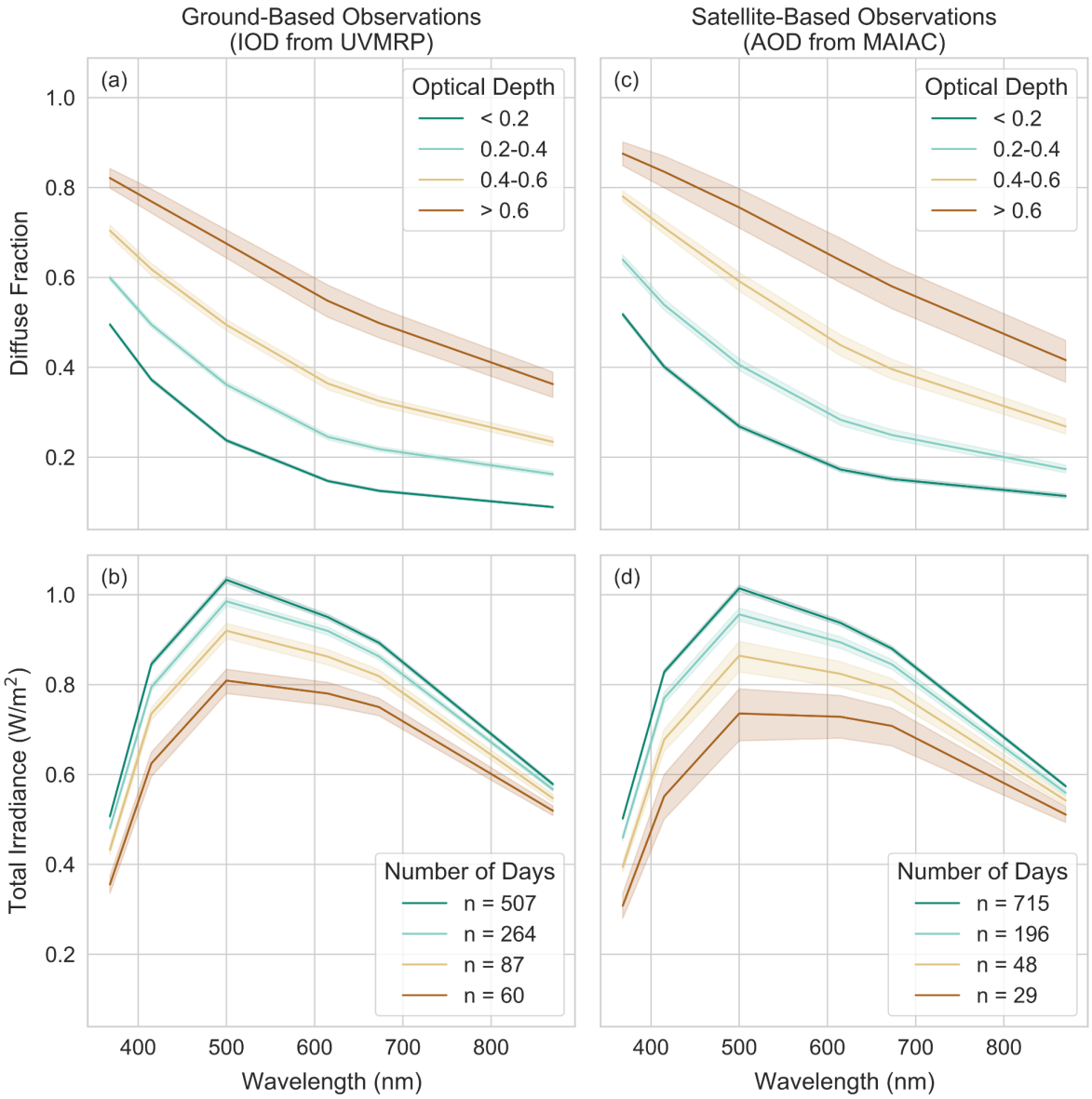

Figure 2.8: Variation in spectral diffuse fraction (a, c) and total spectral irradiance (b, d) across the six multifilter rotating shadow-band radiometer (MFRSR) wavelengths measured on smoke-impacted clear-sky days during the growing season. The impact of smoke plume optical thickness on irradiance measures is shown using different optical depths based on ground measurements of IOD from the UVMPR (a, b) and satellite retrievals of AOD by MAIAC (c, d). Solid lines indicate the average value and shading shows the 95% confidence interval (n_{uvmrp} = 918; n_{maiac} = 988).

The ground measurements show that DF (Figure 2.8a) becomes progressively larger as optical depth increases on smoke-impacted clear-sky days, which indicates a larger increase in DF under optically thick smoke plumes than under optically thin smoke plumes. Conversely,

total irradiance (Figure 2.8b) decreases with increasing plume optical depth. Changes to total irradiance based on optical depth are greatest at 500 nm, and least at 368 and 870 nm. Changes to DF, on the other hand, are relatively consistent across individual wavelengths. An optical depth increase from <0.2 to 0.2–0.4 results in an increase in DF between 0.07 and 0.12 (average: +0.10) depending on the wavelength. A similar magnitude increase occurs when the optical depth increases to 0.4–0.6 (range: +0.07–0.13; average: +0.11) and again to >0.6 (range: +0.12–0.18; average: +0.16). Days with optically thick smoke plumes (>0.6; n = 60) occur less frequently than days with optically thin smoke plumes (<0.2; n = 507), which results in wider 95% confidence intervals.

Ground-based sensors provide detailed information about radiation at specific sites; however, monitoring networks like the UVMRP are sparsely distributed. To expand beyond single sites and examine the impact of smoke on radiation at a national level requires satellite observations. Using the MAIAC AOD (Figure 2.8c/d) results in similar spectral DF and total spectral irradiance trends to those found using the MFRSR IOD observations (Figure 2.8a/b). DF becomes progressively larger as the optical depth increases on clear-sky days, indicating that optically thick smoke plumes increase DF more substantially than optically thin plumes.

However, DF values for each wavelength and optical depth bin are slightly higher (range: +0.01–0.10; average: +0.05) when plume optical depth is determined using MAIAC AOD rather than MFRSR IOD. The offset in DF values between the two methods is smaller when optical depths are lower. Across the six wavelengths assessed, the average offset between the two methods for the optical depth bins <0.2, 0.2–0.4, 0.4–0.6, and >0.6 are +0.03, +0.03, +0.08, and +0.07, respectively. Total irradiances decrease with increasing optical depth regardless of which optical depth measure is used, but most irradiances are slightly lower when using MAIAC AOD

bins. As with the DF comparison, the difference between the two methods is smaller when optical depths are lower. The average difference between the two methods for the optical depth bins <0.2, 0.2–0.4, 0.4–0.6 are −0.01, −0.02, −0.04, and −0.05, respectively. Overall, Figure 2.8 highlights the similarity between DF and total irradiance trends derived using the MFRSR and MODIS instrument data, which supports the use of MAIAC AOD to examine smoke-driven radiation changes at larger scales.

2.4 CONCLUSIONS

We combine ground and satellite observations to examine spatial and temporal trends in smoke presence across the U.S. during the growing season as well as smoke's impact on DF and total irradiance at the surface. The following conclusions stem from this analysis:

On average, smoke was present overhead on 20% of growing season days from 2006 to 2020 at the 10 UVMRP sites analyzed. Over that 15 year period, interannual trends show an increase in smoke frequency.

1. Annual site-specific smoke frequency varies with the prevalence of wildfires in smoke source regions, but northern sites in the RM, GP, and MW regions consistently experience smoke the most often.
2. Monthly trends show that smoke frequency increases as the growing season progresses and peaks in August at sites in all regions, except the SE where the smoke source is distinctly different. The high frequency of smoke over most of the U.S. in July and August aligns with the mid to late growing season.
3. Using the UVMRP data, we show elevated daily PAR DF values occur on smoke-impacted days across a wide range of cloud conditions. Average PAR DF increases most substantially on smoke-impacted days under cloud-free conditions (+0.10), but increases

in the median and interquartile range of PAR DF are evident at CFs below 0.5. On clear-sky days, the presence of smoke increases spectral DF and decreases total spectral irradiance at all six wavelengths measured by the MFRSR from 368 to 870 nm. These results indicate that on smoke-impacted days optimal PAR DF values for plant productivity are achievable at lower CFs than on smoke-free days.

4. When smoke is present, spectral DF increases and total spectral irradiance decreases with increasing smoke plume optical thickness. Optical depth observations from ground (UVMRP) and satellite (MODIS MAIAC) instruments produce similar trends for the impact of plume optical thickness on DF and total irradiance.

Our analysis provides a foundation for further research on the impact of smoke on PAR and the use of the UVMRP network data. The observed interannual and seasonal variability in smoke exposure captured by the UVMPR sites supports the use of the UVMRP network to characterize changes in PAR DF and total PAR associated with wildfire smoke and, in the future, to examine smoke-induced changes to agricultural crop yields within and across sites. Future work could focus on developing a model of PAR DF and total PAR on smoke-impacted days using data from all 34 UVMRP sites in the contiguous U.S. Expanding the number of stations included could introduce greater variability in smoke characteristics and irradiance within each region, which are not fully captured in the current study. With more sites, we can better characterize regional differences both in terms of average values and intraregional variance as not all sites in a region experience the same smoke conditions. Additionally, the inclusion of satellite AOD measurements supports scaling this analysis to the regional and national level and may allow for other atmospheric chemistry applications.

2.5 Data Availability Statement

The USDA's UVMRP data sets (USDA, n.d.) used in this analysis are described in Bigelow et al. (1998) and publicly available at https://uvb.nrel.colostate.edu/UVB. The HMS (NOAA NESDIS, n.d.), MODIS (Platnick et al., 2015), and MAIAC (Lyapustin & Wang, 2018a) data sets used in this analysis are also publicly available. The final cleaned and merged data set used to produce the results and visualizations presented here is available in a Dryad repository (Corwin et al., 2022a).

CHAPTER 3

SOLAR ENERGY RESOURCE AVAILABILITY UNDER EXTREME AND HISTORICAL WILDFIRE SMOKE CONDITIONS[3]

3.1 INTRODUCTION

Addressing climate change necessitates a rapid transition to renewable energy; one path to a sustainable future lies in solar energy production. Since 2010, advances in solar cell efficiency have decreased the cost of utility-scale photovoltaics (PV) by 82% (Feldman et al., 2020), increasing the feasibility of large-scale solar power. As of 2020, solar power constituted only 3% (80 GW) of U.S. energy production, but the U.S. aims to receive 45% of its energy from solar power by 2050 (Ardani et al., 2021). Meeting this target requires rapid widespread solar energy development, which means identifying locations with suitable solar resources given current and future climate, population, land use, and technological constraints.

Solar resources are assessed by the amount of shortwave direct normal (DNI) and global horizontal (GHI) irradiance a location receives. Concentrating solar-thermal power (CSP) relies on DNI while PV relies primarily on GHI (Lopes et al., 2018; Schroedter-Homscheidt et al., 2017). However, when considered simultaneously, GHI and DNI provide details on the amount of diffuse radiation, which affects PV panel technologies differently (Munshi et al., 2018). The most prominent commercially-employed panels are constructed from monocrystalline silicon (c-Si; ~95% of installations) and polycrystalline cadmium telluride (CdTe; most of the remaining 5% of installations) (Department of Energy, n.d.; Grand View Research, n.d.). CdTe and c-Si are direct and indirect bandgap materials, respectively, meaning that CdTe better absorbs solar

[3] Adapted from a manuscript under review: Corwin, K. A., Burkhardt, J., Corr, C. A., Stackhouse, P. Jr., Munshi, A. & Fischer, E. V. (under review). Solar energy resource availability under extreme and historical wildfire smoke conditions. *Nature Communications*. https://doi.org/10.21203/rs.3.rs-3979476/v1

radiation. About 1 μm of thin film CdTe absorbs nearly 99% of incident light (Rangel-Cárdenas & Sobral, 2017) by continuing to function under diffuse radiation. c-Si requires a thick wafer of over 100 μm and performance is reduced under diffuse radiation (Zengir et al., 2006). The tradeoff between direct and diffuse conditions–resulting from clouds and aerosols–carries important implications for solar energy production.

Anthropogenic pollution (Li et al., 2017, 2020) and dust (Sarver et al., 2013) reduce PV generation by decreasing solar radiation via atmospheric attenuation (absorption/scattering) and deposition on panels (soiling). In northern and eastern China, air pollution decreases annual average (peak) irradiance at PV arrays by 20-25% (34%) (Li et al., 2017). Globally, particulate matter (PM) reduces PV output by > 50% in polluted and desert regions, and soiling accounts for over two-thirds of energy lost (Li et al., 2020). In some regions, PM's impact on PV generation can rival that of clouds (Li et al., 2020). PM includes a wide range of aerosol types, including pollution, dust, and smoke, which interact with solar radiation differently based on their optical properties. As such, general examinations of PM's impact on solar energy may not fully capture the specific effects of increasingly abundant wildfire smoke.

As noted in Chapter 1, wildfire activity and smoke emissions are increasing at the same time that the U.S. is trying to increase solar energy generation. Most of the increase in wildfire activity has occurred in the Pacific Northwest and Southwest (Westerling, 2016), the latter having the highest U.S. solar resource potential. Recent case studies document sizable smoke-driven reductions in PV output during severe local wildfires over short time intervals and at specific locations and aerosol optical depths (AOD). Average PV output declined 34% over two days at a PV plant in Spain due to smoke (Gómez-Amo et al., 2019), 7% at a solar lab in Australia during a controlled burn when AOD reached 0.25 (-27% at peak) (Perry & Troccoli,

2015), and ~10-50% at southern California solar plants during the 2020 wildfire season when AOD ranged from 0.5 - 4.5 (Donaldson et al., 2021). Examinations of solar resource and forecast models demonstrate the need to include aerosol parameters that account for smoke. Solar forecasts improved nearly 50% when using aerosol inputs from a 3-hour reanalysis product rather than a monthly aerosol climatology (Juliano et al., 2022). Similarly, using a satellite-derived AOD product that better detects smoke's presence and spatial variability improved a solar resource model's accuracy compared to ground-based observations (Lin et al., 2023).

In this study, we assess wildfire smoke's impact on baseline solar resource availability across multiple temporal and spatial resolutions. We leverage daily case studies, monthly aggregations, and multi-year analyses to quantify smoke's impact on DNI and GHI at the state, regional, and national levels. At the finest scale, we examine daily localized impacts of smoke in California during the 2020 wildfire season under different aerosol and cloud conditions to demonstrate the range of smoke's influence on irradiance. We ask how smoke plume optical thickness affects the daily severity of smoke-driven irradiance changes and how cloud-driven irradiance changes compare. At larger temporal and spatial scales, we compare regional and national solar resources under high (2020) and low (2019) smoke conditions to bookend potential future and historical smoke impacts, respectively. We ask how much daily smoke-driven irradiance changes affect monthly mean DNI and GHI, how these impacts vary for local and transported smoke, and how these impacts relate to AOD. We use the resulting mean irradiances to model smoke's impact on PV output at 13 locations across CONUS for c-Si and CdTe panels. Finally, we expand our analysis to a 16-year period (2006-2021) to characterize longer-term, regional smoke-irradiance interactions even as impacts may increase into the future.

Overall, while we examine both DNI and GHI, our discussion focuses on GHI because stationary PV panels represent the bulk of U.S. solar installations.

We rely on modeled clear-sky and all-sky DNI and GHI from the National Renewable Energy Laboratory's National Solar Radiation Database (NSRDB) at 4-km spatial and 30-minute temporal resolution across CONUS. All-sky values include cloud and aerosol impacts; clear-sky values include aerosols but exclude clouds. We compute 1) daily means for each variable using times when the solar zenith angle is < 75°, 2) cloud-driven changes by subtracting the clear-sky (i.e., cloud-free) and all-sky values, and 3) smoke-driven changes by subtracting clear-sky values on smoke-impacted and reference smoke-free days. We pair daily irradiances with smoke-impacted and smoke-free flags derived from the National Oceanic and Atmospheric Administration's Hazard Mapping System (HMS) Smoke Product. Although HMS does not identify the source of smoke (e.g., wildfire, prescribed burn, agricultural), our analysis focuses on months when western U.S. and Canadian wildfire activity is greatest with most smoke traced to wildfires. We integrate satellite-derived aerosol and cloud parameters from the Multi-Angle Implementation of Atmospheric Correction (MAIAC) product and the Clouds and the Earth's Radiant Energy System (CERES). Finally, we design a model to assess PV performance given smoke impacts.

Importantly, our study reaches beyond quantifying the impact of local smoke on areas close to active fires to examine the role of both local and transported smoke in determining average solar resource availability at the regional and national level. We find considerable losses in daily mean DNI (32-44%) and GHI (11-17%) associated with localized smoke–consistent with prior studies. Local smoke can also greatly reduce monthly mean DNI (max: 61%) and GHI (max: 25%) with impacts on DNI persisting downwind of fires. However, the impact of

transported smoke on GHI is relatively minimal (< 5 %) on average over CONUS, even during an extreme wildfire season. This result implies the average impact of smoke plumes on PV resources is relatively minimal across the U.S., which is encouraging as grids incorporate more utility-scale battery storage capacity to provide greater stability when local smoke causes potentially large irradiance shifts at finer timescales.

3.2 METHODS

Below we describe the data sets and variables used in this study as well as the data processing and analysis, which were performed using Python version 3.10.

3.2.1 Irradiance data

We assessed solar resources using modeled clear-sky and all-sky DNI and GHI from the National Renewable Energy Laboratory's National Solar Radiation Database (NSRDB) (Sengupta et al., 2018) Physical Solar Model (PSM) version 3.2.2. The NSRDB combines atmospheric and land surface properties from satellite and reanalysis data in a two-step physical model. Cloud properties are derived from Geostationary Operational Environmental Satellite (GOES) observations using the Advanced Very High Resolution Radiometer (AVHRR) Pathfinder Atmospheres-Extended (PATMOS-x) algorithms. The NSRDB uses aerosol optical depths (AOD) determined using a combination of data from the Modern-Era Retrospective analysis for Research and Applications, Version 2 (MERRA-2) reanalysis product and monthly values from the Moderate Resolution Imaging Spectroradiometer (MODIS) instrument aboard the Terra and Aqua satellites. Although MERRA-2 assimilates data from MODIS, the NSRDB applies a two-fold approach to determining AOD that relies on both products. When MODIS monthly data are missing, only the MERRA-2 data are used, as is standard for the eastern and northern U.S. Otherwise, an optimal linear combination of the two data sets is computed. Surface

albedo inputs are sourced from MODIS and the Interactive Multisensor Snow and Ice Mapping System (IMS). MERRA-2 is used for all other inputs. The NSRDB regrids these data to a 4x4-km spatial resolution and interpolates to a 30-minute temporal resolution before being input into the Fast All-sky Radiation Model for Solar Applications (FARMS) (Xie et al., 2016). GHI is directly computed using FARMS, as is DNI when the sky is cloud-free. To compute DNI when clouds are present, the Direct Insolation Simulation Code (DISC) is used to decompose the DNI component of GHI. The Reference Evaluation of Solar Transmittance-2 bands (REST2) model is used for clear-sky irradiance computations (Gueymard, 2008). Comparisons to ground observations of radiation indicate a 5% bias for GHI and 10% bias for DNI with the NSRDB (Sengupta et al., 2018).

3.2.2 Smoke plume locations

We use the Hazard Mapping System (HMS) to distinguish between smoke-free and smoke-impacted days at each NSRDB grid location across CONUS. The HMS was developed by the National Oceanic and Atmospheric Administration's (NOAA) National Environmental Satellite, Data, and Information Service (NESDIS) and provides daily U.S. smoke plume locations (Ruminski et al., 2006). Analysts use visual-band imagery mainly from the National Aeronautics and Space Administration (NASA) GOES to identify smoke from wild, agricultural, and prescribed fires. No attempt is made to determine the smoke's source. Analysts manually outline plume extents and qualitatively estimate plume concentration. Occasionally, analysts use polar orbiting satellite imagery to identify smoke or infrared imagery to distinguish smoke from clouds (Rolph et al., 2009). Limitations of the HMS include difficulty distinguishing smoke from anthropogenic haze and clouds as well as uncertainty around smoke detection along plume

edges and in areas with high albedo. These limitations make the HMS a conservative estimate of plume number and extent (Brey et al., 2018).

3.2.3 Cloud and aerosol observations

We use the cloud mask and 550 nm AOD retrieval from the Multi-Angle Implementation of Atmospheric Correction (MAIAC) daily atmosphere product (MCD19A2). MAIAC processes MODIS observations from both Terra and Aqua overpasses, which capture morning (~10:30 AM LT) and afternoon (~1:30 PM LT) conditions, respectively. MAIAC uses the contrasting spatial and temporal variability of land surfaces and aerosols to improve cloud masking and retrieve 1-km resolution AOD (Lyapustin et al., 2018; Lyapustin & Wang, 2018b). Unlike other algorithms, MAIAC specifically tests for the presence of smoke, and when detected, retrieves AOD for both clear and possibly cloudy skies. This results in more AOD retrievals during smoke-impacted conditions but can increase cloud-contamination of AODs.

We combine cloud observations from MAIAC and the Clouds and the Earth's Radiant Energy System (CERES). We use the cloud mask from MAIAC to determine cloud locations on a fine spatial scale (1-km) and the CERES Synoptic 1-degree hourly (SYN1deg-1Hour) Edition 4.1 product to obtain the cloud visual optical depth. The SYN1deg cloud properties are derived from visible and infrared MODIS, Visible Infrared Imaging Radiometer Suite (VIIRS), and geostationary (GEO) satellite imagery (Minnis et al., 2011; Rutan et al., 2015; Wielicki et al., 1996). Values are spatially averaged and temporally interpolated to the SYN1deg-1Hour resolution.

3.2.4 Data processing

We downloaded the 30-minute, 4-km, yearly netCDF files for the NSRDB PSM version 3.2.2 for all years from 2006-2021 from the Registry of Open Data on Amazon Web Services

(AWS), which is part of the Department of Energy's Open Energy Data Initiative. We extracted the clear-sky DNI, clear-sky GHI, all-sky DNI, all-sky GHI, and solar zenith angle (SZA) data sets for April-October of each year and for grid locations within the 48 states comprising the contiguous U.S. The SZA values were used to filter the irradiance data sets to exclude times when the SZA is greater than 75-degrees. This removes times near sunrise and sunset when solar energy generation is low. Using a SZA filter provides consistency in analysis across time zones.

The four data products used in this analysis have different spatial and temporal resolutions. Spatially, we converted the HMS, MAIAC, and CERES data to the NSRDB 4-km grid using two spatial gridding processes. First, the HMS smoke polygons were gridded by determining if the center point (latitude, longitude) of an NSRDB grid cell was located beneath a smoke plume polygon. If a polygon overlapped an NSRDB point, the location was considered smoke-impacted, and if not, the location was considered smoke-free. Second, we mapped the MAIAC and CERES grids to the NSRDB using a nearest-neighbor approach in which the haversine distance between each grid point is calculated and the minimum distance determined. Each NSRDB location was assigned a MAIAC AOD, MAIAC cloud mask, and CERES COD based on the closest location match. A few NSRDB grid points (0.01%) had more than one matching MAIAC neighbor, and as such, an average AOD was calculated for these pixels.

Temporally, we averaged the MAIAC, CERES, and NSRDB data to the daily level of the HMS smoke product. AOD values were averaged across the different Terra and Aqua retrievals in MAIAC to determine a daily mean AOD at 550 nm. The MAIAC cloud mask classifies each pixel as cloudy, possibly cloudy, or clear. If a location is identified as cloudy or possibly cloudy in any of the Terra or Aqua retrievals for the day, we consider the location to be cloudy. The daily COD was calculated by averaging the hourly CERES COD values for times when the SZA

was less than 75-degrees. Similarly, the NSRDB 30-minute irradiance values were averaged for each day to obtain daily clear-sky and all-sky DNI and GHI. Once converted to the same spatial and temporal resolution, we merged all four data products for analysis.

3.2.5 Analysis of California case study dates

We focused on August and September when selecting dates for the case study analysis because major fire activity and smoke production in California is generally greatest during these months and was particularly so in 2020. We identified case study days based on visual examination of the NASA Worldview true-color imagery of California for all August and September days in 2019 and 2020. After manual review of these images, we selected two days in August with plumes of different optical depths in 2020 (Aug 20 AOD_{550_mean}=0.56; Aug 30 AOD_{550_mean}=0.43) and both smoke-free and clear-sky conditions in 2019. These dates allowed us to calculate smoke-driven changes in DNI (ΔDNI) and GHI (ΔGHI) by subtracting the clear-sky values in 2020 from those in 2019. Using the same date in both years better controls for variation in solar position and climate. To examine cloud-driven changes in DNI and GHI, we used two cloudy days from 2019 in September that exhibited different CODs (Sept 7 COD_{mean}=3.26; Sept 18 COD_{mean}=10.75) and were relatively smoke-free. When comparing smoke-driven irradiance changes, we limited our analysis to pixels that were both smoke-impacted in 2020 and smoke-free in 2019 based on the HMS smoke polygons. Only locations that met both conditions were included in the analysis. For cloud-driven changes, we limited our analysis to pixels that were smoke-free and cloudy or possibly cloudy. A cloud filter was not applied to the smoke-impacted days. Boxplots were used to present the distribution of either the clear-sky DNI and GHI values or the changes in DNI (ΔDNI) and GHI (ΔGHI) on each of the case study days. Smoke-driven changes were calculated by subtracting the clear-sky values in

2020 from the clear-sky values on the same day in 2019. Cloud-driven changes were calculated by subtracting the clear-sky values from the all-sky values on the same day. Negative values indicate the reduction of irradiance.

3.2.6 Analysis of monthly CONUS trends in 2019 and 2020

We computed monthly smoke frequency by summing the number of HMS-indicated smoke-impacted days at each NSRDB grid point for each month. We then calculated the difference between the number of smoke-impacted days in 2019 and 2020. Similarly, we computed the mean monthly AOD_{550} for all CONUS pixels by averaging the daily MAIAC AOD_{550} and calculated the difference between the 2019 and 2020 monthly values. For irradiance, we averaged daily clear-sky DNI and GHI to obtain the mean monthly clear-sky DNI and GHI. We then calculated the average smoke-driven changes in DNI (ΔDNI) and GHI (ΔGHI) by subtracting the monthly clear-sky value in 2019 from that in 2020 for each irradiance measure. National and regional monthly averages were then calculated for smoke frequency and irradiance from the monthly means at each grid location to summarize trends at different spatial scales.

3.2.7 Modeling photovoltaic array performance

We designed a model of a 1 MW solar PV installation to assess the change in PV output under average low smoke (2019) and high smoke (2020) conditions for September (i.e., when smoke was most abundant in 2020). To provide a comprehensive and realistically relevant analysis of PV performance under non-standard (i.e., real world) conditions, we used monthly mean irradiance values computed in this study for low and high smoke years as input. Based on the computed clear-sky DNI and GHI values, we derived the solar cell temperature since different solar panel technologies exhibit different temperature dependencies, and thus, different temperature coefficients for each PV technology. Below is a detailed description of the model

design and relevant computations for evaluating the performance of the PV modules under different conditions (PV model development conducted by co-author Dr. Amit Munshi).

Traditionally, all PV modules are tested and their performance is rated under standard test conditions (STC) (Osterwald, 2003). The STC for terrestrial solar panels include:

- Irradiance Level: 1000 W/m²

  A solar radiation intensity of 1000 W/m² is approximately the average solar radiation level on a clear day at noon.

- Cell Temperature: 25°C (or 77°F)

  This refers to the temperature of the solar cells themselves, not the ambient temperature. Solar panels typically operate at higher temperatures in real-world conditions, but the STC rating is based on this standardized cell temperature.

- Air Mass: 1.5

  This factor represents the spectral distribution of the sunlight and is a measure of the path length through the Earth's atmosphere. An air mass of 1.5 approximates the sun's angle in the sky in mid-latitudes during an average day.

The temperature coefficient of solar panels is a measure of how much a solar panel's performance is affected by changes in temperature. Specifically, the measure quantifies the change in electrical output (usually power or voltage) for each degree Celsius (°C) rise in temperature above a standard reference point, typically 25°C (STC) and is expressed as a percentage change per degree Celsius (%/°C). For example, a temperature coefficient of -0.3%/°C means that for each degree Celsius increase in temperature above 25°C, the solar panel's output power decreases by 0.3%. The temperature coefficient is specified via

$$Temperature\ Coefficient = \frac{Output\ at\ Operating\ Temperature - Output\ at\ STC}{(Operating\ Temperature - STC\ Temperature) \times Output\ at\ STC}, \text{ (eq. 1)}$$

Often, the operating temperatures for PV panels significantly exceeds the STC with temperatures over 65°C in hot desert climates and reaching 35-45°C even in cold or arctic climates. Therefore, we account for the effect of operating temperatures on performance when evaluating the effect of smoke on the performance of PV panels using two methods. First, we used a model operating temperature calculator available online at pveducation.org, which relies solely on the ambient air temperature to estimate the module operating temperature (*Nominal Operating Cell Temperature*, n.d.). Operating temperature is calculated using the relationship

$$T_{cell} = T_{air} + \frac{NOCT-20}{80} S, \text{ (eq. 2)}$$

where T_{cell} is the operating temperature of the PV cell or module. NOCT is Nominal Operating Cell Temperature, defined as the temperature reached by open circuited cells in a PV module under incident irradiance of 800 W/m^2, air temperature of 20°C, wind velocity of 1 m/s, and the assumption that the panel is mounted such that the back surface of the panel is exposed to air (e.g., as opposed to residential mountings where the roof covers the back surface). *S* is the insolation in mW/cm^2, and in the context of PV panels, refers to the amount of solar radiation energy received on a given surface area in a given amount of time. The fraction (NOCT-20)/80 represents the rate at which the cell temperature increases per unit increase in solar irradiance above a baseline of 20°C at an irradiance of 800 W/m^2. When using equation 2, the actual module temperature will be lower than calculated when wind velocity is high and higher under still conditions (R. G. Ross Jr, 1980; R. Ross & Smokler, 1986).

Second, a more accurate estimate for operating temperature of PV panels in the field can be calculated using the relationship

$$T_{panel} = T_{ambient} + \frac{NOCT-20}{800} \times GHI \times Wind\ Factor, \text{ (eq. 3)}$$

where T_{panel} is the solar panel operating temperature, $T_{ambient}$ is the ambient temperature, GHI is the Global Horizontal Irradiance, and the Wind Factor is a term that accounts for the cooling effect of the wind (Tahir et al., 2022). We approximated the Wind Factor as

$$Wind\ Factor = Wind\ Coefficient \times (Wind\ Speed - 1), \text{ (eq. 4)}$$

where the wind coefficient parameter depends on the installation specifics and panel type.

For our simulations, we evaluate panel performance at 12 locations for the month of September in 2019 and 2020. As inputs, we used the monthly mean clear-sky GHI calculated in the current study; normalized NOCT values of 46°C for c-Si PV and 45°C for CdTe PV; and temperature coefficients of -0.45% for c-Si and -0.21% for CdTe (Appelbaum & Maor, 2020). We assume a 1 MW solar installation of each solar PV (c-Si and CdTe) system modeled. The highest reported record efficiencies for each panel technology were used (i.e., 24.5% and 20.2% for c-Si and CdTe, respectively). Under STC, the solar panel efficiency equates to the percent of incident irradiance that would be efficiently converted to useful electrical power (Green et al., 2023). In other words, at 25°C and 1000 W/m^2 incident solar irradiance, c-Si and CdTe PV modules were assumed to produce 245 Wp and 202 Wp per meter square of the PV module, respectively. Hence, the total area required for 1 MW installation for c-Si and CdTe PV was estimated to be 4081.63 m^2 and 4950.5 m^2, respectively. For a better perspective, this is approximately the volume of solar PV installation that can power houses for about 130 American families.

The ambient temperatures and wind speeds were drawn from the NSRDB. Considering only daytime hours (i.e., when enough solar irradiance was available to produce measurable PV power output), we calculated the average ambient temperature and wind speed for September across both years. We averaged across 2019 and 2020 to ensure that changes in operating

temperature resulted from smoke-driven GHI adjustments rather than independent meteorological conditions in a given year. We then calculated the average PV panel operating temperatures. Ultimately, the following outputs were modeled for each location in 2019 and 2020 for c-Si and CdTe solar panels:

- *Power Output with DNI at 25°C:* estimate of power output considering only clear-sky DNI, which excludes the impact of clouds, operating temperatures, and diffuse radiation but includes the impact of smoke.
- *Power Output with GHI at 25°C:* estimate of the power output under more realistic conditions while excluding the effects of temperature on PV performance.
- *Power Output Including Wind and GHI in Temperature Calculation:* the most realistic evaluation of power output considering the wind speed (cools solar panels) and actual clear-sky GHI (heats solar panels), calculated using Equation 3.
- *Power Output Excluding Wind and GHI from Temperature Calculation:* evaluation of power output using the online panel temperature calculator and Equation 2 (i.e., does not account for GHI and wind-driven changes in panel temperature; estimated PV module temperature based solely on ambient temperature).

3.2.8 Analysis of longitudinal data from 2006-2021

Using the daily mean clear-sky DNI and GHI, we calculated the mean DNI and GHI values for each of the six regions considered for all days from 2006-2021. We computed fractional smoke coverage for each region on these days by determining the number of pixels flagged as smoke-impacted relative to the total number of pixels in the region.

3.3 RESULTS

3.3.1 California 2020 case study: localized smoke-irradiance interactions

Driven by increased aridity (Higuera & Abatzoglou, 2021), the 2020 wildfire season set records for acres burned in California (Safford et al., 2022), and previous studies and news articles documented the resulting large reductions in PV output (e.g., Donaldson et al., 2021). We compared clear-sky DNI and GHI across California on two smoke-impacted days in 2020 to analogous smoke-free conditions on the same days in 2019 (Figure 3.1). We selected August 20 and 30 for comparison since both days featured 1) expansive smoke plumes in 2020, 2) minimal cloud cover in 2019 and 2020, 3) different mean AOD values, and 4) no smoke in 2019. This exercise demonstrates how smoke affects daily irradiance and how optical thickness modulates the effect. We then compare these smoke-driven changes to cloud-driven irradiance changes on two cloudy days in 2019 with differing optical depths (Figure 3.2). We selected September 7 and 18 as our cloudy, smoke-free reference days due to the variability in cloud optical depth (COD) and abundance of clouds in an area where clouds are rare in August and September.

3.3.2 Variation with aerosol optical depth

The impact of wildfire smoke plumes on AOD varies substantially, resulting in large differences in how plumes affect DNI and GHI. In 2020, the AOD at 550 nm (AOD_{550}) in smoke-impacted locations averaged 0.56 on August 20 (median: 0.40; range: 0.01-2.29; n=21,541 4-km grid cells) and 0.43 on August 30 (median: 0.32; range: 0.01-2.37; n=15,322 4-km grid cells). Mean DNI declined 42% under the optically thicker smoke and 32% under the optically thinner smoke (Figure 3.1). Decreases in GHI were smaller under optically thicker (-17%) and thinner (-11%) smoke conditions and similar to PV output reductions documented during a similar timeframe (Donaldson et al., 2021). On average, the 0.13 increase in AOD

resulted in a 10-point greater decrease in DNI compared to a 6-point difference in GHI. Additionally, the DNI and GHI distributions shifted lower when smoke was overhead with no overlap between the interquartile ranges of smoke-free and smoke-impacted locations. At most, clear-sky DNI declined 86% due to smoke to 118-127 W/m^2 (n=42) and clear-sky GHI declined 51% to 330-337 W/m^2 (n=50). Overall, smoke reduced clear-sky DNI more than clear-sky GHI and the influence of optical depth was more pronounced for DNI than GHI.

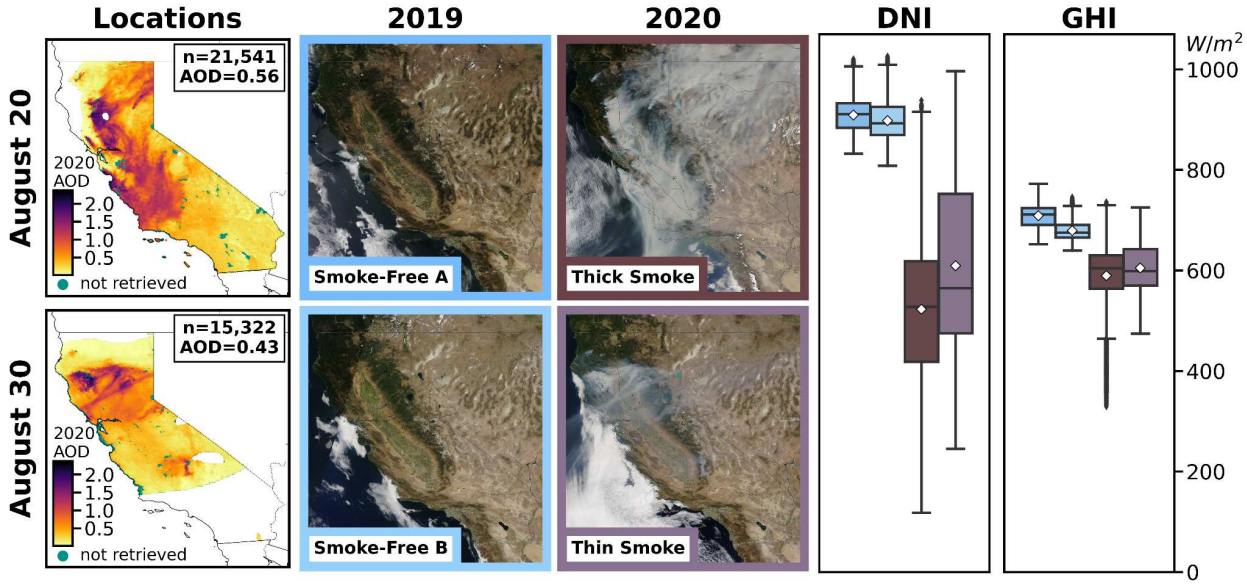

Figure 3.1: Comparison of smoke, aerosol, and irradiance conditions on August 20 (top row) and August 30 (bottom row) in 2019 and 2020 across California. Optically thinner (light purple; 8/30/2020) and thicker (brown; 8/20/2020) wildfire smoke in 2020 are contrasted against clear-sky analogues from 2019 (blue shades). Locations included in the analysis (left map column) are indicated along with the corresponding change in the mean daily MAIAC AOD at 550 nm between the smoke-free day in 2019 and the same smoke-impacted day in 2020. Only California locations that were smoke-free in 2019 and smoke-impacted in 2020 were included in the analysis. Corrected reflectance true-color imagery from the Terra MODIS instrument (NASA Worldview Snapshot) for each date examined is shown (second and third column) with the image border color corresponding to the associated color in the box plot (right). The box plots show the distribution of daily average clear-sky DNI and GHI including the median value (black line), mean (white diamonds), first quartile (box bottom), third quartile (box top), and range (whiskers) excluding outliers (data beyond 1.5 times the interquartile range).

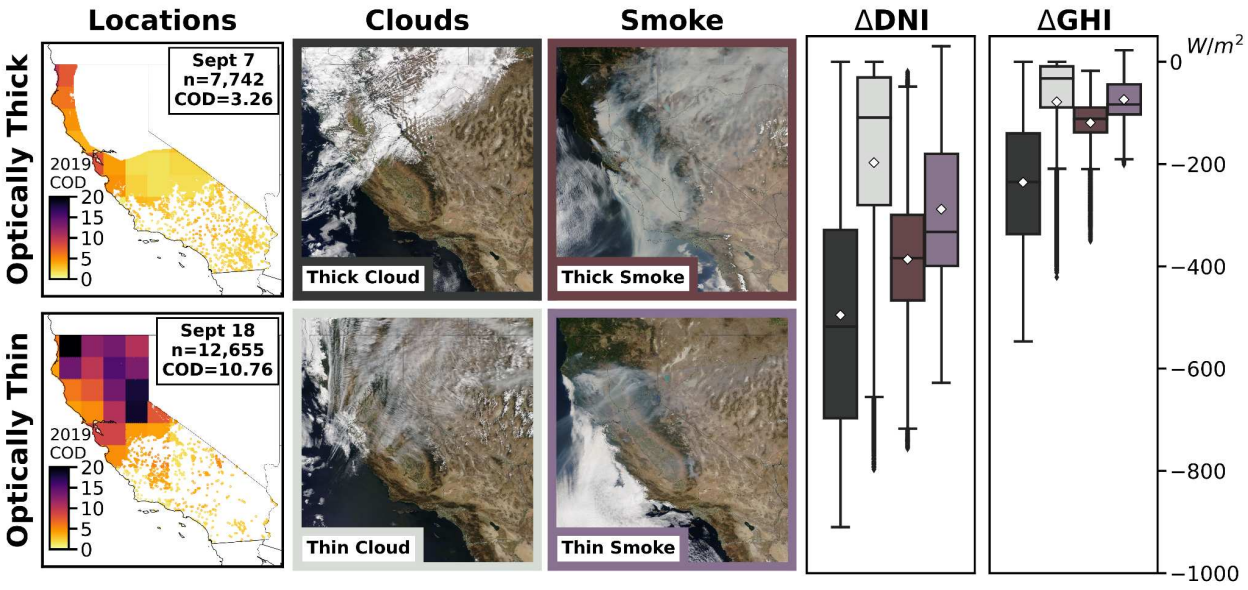

Figure 3.2: Comparison of smoke, clouds, and irradiance conditions on four days in 2019 and 2020 across California. Change in irradiance at locations experiencing optically thinner (light purple; 8/30/2020) and thicker (brown; 8/20/2020) wildfire smoke in 2020 are contrasted with similar smoke-free locations with optically thin (light gray; 9/7/2019) and thick (dark gray; 9/18/2019) clouds in 2019. Locations included in the analysis (left map column) are indicated along with the corresponding mean daily COD calculated from the CERES SYN1deg-1Hour product on 9/7 (bottom) and 9/18 (top). Areas that were smoke-impacted in 2019 in the cloudy scenes were omitted from the analysis. Corrected reflectance true-color imagery from the Terra MODIS instrument (NASA Worldview Snapshot) for each date examined is shown (second and third column) with the image border color corresponding to the associated color in the box plot (right). The box plots show the distribution of changes in daily average clear-sky DNI and GHI including the median change (black line), mean (white diamonds), first quartile (box bottom), third quartile (box top), and range (whiskers) excluding outliers (data beyond 1.5 times the interquartile range).

3.3.3 Smoke-driven vs. cloud-driven changes

Clouds introduce substantial variability into solar energy forecasts as the exact impact of clouds on generation depends on multiple factors including cloud coverage, type, shape, optical depth, altitude, and speed (Barbieri et al., 2017; Kankiewicz et al., 2010; Kern et al., 1989; Lappalainen & Valkealahti, 2015, 2016; Lau et al., 2015). Clouds scatter light more efficiently than smoke plumes and can reach far greater optical depths. In California, summertime clouds are infrequent, but smoke impacts are becoming commonplace, raising the question of whether smoke is effectively increasing the number of "cloudy" days. We compared smoke-driven

changes in DNI (ΔDNI) and GHI (ΔGHI) at two AODs to cloud-driven changes under average CODs of 3.26 (Sept 7: range=0.99-9.56; n=7,742) and 10.76 (Sept 18: range COD=1.12-21.92, n=12,655). ΔDNI_{smoke} and ΔGHI_{smoke} refer to the difference between the clear-sky values on the smoke-impacted and smoke-free days from the previous section (Aug 20, Aug 30). ΔDNI_{cloud} and ΔGHI_{cloud} indicate the difference between the clear-sky and all-sky values for 2019 cloudy scenes.

On all days considered, ΔDNI exceeded ΔGHI (Figure 3.2) due to the heightened sensitivity of DNI to cloud droplets and aerosol particles. Shifts in the means, medians, and interquartile ranges were more negative for optically thicker smoke and clouds than optically thinner smoke and clouds, respectively. Compared to smoke, clouds created a wider range of daily ΔDNI and ΔGHI values, and the maximum cloud-driven reduction far exceeded the maximum smoke-driven reduction. Clear-sky DNI losses reached -910 W/m^2 for thicker clouds and -797 W/m^2 for thinner clouds compared to -756 W/m^2 for thicker smoke. GHI losses reached -547 W/m^2 for thicker clouds and -421 W/m^2 for thinner clouds compared to -350 W/m^2 for thicker smoke. For context, PV panel efficiency is tested using a standard irradiance value of 1000 W/m^2. For both metrics, and particularly for GHI, thinner smoke and clouds resulted in similar irradiance reductions given the overlapping interquartile ranges. Occasionally, thicker smoke achieved reductions similar to thicker clouds, but in general, thicker clouds created larger reductions than smoke. However, thicker smoke typically drove similar or greater losses than thinner clouds. Since localized wildfire smoke can persist in an area longer than clouds–which develop, move, and dissipate throughout the day, limiting their impact–the collective effect of increased smoke and relatively cloud-free conditions functionally increased the number of cloudy days in California in 2020.

3.3.4 2020 future conditions analogue aggregate analysis

Exceptional fire years like 2020 will become more frequent as the west continues to warm (Coop et al., 2022) and relatively low fire years like 2019 will stand as reminders of past conditions. Here we contrast 2020 and 2019 as an analogue for predicting future smoke impacts on solar resources relative to more traditional smoke conditions. Since smoke is present every year from diverse sources including wildfires, prescribed burns, and agricultural fires, we focus on low and high smoke conditions rather than smoke-impacted and smoke-free conditions. Smoke-impacted days increased from 2019 to 2020 across 72% of CONUS in August (Figure 3.3.a) and 88% in September (Figure 3.3.b). In 2020, the percentage of CONUS experiencing smoke overhead for at least 15 days was 22% in August (2019: 1%) and 40% in September (2019: 4%). The percentage experiencing smoke for at least eight days was 38% in August (2019: 17%) and 47% in September (2019: 15%). As wildfires grew across California, Oregon, Washington, and Colorado, smoke was transported farther north and east leading to a widespread increase in smoke-impacted days.

AOD provides context for interpreting surface-level irradiance changes since extinction efficiency varies with smoke particle density, plume vertical extent, and composition. Smoke-driven changes in CONUS monthly mean AOD_{550} were minor in August (Figure 3.3.c), increasing 23% from 0.13 in 2019 to 0.16 in 2020. More substantial changes occurred in September (Figure 3.3.d) when mean AOD_{550} increased 127% from 0.11 to 0.25. Few areas surpassed an AOD_{550} of 0.5 in August 2019 (< 0.01%), September 2019 (< 0.01%), or August 2020 (0.08%). However, in September 2020, AOD_{550} exceeded 0.5 across 3% of CONUS, in areas close to active fires. Even as smoke-impacted days increased in August, mean AOD_{550}

remained relatively stable, but the more substantial increase in smoke frequency in September was associated with a more than doubling of the mean CONUS AOD_{550}.

As smoke frequency and AOD_{550} increased, modeled clear-sky DNI (Figure 3.3.e/f) and GHI (Figure 3.3.g/h) typically decreased, particularly in areas close to large wildfires in California and Colorado in August and California, Colorado, Oregon, and Washington in

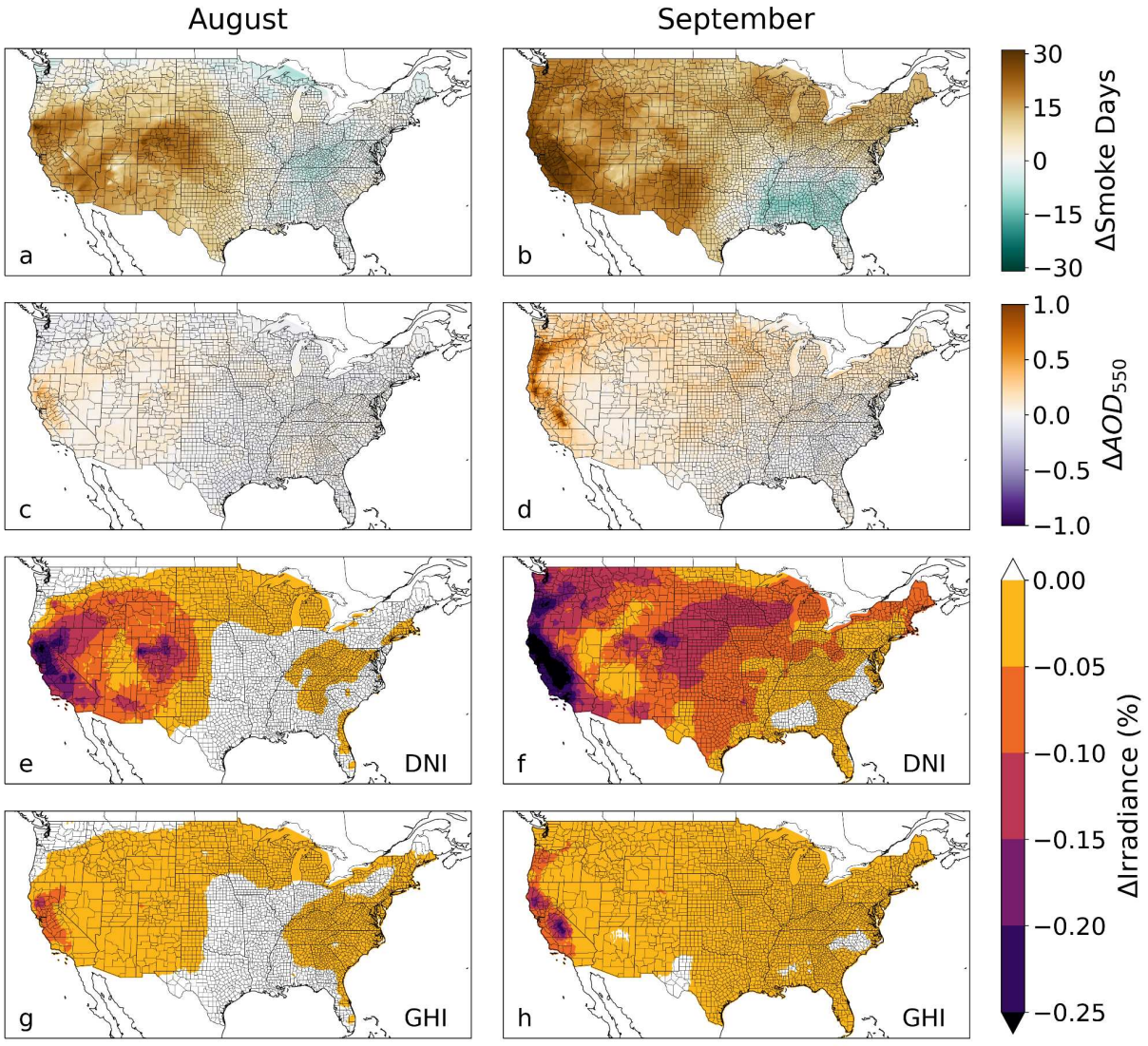

Figure 3.3: Change in smoke, aerosol, and irradiance metrics from 2019 to 2020 for August (left column) and September (right column). Specifically, the change in the number of smoke-impacted days (a, b), change in monthly mean AOD at 550 nm (c, d), and percent decrease in surface-level mean clear-sky DNI (e, f) and GHI (g, h).

September. For clear-sky DNI, monthly means decreased across 63% of CONUS in August (Figure 3.3.e) and 96% in September (Figure 3.3.f). In August, mean clear-sky DNI decreased over 20% in areas of California (max: 30%; 255 W/m^2) and Colorado (max: 24%; 203 W/m^2) near active wildfires. In September, average losses exceeded 20% across much of California (max: 61%; 483 W/m^2) and in parts of Oregon (max: 29%; 238 W/m^2), Northern Colorado (max: 24%; 225 W/m^2), and Southern Wyoming (max: 25%; 229 W/m^2). Clear-sky DNI losses reached 40-60% in some areas of California's Central Valley and Northern Coastal Ranges. DNI reductions persisted downwind to affect areas far from emission sources but within the transport pathway for western wildfire smoke. In September, clear-sky DNI decreased 5-10% as far east as Maine and 10-15% in Nebraska and parts of South Dakota, Minnesota, Iowa, Wisconsin, Kansas and Texas.

Mean clear-sky GHI (Figure 3.3.g/h) decreased less than DNI, but spatial trends in GHI losses largely mirrored those for DNI. In 2020, clear-sky GHI decreased across 66% of CONUS in August and 95% in September. On average, reductions were < 5% in nearly all areas (≥ 95%) that experienced GHI losses in August and September. The largest reductions occurred in California. By percent, the greatest decrease was 12% in August and 25% in September, and by value, the greatest decrease was 83 W/m^2 in August and 156 W/m^2 in September. While substantial reductions in clear-sky GHI occurred across California, Oregon, and Colorado, severe decreases were restricted to areas immediately adjacent to large wildfires (e.g., California Central Valley and Coastal Ranges; Oregon Willamette Valley and Coast Range). Outside these areas, the reduction in monthly mean clear-sky GHI was minimal (< 5%), which indicates that monthly mean clear-sky GHI changes little with increased smoke in areas primarily affected by transported plumes.

Figure 3.4 summarizes how monthly mean irradiance changed alongside smoke frequency at the national and regional scale for the entire wildfire season (April-October). Nationally, clear-sky DNI varied with changes in smoke frequency throughout the fire season, while clear-sky GHI remained relatively stable (Figure 3.4.a). Early in the season (April-July), the average number of smoke-impacted days across CONUS was the same or slightly lower in 2020 and irradiance was slightly higher (maximum increase of 2.5% for clear-sky DNI and 0.8% for clear-sky GHI). Later in the season (August-October), 2020's smoke-impacted days far exceeded 2019's with the average number of smoke-impacted days more than doubling in

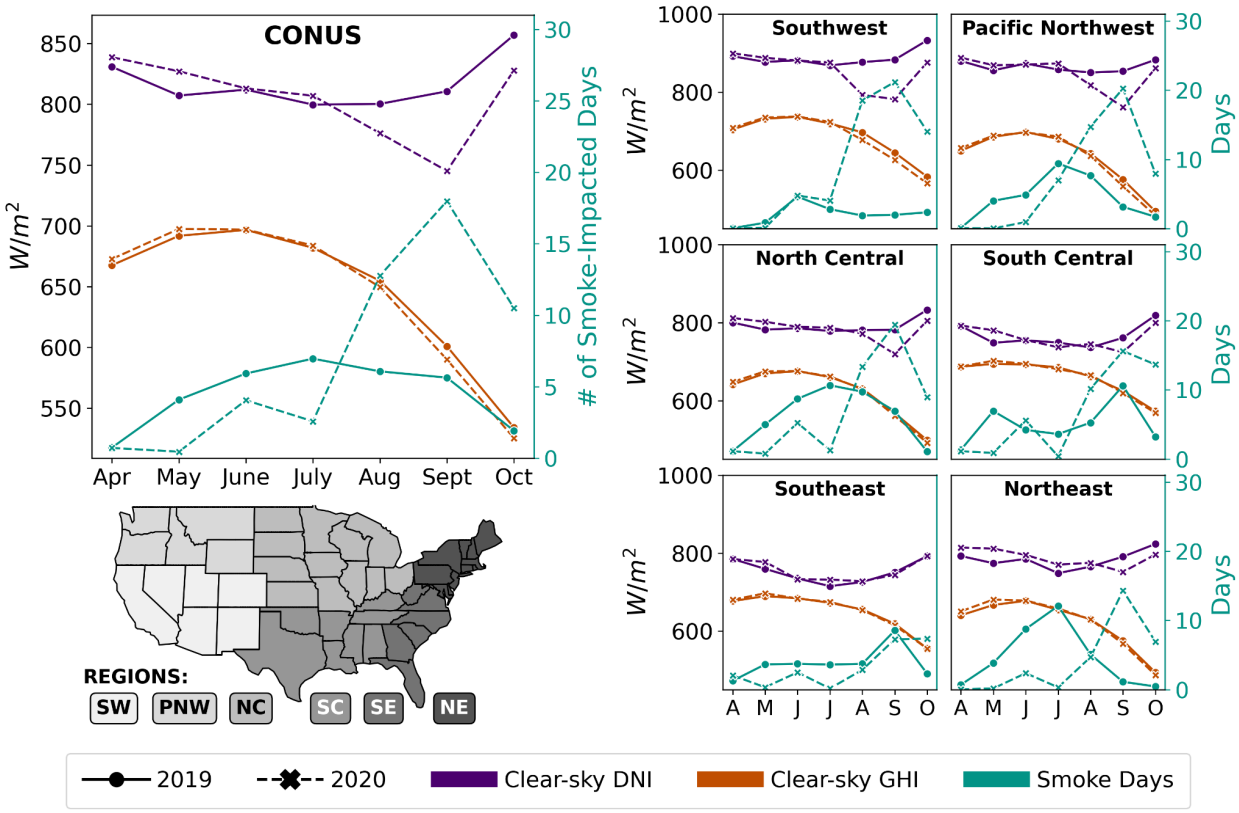

Figure 3.4: Average monthly number of smoke-impacted days (teal), surface-level mean clear-sky DNI (purple), and surface-level mean clear-sky GHI (orange) in 2019 (solid) and 2020 (dashed) nationally (far left) and aggregated by region (six right panels). A map of the different regions is presented (lower left) showing the Southwest (SW), Pacific Northwest (PNW), North Central (NC), South Central (SC), Southeast (SE), and Northeast (NE).

August (110%) and more than tripling in September (219%). Corresponding clear-sky DNI decreased by 3% and 8% while clear-sky GHI decreased by 1% and 2%, respectively. The decreases in CONUS-averaged clear-sky irradiance were relatively small compared to the large increases in smoke frequency, especially when considering GHI.

Regionally, smoke frequency increased and clear-sky irradiance decreased in the late summer and early fall, particularly in the Southwest (SW), Pacific Northwest (PNW), and North Central (NC) regions. (Figure 3.4.b-d). The SW recorded the largest rise in smoke-impacted days of any region, increasing by 16.6 days in August (+882%) and 19.2 days in September (+963%). The largest decrease in clear-sky irradiance during these months also occurred in the SW with DNI losses of 10% in August and 12% in September and GHI losses of 3% in both months. In September, smoke-impacted days increased substantially in the PNW (+544%), NC (+180%), and Northeast (NE; +1169%) regions; clear-sky DNI decreased 11%, 8%, and 5%, respectively; and clear-sky GHI decreased 3%, 1%, and 1%, respectively. Weaker trends in smoke frequency and irradiance characterized the South Central (SC) and Southeast (SE) regions. Overall, trends in the SW, PNW, and NC regions largely drove the variation in CONUS averages (Figure 3.4.a). Additionally, the limited fluctuations in GHI across a wide range of smoke frequencies indicate relative stability in the baseline (i.e., average) resource for PV.

We focus on smoke-driven irradiance shifts, but the main societal concern is how much these changes, particularly in GHI, affect PV power output. We modeled average daily output at an idealized 1 MW stationary PV installation for September 2019 and 2020 at 13 locations across CONUS using the monthly mean clear-sky DNI and GHI computed in this study (Appendix Table A2.1). Below we present results assuming c-Si panels (Figure 3.5), and results for CdTe panels are provided in Appendix Figure A2.1. Under standard test conditions (STC;

25°C, air mass 1.5), power loss is greatest in areas near active wildfires with optically dense, persistent smoke plumes (Figure 3.5). For example, given an 11% or 65 W/m^2 reduction in mean September GHI in Modesto, CA (2019 baseline: 620 W/m^2), the model projects an 11% (-6.6

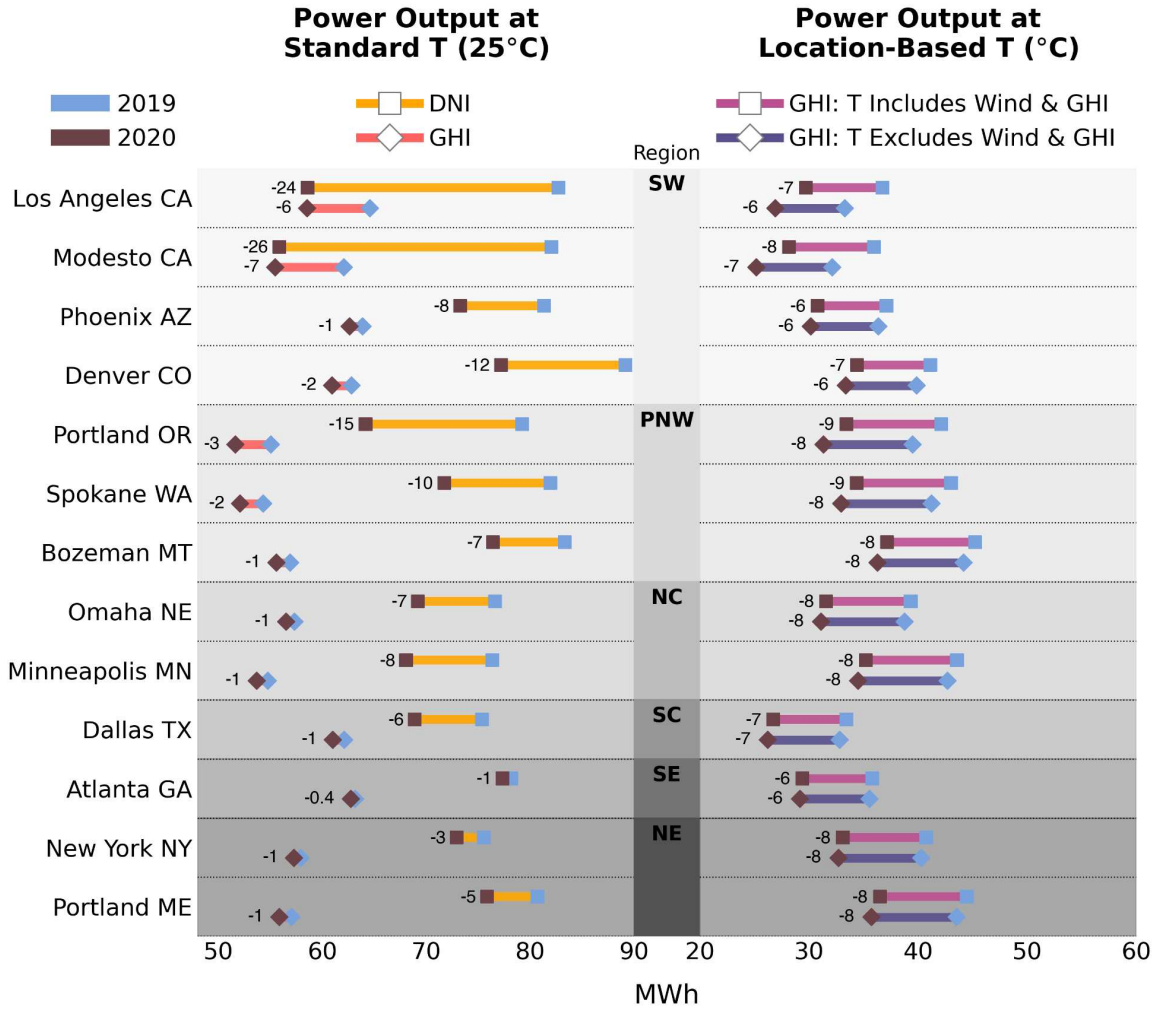

Figure 3.5: Comparison of modeled average daytime power output (MWh) in September for 1 MW PV installations of c-Si panels at 13 locations across CONUS in a low (blue; 2019) and high (brown; 2020) smoke year. Site region is indicated with grayscale shading consistent with the map in Figure 3.4. Power output was modeled using four approaches: two with panel temperatures set to a standard temperature of 25°C (left panel) and two with panel temperatures determined by location (right panel). At 25°C, power output was modeled using clear-sky DNI (orange) and clear-sky GHI (red) as the irradiance input. At location-based temperatures, power output was modeled using clear-sky GHI as the irradiance input, but temperature was determined either including (light purple) or excluding (dark purple) the cooling effects of wind and warming effects of radiation. The clear-sky DNI and GHI for each location were determined using the data underlying Figure 3.3 and are reported in Appendix Table A2.1. Results for the second most common panel material, CdTe, are provided in Appendix Figure A2.1.

MWh) reduction in average daily power output. PV output reductions are substantially lower (~1 MWh) in areas with optically thinner, transported smoke plumes (e.g., NC, SC, and NE regions). However, using the STC ignores how site location, wind conditions, and smoke-driven reductions in surface radiation influence panel temperature, which greatly affects PV performance as panels operate more efficiently at lower temperatures (Dubey et al., 2013; Skoplaki & Palyvos, 2009). Accounting for location-specific temperatures, the reduction in power output becomes more consistent across CONUS ranging from 6-9 MWh (16-22%). Although variability is minimal, the SW, SC, and SE locations experienced slightly smaller reductions (6-7 MWh) in power output than the PNW, NC, and NE locations (8-9 MWh). Southern sites may benefit more from increased panel efficiency as smoke reduces temperatures, compared to northern sites where baseline temperatures are lower.

3.3.5 Smoke-irradiance interactions across CONUS from 2006-2021

Although smoke conditions in 2020 exemplify potential future conditions, U.S. wildfire activity has been increasing since the mid-1980s (Abatzoglou & Williams, 2016; Westerling, 2016; Westerling et al., 2006). As such, we examined trends in mean daily smoke spatial coverage and clear-sky irradiance at the regional level from 2006-2021 for August (Figure 3.6) and September (Figure 3.7). Smoke coverage refers to the average fraction of a region that was categorized as smoke-impacted by HMS at the daily level for each month. Similarly, mean irradiance refers to the average clear-sky DNI and GHI at the daily level for each month. This longitudinal analysis better constrains the impact of smoke on baseline (i.e., average) resources given spatio-temporal variations in smoke extent and optical properties. As in the previous two sections, clear-sky DNI showed greater sensitivity to smoke than clear-sky GHI.

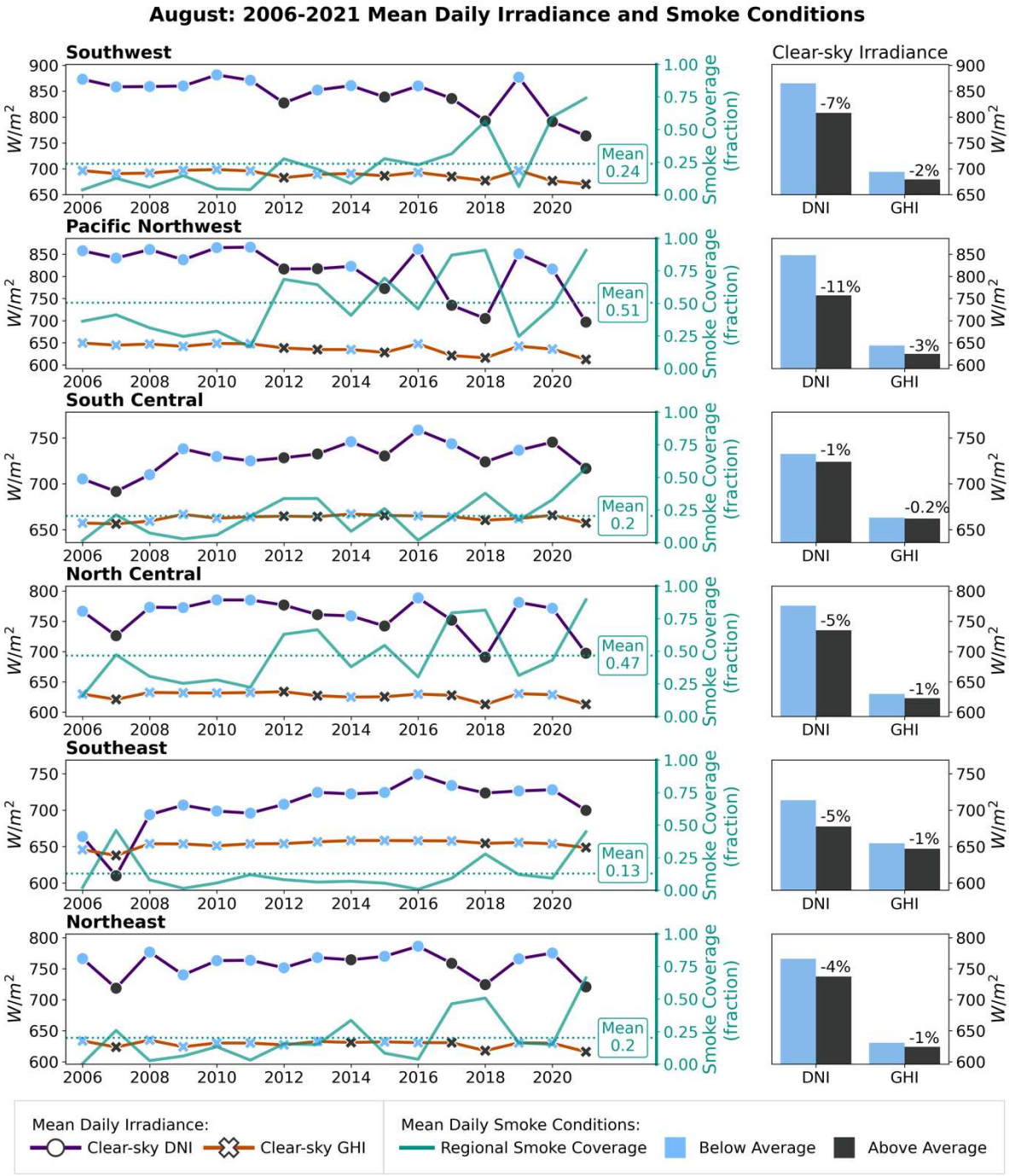

Figure 3.6: Timeseries (left) of the August daily mean smoke coverage (teal line), clear-sky DNI (purple line with circles), and clear-sky GHI (orange line with x's) for each CONUS region from 2006-2021. Smoke coverage refers to the fraction of each region that was smoke-impacted on a given day. The mean smoke coverage for each region is indicated by a dashed teal line and text. Bar plots (right) of the August mean clear-sky DNI and GHI during years with below-average (light blue) and above-average (dark grey) smoke coverage conditions. The percent change is indicated above the respective bars.

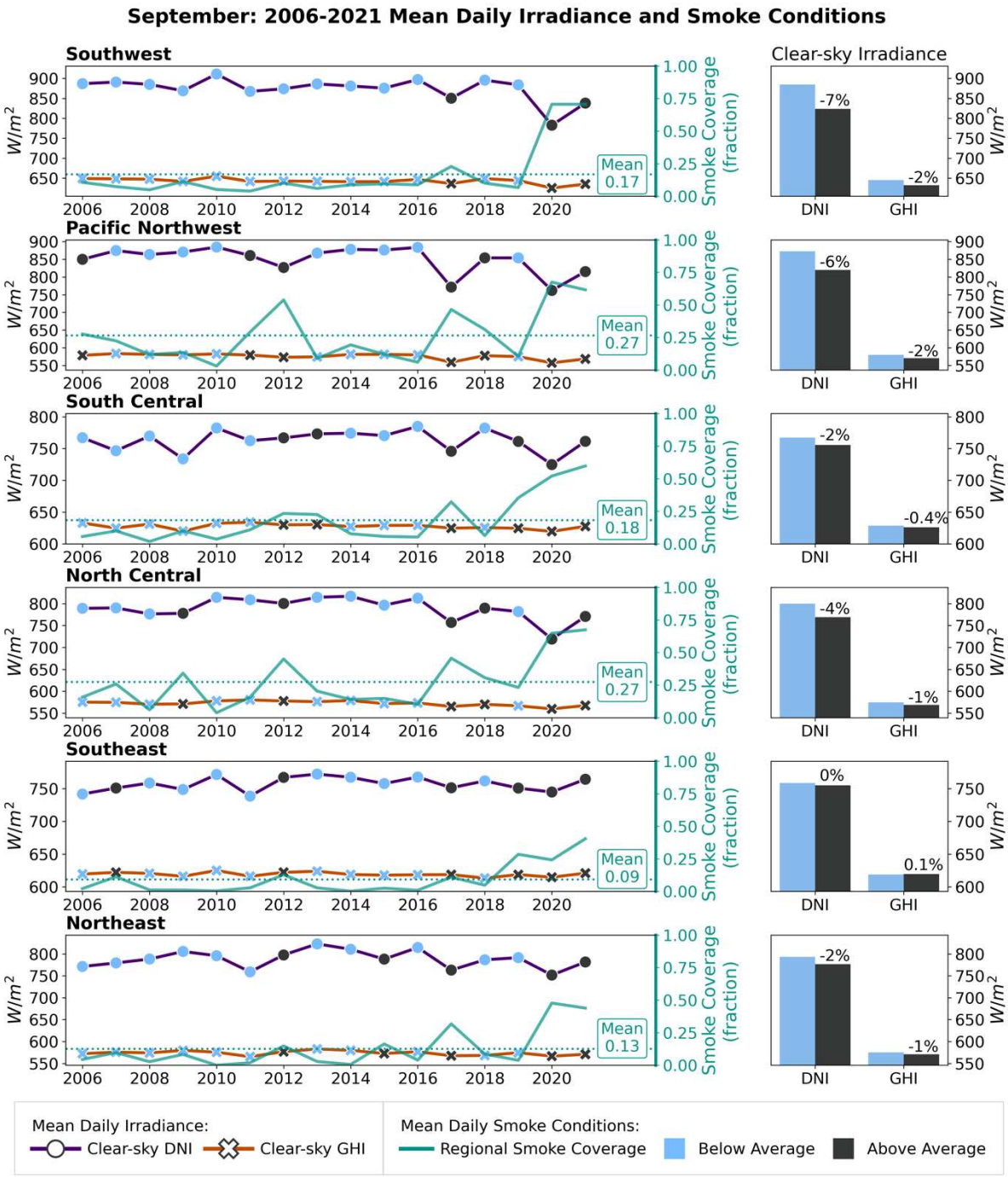

Figure 3.7: Timeseries (left) of the September daily mean smoke coverage (teal line), clear-sky DNI (purple line with circles), and clear-sky GHI (orange line with x's) for each CONUS region from 2006-2021. Smoke coverage refers to the fraction of each region that was smoke-impacted on a given day. The mean smoke coverage for each region is indicated by a dashed teal line and text. Bar plots (right) of the September mean clear-sky DNI and GHI during years with below-average (light blue) and above-average (dark grey) smoke coverage conditions. The percent change is indicated above the respective bars.

Mean clear-sky DNI exhibited considerable variability over time and larger differences between below-average and above-average smoke years. During years with above-average smoke coverage, DNI reductions were largest in the SW (August: -7%; September: -7%) and PNW (August: -11%; September: -6%), regions affected by fresh, optically thick smoke plumes from local wildfires (Brey et al., 2018; Corwin et al., 2022). Following 2017, prominent extremes in smoke coverage and DNI variability occurred in the SW and PNW, highlighting the impact of recent severe wildfire seasons. Earlier years exhibited greater stability in clear-sky DNI resources. Average smoke coverage was greatest in the PNW (August: 51%; September 27%) and NC regions (August: 47%; September: 27%), with the latter influenced primarily by transported smoke. Despite similar smoke coverage levels, the decline in clear-sky DNI was less pronounced in the NC region (August: -5%; September: -4%) due to differences in the density and optical properties of the smoke over each region. Overall, clear-sky DNI was more sensitivity to plume size (i.e., regional coverage) in areas where plumes were denser, a characteristic of areas near active fires where smoke is fresher. Clear-sky DNI was less sensitive to regional smoke coverage in areas with optically thin, laterally extensive, dilute, aged plumes overhead, such as the NC, SC, NE, and SE regions.

Regional clear-sky GHI remained remarkably stable across the 16-year timeframe analyzed regardless of smoke coverage conditions. During above-average smoke years, each region's mean clear-sky GHI decreased by 3% or less compared to below-average smoke years. GHI declines peaked at 3% in August in the PNW and 2% in September in the PNW and SW. Regions mainly affected by transported smoke experienced decreases in clear-sky GHI of 1% of less during both months. Ultimately, smoke failed to drive major shifts in regional monthly mean clear-sky GHI.

3.4 DISCUSSION

We examine the historical impact of smoke, particularly wildfire smoke, on two irradiance parameters–DNI and GHI–relevant for solar energy production at different spatial and temporal scales. Consistent with prior studies, solar resources decline substantially under local optically thick smoke. However, transported smoke that extends across CONUS minimally affects baseline monthly mean GHI in the underlying regions, even during extreme wildfire seasons. Thus, while most other studies report that smoke will negatively affect solar PV generation on a day-to-day or minute-to-minute basis (Donaldson et al., 2021; Gómez-Amo et al., 2019; Juliano et al., 2022; e.g., Perry & Troccoli, 2015), we demonstrate through an expanded CONUS-wide analysis of a longer time horizon that, on average, smoke will not greatly affect baseline solar PV resource availability. Although transported smoke increasingly affects larger areas, the long-term stability of GHI resources with regard to smoke supports continued PV development alongside the growth of utility scale battery storage capacity to address short-term smoke impacts from local fires. Resources for CSP production (i.e., DNI), show greater sensitivity to local and transported smoke–particularly to fresh, dense, local plumes–but CSP represents a relatively small portion of U.S. solar production.

Local smoke can substantially decrease surface-level clear-sky DNI and GHI during severe wildfire events. Using daily case studies with thick smoke (AOD_{550} 0.43-0.56), we show average clear-sky DNI for California declined 32-42% and clear-sky GHI declined 11-17%, which is consistent with reductions in PV output of ~10% modeled at an AOD of 0.5 at ten southern California PV plants in 2020 (Donaldson et al., 2021). While average GHI reductions of 11-17% can substantially impact the power grid, the spatial variability of smoke means that some areas may see GHI reduced by half. Such a loss represents an important risk to PV production in

California, particularly since clouds are rare, irradiance is high, and demand is at its peak during the summer. More wildfire smoke could increase the need for typically dirtier and more expensive natural gas generation or battery storage.

Lofted smoke from western U.S. and Canadian wildfires frequently travels across CONUS (Brey et al., 2018). As such, understanding how smoke may affect solar energy production requires looking beyond the influence of local fires on adjacent PV installations. Comparing the heavy smoke season of 2020 to the more traditional smoke season of 2019, monthly mean clear-sky DNI and GHI decreased across CONUS as smoke frequency increased in August and September. Clear-sky DNI was more sensitive to smoke than clear-sky GHI. Local smoke was associated with clear-sky DNI reductions of over 20% in the SW and PNW, with losses reaching 50-60% in parts of California. Reductions in clear-sky DNI persisted into areas affected by transported smoke, decreasing by 10-15% in parts of the NC region and 5-10% in parts of the SC and NE regions. In contrast, clear-sky GHI reductions amounted to < 5% in areas affected by transported smoke. Ultimately, in a heavily smoke-impacted season indicative of potential future conditions, regional and national declines in monthly mean clear-sky GHI were small. However, locations near large fires remained at risk of substantial resource losses given the large decrease in GHI (>10%) in areas of the SW, where solar potential and production are greatest.

Similar patterns emerged over longer timescales. Clear-sky DNI was more sensitive to changes in regional smoke coverage compared to clear-sky GHI. Smoke-irradiance trends were strongest in the SW and PNW where plumes are typically optically thicker and fresher. Regional clear-sky DNI decreased 6-11% in the SW and PNW in August and September during years with above-average smoke coverage. The PNW region experienced the highest smoke coverage rates

given the abundance of both local and transported smoke. The NC region experienced similar smoke coverage rates with predominantly transported smoke but lacked substantial reductions in DNI. In general, clear-sky DNI decreased by 5% or less in regions mainly affected by transported smoke (i.e., the SE, NC, NE, and SC regions). In contrast, clear-sky GHI decreased little, if at all, with varying smoke coverage. GHI reductions were 3% or less during years with above-average smoke coverage and typically 1% or less in areas dominated by transported smoke. By examining 16 years of smoke and irradiance data, we find that daily regional clear-sky GHI remains relatively stable, decreasing < 3% with increasing smoke coverage, consistent with our analysis of 2020 and 2019.

The two primary limitations of this study are the spatial and temporal resolution at which we conduct the aggregate analyses. We explore smoke-irradiance trends at the monthly level, which obscures day-to-day and hour-to-hour changes in surface irradiance due to variable smoke conditions. Understanding this variability is essential for producers given the need for accurate generation forecasts for electricity load balancing on finer time scales. Additionally, spatial variability in smoke-irradiance interactions is masked by our focus on trends at the state, regional, and national level. Finer temporal and spatial resolution would better constrain the range of smoke-irradiance conditions a location experiences. Our national and regional assessments capture the broader impacts of the spatially extensive smoke plumes produced by large western wildfires that are growing larger, more frequent, and longer in duration with climate change.

Most of the existing and planned solar installations in the U.S. use PV panels, which rely on GHI. As such, understanding how smoke affects surface-level GHI is crucial for locating PV development and accurately forecasting PV production. We show that smoke is associated with

large reductions in GHI close to major wildfires but minimal to no loss of GHI from transported smoke across most of CONUS. Even during extreme wildfire seasons with heavy smoke, as seen in 2020, we project little change in average PV resource availability, except in areas with optically thick, fresh, local smoke plumes. Overall, the anticipated increases in AOD from smoke emissions due to climate-induced increases in wildfire activity will minimally impact the long-term baseline solar PV resources across most of the country.

3.5 Data Availability Statement

All data used for this study are publicly available. Modeled irradiance data from the NREL NSRDB (https://nsrdb.nrel.gov/) are available for bulk download via AWS at https://registry.opendata.aws/nrel-pds-nsrdb/. Smoke plume locations are available from the NOAA NESDIS HMS smoke product, which can be downloaded at https://www.ospo.noaa.gov/Products/land/hms.html#maps. NASA's MAIAC aerosol product (MCD19A2 MODIS/Terra + Aqua land aerosol optical depth daily L2G Global 1km SIN Grid V006) can be accessed at https://lpdaac.usgs.gov/products/mcd19a2v006/ and the CERES cloud data product (SYN1deg-1Hour Edition 4.1) can be accessed at https://ceres-tool.larc.nasa.gov/ord-tool/jsp/SYN1degEd41Selection.jsp.

CHAPTER 4

OBSERVED AND MODELED CHANGES IN BOUNDARY LAYER AND SURFACE-LEVEL ACTINIC FLUX DUE TO WILDFIRE SMOKE PLUMES IN THE CALIFORNIA CENTRAL VALLEY IN SUMMER 2018 (WE-CAN)[4]

4.1 INTRODUCTION

Recent severe wildfire seasons in the western U.S. and Canada have highlighted the increasing impact of wildfire smoke on surface air quality across North America. Smoke impacts surface air quality via multiple processes including direct emission of fine particulate matter and gas-phase pollutants into the boundary layer (McClure & Jaffe, 2018; O'Dell et al., 2020, 2021) as well as changing the chemical composition in ways that promote ozone and secondary pollutant formation. Beyond introducing chemical species, smoke affects visibility (Jaffe et al., 2020; R. J. Park et al., 2003; Val Martin et al., 2015) and the amount and characteristics of light reaching the surface (Corwin et al., 2022b; McKendry et al., 2019). By absorbing and scattering incoming shortwave radiation, smoke alters chemical reactions that control pollutant concentrations.

Photochemical reactions occur when a photon of light is absorbed and a molecule dissociates in a process called photolysis. The photolysis rate, J, is calculated via

$$J = \int F(\lambda)\sigma(\lambda)\varphi(\lambda)\, d\lambda$$

where F is the actinic flux in photons cm^{-2} nm^{-1} s^{-1}, σ is the absorption cross-section in cm^2 $molec^{-1}$, and φ is the quantum yield in molec $photons^{-1}$. All three components vary by

[4] Adapted from a manuscript in preparation: Corwin, K. A., Hall, S. R., Ullmann, K., Corr, C. A., & Fischer, E. V. (in prep). Observed and modeled changes in boundary layer and surface-level actinic flux due to wildfire smoke plumes in the California Central Valley in summer 2018 (WE-CAN). *Journal of Geophysical Research: Atmospheres*.

wavelength. The actinic flux, absorption cross-section, and quantum yield provide measures of the likelihood of a photon colliding with a molecule, being absorbed by the molecule, and having enough energy to break apart the molecule, respectively (Madronich & Flocke, 1999). More specifically, actinic flux refers to the flux of photons through a point in the atmosphere from all directions at a given time. Actinic flux is measured directly in the atmosphere and varies extensively with changes in optical conditions (e.g., clouds, aerosols, surface albedo). Quantum yield and absorption cross-section differ across chemical species, temperature, pressure, and humidity and are typically measured in laboratory settings.

Actinic flux changes as photons pass through the atmospheric column and are absorbed or scattered by gasses, aerosols, and cloud droplets. Such interactions vary by wavelength according to the absorption spectra of different species and scattering regimes (e.g., Rayleigh, Mie). The absorption of shortwave radiation by stratospheric ozone, in particular, strongly influences actinic flux at shorter wavelengths (< 330 nm) in the troposphere (Madronich & Flocke, 1999). The influence of clouds on actinic flux can be mixed, depending on the cloud position and optical depth. Low clouds have been shown to shade and reduce actinic flux near the surface while brightening and increasing actinic flux in the mid-troposphere and, to a lesser extent, the upper troposphere (Hall et al., 2018). Photolysis frequencies also have been shown to decrease (Lill et al., 2022) and NO_2 lifetimes to increase (Lindaas et al., 2017) under elevated aerosol loads during wildfire smoke events, which is indicative of smoke-driven reductions in actinic flux. Smoke emissions preferentially impact atmospheric optical properties at shorter wavelengths with impacts that vary by fire regime and smoke photochemical age (Chakrabarty et al., 2023; Corr et al., 2012; He & Carmichael, 1999; Y. H. Park et al., 2020). The actinic flux at shorter wavelengths is important for the formation and destruction of many pollutants. For

example, the ozone cycle relies on shortwave radiation for O_3 (< 340 nm) and NO_2 (< 420 nm) photolysis.

While the number of observational studies of wildfire smoke composition and evolution are increasing, chemical transport models remain a cornerstone of how we understand how wildfire smoke may affect local and downwind air quality. However, chemical transport models often rely on simplified mechanisms that apply a single photolysis rate in the boundary layer (Hall et al., 2018). Wildfire smoke's influence on photolysis rates, via changes in actinic flux, and the inclusion of such effects in chemical transport models remains understudied. Yet, accounting for smoke in determining and applying photolysis rates is especially important given smoke's preferential absorption at short wavelengths and the potentially rapidly changing optical properties and conditions in and around smoke plumes.

In this study, we leverage aircraft and satellite-based measurements to estimate smoke-driven changes in downwelling actinic flux (F↓) based on observed and modeled fluxes throughout the boundary layer and at the surface during a heavy smoke event. We use the National Center for Atmospheric Research (NCAR) Tropospheric and Ultraviolet (TUV) Radiation Model to calculate F↓ under smoke-impacted conditions based on smoke optical properties observed during a research flight from the 2018 Western wildfire Experiment for Cloud chemistry, Aerosol absorption, and Nitrogen (WE-CAN) campaign. For comparison, we calculate smoke-free conditions using TUV based on aerosol climatology and TUV default values. Direct observations of actinic flux from the onboard High Performance Instrumented Airborne Platform for Environmental Research (HIAPER) Airborne Radiation Package (HARP) provides not only a validation mechanism for implementing a TUV-based methodology, but also an independent measure of the smoke-driven changes rooted in observations. We focus on a

single flight from WE-CAN through the California Central Valley. Research Flight 08 (RF08) is ideal for examining the impact of smoke on actinic flux because RF08 targeted an extensive region with wildfire smoke in the boundary layer (< 2.2 km), and the aircraft was able to sample at low altitudes within and beneath smoke plumes from multiple nearby fires. Ultimately, we aim to answer two questions: 1) to what extent does wildfire smoke change downwelling actinic flux at the peak wavelength for NO_2 photolysis (380 nm), and 2) how well does TUV characterize changes in downwelling actinic flux under smoke-impacted conditions given the limited nature of field observations?

4.2 METHODS

We integrated aircraft, satellite, and model data to analyze smoke-driven changes in F↓ within and beneath a western U.S. wildfire smoke plume to better understand potential photooxidation and air quality in smoke-impacted environments. Figure 4.1 outlines the data, model, and workflow leveraged for this study. Briefly, we modeled downwelling actinic flux at 380 nm ($F\downarrow_{380}$) and 550 nm ($F\downarrow_{550}$) under smoke-impacted and smoke-free conditions using TUV. We performed calculations at positions, times, and altitudes along a research flight through the California Central Valley from the 2018 WE-CAN aircraft campaign. We removed cloudy locations based on observations from the Geostationary Operational Environmental Satellite-16 (GOES-16). We determine where the aircraft was located relative to smoke using the National Oceanic and Atmospheric Administration (NOAA) National Environmental Satellite, Data, and Information Service (NESDIS) Hazard Mapping System (HMS) smoke plumes as well as the WE-CAN in situ chemical composition and onboard LiDAR measurements. For smoke-impacted model calculations, we used aerosol optical properties from WE-CAN and the Multi-Angle Implementation of Atmospheric Correction (MAIAC) satellite retrieval algorithm. The strength

of modeled results was tested against direct measurements of downwelling actinic flux taken onboard the aircraft. Smoke-driven changes in F↓ were calculated at the aircraft altitude and ground using the difference between smoke-free and smoke-impacted conditions.

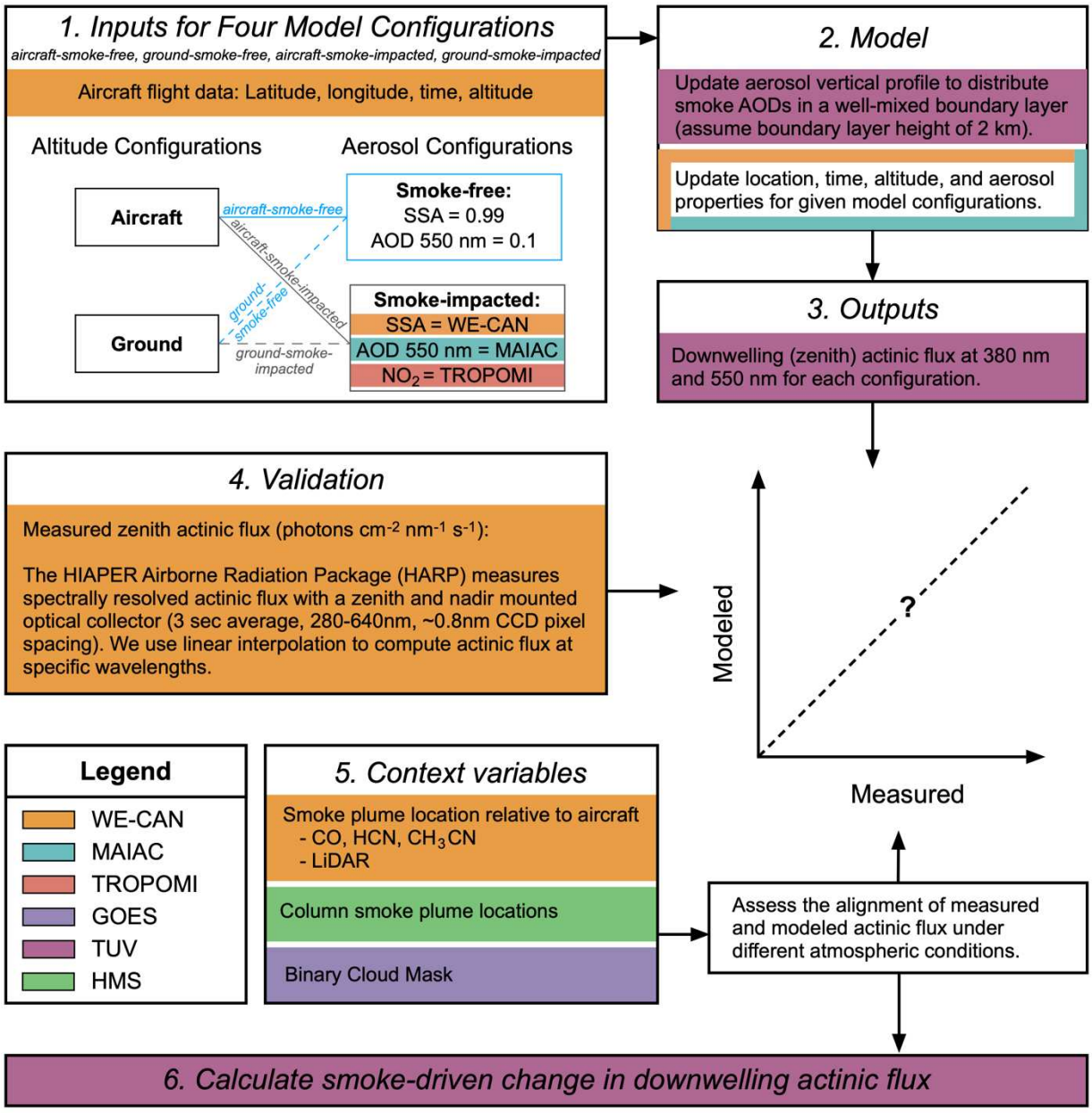

Figure 4.1: Diagram of the methods workflow with colors linking the underlying data or tool to the corresponding process.

4.2.1 Dataset Description and Model Inputs

4.2.1.1 WE-CAN

The 2018 WE-CAN aircraft-based field campaign used the National Science Foundation/National Center for Atmospheric Research (NSF/NCAR) C-130 to sample a diverse set of western U.S. wildfire smoke plumes. Based out of Boise, ID, 16 research flights occurred from July 24 through August 28, 2018, and three additional educational flights took place from September 6-13, 2018, with the aircraft based in Broomfield, CO. Sampling targeted relatively fresh smoke emissions via a pseudo-Lagrangian approach that attempted to resample the same air parcel across time and document plume evolution. Additionally, WE-CAN frequently sampled more aged smoke of mixed origin during transit to and from targeted fires due to the abundance of wildfire smoke during summer 2018. WE-CAN flew an extensive instrument payload aimed at characterizing the aerosol, chemical, and cloud composition as well as the shortwave radiation field. Detailed descriptions of the campaign, sampling strategies, and instruments are available in O'Dell et al. (2020), Juncosa Calahorrano et al. (2021), and Lindaas et al. (2021). In this study, we primarily relied on the following data and instruments from the WE-CAN payload for model input and contextual variables:

- Flight metadata (latitude, longitude, time, aircraft altitude, and ground altitude).
- Spectrally resolved actinic flux measurements from HARP.
- Carbon monoxide (CO) concentration from the Aerodyne Research CS-108 quantum cascade laser (QCL) mini-TILDAS tunable diode laser infrared absorption spectrometer (Lebegue et al., 2016).

- Hydrogen cyanide (HCN) and acetonitrile (CH_3CN) concentrations from the NCAR Trace Organic Gas Analyzer (TOGA)–a fast online gas chromatograph-mass spectrometer (GS-MS) (Apel et al., 2003, 2015; Permar et al., 2021).
- Aerosol absorption (ABS) at 405 nm and 660 nm from the Photoacoustic Absorption Spectrometer (PAS) (Shen et al., 2024).
- Aerosol scattering (SCAT) and overall extinction (EXT) at 450 nm and 660 nm from the Cavity Attenuated Phase-Shift Spectrometers (CAPS) (Shen et al., 2024).
- Upward and downward lidar profiles from the University of Wyoming Cloud Lidar (WCL) at 355 nm (WCL-I) and 351 nm (WCL-II).

Measurements of F↓ from the HARP instrument formed the foundation of this study, allowing us to determine how well TUV recreates field conditions. Alignment between TUV and HARP was necessary to ensure reasonable calculations of smoke-driven changes in actinic flux, particularly at the ground. HAPR measures spectrally resolved actinic flux from 280-640 nm using zenith and nadir mounted optical collectors with ~0.8 nm CCD pixel spacing. Measurements are reported at three-second averaged intervals to which we aligned all other WE-CAN and satellite variables. HARP measures flux at 462 wavelengths but not at the exact wavelengths used in this study (380 and 550 nm). As such, we used linear interpolation between adjacent, closely spaced wavelengths to compute actinic flux at the wavelengths of interest. We focused our analysis on F↓ as measured by the zenith instrument to remove the complexities of rapidly changing surface albedo and cloud conditions beneath the aircraft (Section 4.2.1.4). Finally, the HARP instrument error is ± 2-3% for solar zenith angles from 0-80 degrees, which applies to all WE-CAN samples considered in this study.

4.2.1.2 Locating smoke plumes

We performed actinic flux calculations at smoke-impacted locations along the flight track and excluded locations deemed smoke-free. We identified smoke-impacted locations using HMS satellite observations, WE-CAN chemical composition, and WE-CAN lidar. As noted in earlier chapters, the HMS (https://www.ospo.noaa.gov/Products/land/hms.html) is a daily operational product that provides the location of smoke plumes across North America (Rolph et al., 2009; Ruminski et al., 2006). A valid timeframe is assigned to each plume mapped, which is based on the satellite observation time. For each location along the flight path, we determined whether an overlapping smoke plume tagged to the same timeframe existed, and if so, classified the location as smoke-impacted. An HMS-derived smoke flag only indicates the presence of smoke in the atmospheric column at a given time and location but provides no indication of the vertical position of the plume relative to the aircraft.

Some known limitations of the HMS include the omission of small smoke plumes and difficulties delineating plume edges, particularly when plumes are dilute or mixed with anthropogenic haze. We note where these limitations may impact smoke identification along flights. However, the WE-CAN flight strategy targeted sampling of large plumes with steep gradients which are more easily identified and delineated during the HMS production. Plumes sampled during flight transits were also generally large, laterally extensive plumes clearly visible on satellite imagery. The exact plume edge on these aged plumes represents a conservative estimate of smoke extent. Additionally, smoke-haze mixtures pose the greatest challenge in the southeast, which is outside the focus of this study.

In addition to the HMS plumes, we used onboard chemical composition measurements of CO, HCN and CH_3CN to identify when the aircraft was sampling smoke-impacted air.

Specifically, a sample was categorized as smoke-impacted when CO > 85 ppb, HCN > 275 ppt, and CH_3CN > 200 ppt (O'Dell et al., 2020). The WE-CAN-derived smoke flags indicated the presence of smoke in the column as well as the aircraft's position within the smoke plume at the given location and time. At locations along the flight path where the chemical composition indicated smoke but the HMS indicated smoke-free conditions, we considered the location smoke-impacted.

Finally, we used lidar measurements from the WCL for additional context as to the vertical position of the aircraft relative to the smoke plumes. Level 1 processed data are available with parallel and perpendicular backscatter values as well as the depolarization ratio for nadir and zenith views. The WCL was exclusively used for aircraft navigation during WE-CAN and not optimized for research purposes. As such, quantitatively and programmatically identifying and extracting smoke plumes was outside the scope of this study as exact backscatter thresholds can vary substantially across plume and atmospheric conditions. However, visual inspection of the aerosol backscatter recorded by the lidar provided a means of determining when the aircraft was above, within, or below a smoke plume. We focused primarily on locations where the smoke was at or above the aircraft to capture the change in F↓ resulting from the smoke.

4.2.1.3 Aerosol properties from MAIAC and WE-CAN

We relied on TUV's aerosol optical property inputs, including the aerosol optical depth (AOD), single scattering albedo (SSA), and Angstrom exponent (α), to calculate actinic flux under smoke-impacted conditions. For AOD, we relied on data from the MAIAC algorithm, described by Lyapustin and Wang (2018b) and Lyapustin et al. (2018), which retrieves aerosol properties over land from measurements taken by the Moderate Resolution Imaging Spectroradiometer (MODIS) instrument aboard polar orbiting satellites. The Version 6.1

MAIAC Daily Atmosphere (MCD19A2) product includes optical depths at 470 nm and 550 nm from both the Terra and Aqua satellites to provide morning (~10:30 a.m. local time) and afternoon (~1:30 p.m. local time) observations at a 1-km spatial resolution. We focused on retrievals of AOD at 550 nm from the Aqua satellite's early afternoon overpass when available and used the Terra retrieval when necessary. Since wildfire activity is greatest in the late afternoon to early evening, which was when WE-CAN completed the bulk of their research flights, the afternoon retrievals likely better align with WE-CAN sampling conditions than the morning retrievals. However, the diurnal smoke production cycle and temporal offset between the satellite overpasses and WE-CAN flights means that the retrieved AODs used in this study likely underestimate the AOD experienced during the flight, particularly later in the day.

Although large time offsets are possible, we used the MAIAC AOD given the algorithm's focus on retrievals under smoke conditions. MAIAC employs a smoke detection test that leverages the preferential increase in absorption at shorter wavelengths (0.412 μm) due to smoke's organic carbon content. MAIAC compares observed to expected reflectance at 0.412 μm given reflectance ratios at 0.646 μm and 0.466 μm. Typically, aerosol retrieval algorithms will only retrieve AODs in areas without clouds. However, if smoke is detected, MAIAC will perform an AOD retrieval in locations marked as clear and possibly cloudy, only omitting confirmed cloudy locations. This increases the likelihood of AOD retrieval, particularly in areas with dense smoke plumes that may be confused for clouds. Recent updates to the MAIAC algorithm also dynamically increase the AOD in areas with optically thick smoke to account for the increase in absorbing organic carbon (Lyapustin & Wang, 2022).

We defined the SSA and α inputs using the WE-CAN PAS and CAPS measurements of aerosol absorption (ABS; 405 nm and 660 nm), scattering (SCAT; 450 nm and 660 nm), and

overall extinction (EXT; 450 nm and 660 nm). Details on the PAS and CAPS measurements of WE-CAN plumes are available in Shen et al. (2024). Given our interest in shorter wavelengths (380-420 nm), we computed SSA at 450 nm, rather than 660 nm, via the two following equations:

$$\text{(A) } SSA = \frac{SCAT_{450}}{EXT_{450}}$$

$$\text{(B) } SSA = \frac{EXT_{450} - ABS_{405}}{EXT_{450}}$$

Since measured scattering, absorption, and extinction values may result in unrealistic SSAs, we used a two-tiered approach to SSA calculation. We used the SSAs computed with equation A for the model input if SSAs fell within a valid range of 0-1. When SSAs from equation A were outside the valid range, we used the result from equation B as the SSA model input. If the SSAs calculated by both equations were negative or exceeded one, we excluded the point. We also only computed SSAs for samples with positive scattering or absorption values as well as positive or nonzero extinction values.

We computed α using two approaches that leveraged the CAPS and MAIAC measurements. Angstrom α can be calculated as a ratio of extinction or optical depth to the ratio of the wavelengths via

$$\alpha = -\frac{log(\frac{\beta^{ext}_{\lambda 1}}{\beta^{ext}_{\lambda 2}})}{log(\frac{\lambda_1}{\lambda_2})} \text{ OR } \alpha = -\frac{log(\frac{\tau_1}{\tau_2})}{log(\frac{\lambda_1}{\lambda_2})}$$

where β^{ext} is the extinction coefficient, τ is the AOD, and λ is the wavelength. We calculated α along the flight path using the CAPS aerosol extinction at 450 nm (λ_1) and 660 nm (λ_2) and the MAIAC AOD at 470 nm (λ_1) and 550 nm (λ_2). Both the CAPS and MAIAC α calculations resulted in mean/median α values of approximately 2 (1.96/1.98 for MAIAC, 1.83/1.83 for CAPS), which is consistent with extinction due to fine mode aerosols such as smoke. As such,

we used an α of 2 when modeling actinic flux at 380 nm. An α of zero was used when modeling actinic flux at 550 nm since we provided AOD at 550 nm and no scaling was needed.

4.2.1.4 Tropospheric NO_2

Since we are interested in wavelengths relevant for NO_2 photolysis, the concentration of NO_2 in the atmospheric column above any point affects F↓ at 380 nm below. Additionally, wildfire smoke includes substantial quantities of NO_2. We used the tropospheric NO_2 vertical column retrieved by the TROPOspheric Monitoring Instrument (TROPOMI) aboard the Sentinel-5P satellite (~1:30 p.m. local time) to approximate the NO_2 contribution from the plume. We applied a quality assurance value of > 0.75 to remove clouds and ensure the use of high-quality column number densities. Per TUV defaults, the NO_2 was distributed throughout the lower 1 km of the atmospheric profile, which is consistent with near-surface smoke emissions.

4.2.1.4 Locating clouds

Clouds can drive significant changes in actinic flux and pose challenges for aligning the TUV modeled values with the HARP measurements. Since we are interested in smoke-driven changes in actinic flux, we took multiple steps to remove cloud effects from our analysis. We used the GOES-16 level 2 binary cloud mask (L2-ACMC), which indicates whether a pixel is cloudy/possibly cloudy or clear/possibly clear at a 1-km horizontal and 5-minute temporal resolution (NOAA, 2022), to locate clouds along the flight path. We collocated the GOES and WE-CAN flight observations using a nearest-neighbor approach and extracted the cloud mask corresponding to the nearest time for each flight sample. Since the GOES resolution averages a larger area than a flight sample, we may have removed locations where clouds do not directly overlap with the flight path or retained locations where GOES failed to detect small clouds. We excluded all flight locations identified as cloudy to remove as much influence of clouds as

possible. To further avoid cloud effects, we focused solely on downwelling rather than upwelling or total actinic flux to avoid cases where small clouds were present beneath the aircraft. Using the zenith direction also has the benefit of minimizing the impact of surface albedo, which can change rapidly and pose another challenge for isolating smoke-driven flux changes.

4.2.2 Modeling Downwelling Actinic Flux

4.2.2.1 TUV Radiation Model Configurations and Output

We used TUV Version 5.4 (Madronich & Flocke, 1999) to model F↓ under four different model configurations that vary altitude and aerosol conditions (Figure 4.1):

1. At the aircraft altitude given measured WE-CAN aerosol conditions (aircraft-smoke-impacted)
2. At the aircraft altitude under smoke-free conditions (aircraft-smoke-free)
3. At the ground altitude beneath the aircraft given measured WE-CAN aerosol conditions (ground-smoke-impacted)
4. At the ground altitude beneath the aircraft under smoke-free conditions (ground-smoke-free)

We used an AOD at 550 nm of 0.1 for the smoke-free aerosol conditions alongside TUV default values for SSA (0.99), α (1), and scattering asymmetry factor (*g*; 0.61). These configurations allowed for the estimation of smoke-driven changes (smoke-free vs. smoke-impacted) in F↓ at two altitudes. For each configuration, we calculated actinic flux at two wavelengths: 380 nm and 550 nm. The former wavelength is important for NO_x photochemical reactions and the latter for process validation given the use of the MAIAC AOD at 550 nm as a primary model input. As such, we expect the greatest agreement between the F↓ modeled by TUV and measured by HARP at 550 nm and poorer agreement at shorter wavelengths given increased absorption by

black and brown carbon at shorter wavelengths. Each execution of TUV involved two steps: updating the aerosol vertical distribution in the source code (Section 4.2.2.2) and updating the model input files to import the flight and aerosol parameters (Section 4.2.2.3) for the four model configurations.

4.2.2.2 Tailoring the TUV Source Code: Smoke Aerosol Vertical Distribution

TUV computes actinic flux given stated aerosol optical properties for AOD, SSA, and Angstrom α defined in the user input. The *g* and aerosol vertical profile are defined in the source code. For the smoke-impacted cases, we used the TUV's default *g* of 0.61 for 550 nm and increase *g* to 0.69 at 380 nm, consistent with the wavelength dependency of *g* and measured *g* values for smoke (Dubovik et al., 2002; Gómez-Amo et al., 2017; Ross & Hobbs, 1998). By default, TUV distributes AOD vertically throughout the atmospheric column according to Elterman (1968), which specifies a continental aerosol vertical distribution with an AOD of 0.235. Smoke plumes, however, are not distributed according to the background aerosol distribution. Instead, the plumes are superimposed on top of the background aerosol conditions with injection height and atmospheric stability dictating the position of smoke in the atmospheric column. As such, we built additional aerosol vertical profiles that overlay aerosols from smoke on top of the background aerosols distributed according to Elterman. We distributed the smoke aerosols within the boundary layer, consistent with most plume injection heights (Val Martin et al., 2018). We approximated the planetary boundary layer height at 2.2 km based on a combination of the flight's potential temperature and CO profiles as well as MERRA-2 boundary layer heights at the northern and southern ends of the Central Valley segment. Given TUV's 1-km aerosol vertical resolution, we set the boundary layer height at 2 km and assumed a well-

mixed distribution throughout the boundary layer (i.e., 50% of the smoke AOD from 0-1 km and 50% from 1-2 km).

Figure 4.2.a outlines the workflow used to determine which aerosol vertical profile we implemented for each flight point. Ultimately, only the coefficients for the first two layers (0-2 km) were altered. We used a look-up table approach based on the rounded percent change in AOD relative to a smoke-free continental AOD at 550 nm of 0.1 (NASA, 2016; NOAA, 2005). We assumed that any point with a round AOD of 0.1 or lower followed the default Elterman profile. As noted, the Elterman profile is a distribution of an AOD of 0.235, but TUV employs this profile to distribute any AOD provided (0.1 in this case). At locations with an elevated AOD, F↓ was modeled by superimposing the smoke distribution of the additional AOD above 0.1 on top of the Elterman distribution (Elterman+Smoke). The exact Elterman+Smoke profile used depended on the magnitude of AOD increase from the smoke-free condition. To reduce computational load, we used a look-up table approach with new profiles defined for multiples of the smoke-free AOD up to the maximum RF08 observed AOD of 2.2 (i.e., a defined profile exists for points where the AOD was 2 times, 3 times, and up to 22 times the smoke-free value). The Elterman profile distributed 74% of the AOD below 3 km while the Elterman+Smoke profiles rapidly increased the distribution of AOD toward the surface (Figure 4.2.b).

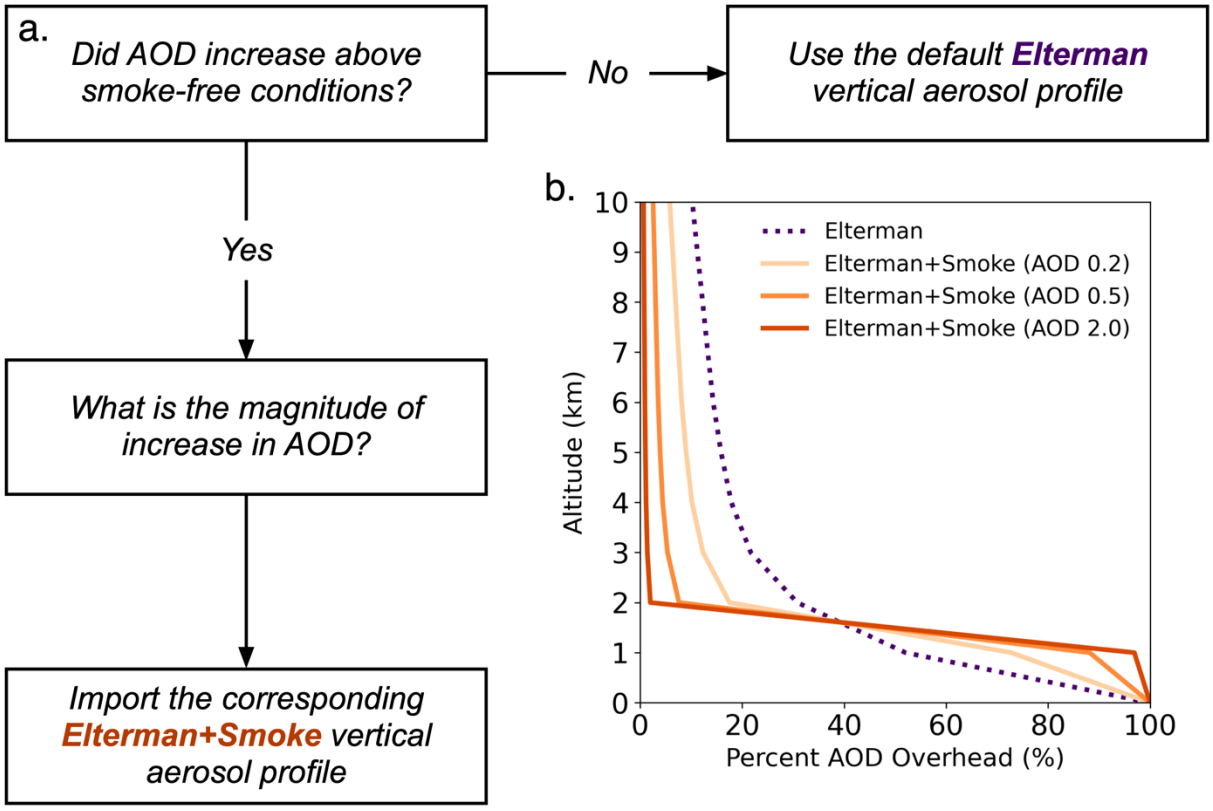

Figure 4.2: (a) Flow chart outlining which aerosol vertical profile is used for the smoke-impacted model initializations given the AOD at a location. (b) The percentage of the AOD distributed above a given altitude. The dashed line indicates the aerosol distribution according to the default TUV Elterman profile. Shaded solid lines show three examples of the Elterman+Smoke profiles for rounded AODs at 550 nm of 0.2 (light orange), 0.5 (orange), and 2.0 (dark orange).

4.2.2.3 Tailoring the TUV Input File

For each location and time modeled, after updating the aerosol vertical profile source code, we updated the following variables in the TUV user input file:

- Wavelength grid specifications: start (wstart), stop (wstop), and interval (nwint)
- Location: latitude (lat) and longitude (lon)
- Time: timezone (tmzone), start (tstart), stop (tstop), and interval (nt)
- Date: year (iyear), month (imonth), and day (iday)
- Altitude: ground (zstart), output (zout)
- Aerosol properties: AOD (tauaer), SSA (ssaaer), Angstrom α (alpha)

- Tropospheric NO_2 column (no2col)

An example file showing input values used for a single model computation is included in Figure S1 in Supporting Information S1. Since we focused on F↓, we enabled the direct downwelling (dirsun) and diffuse downwelling (difdn) components in TUV and disabled the diffuse upwelling (difup) component. All model input variables were averaged to the three-second resolution of the HARP zenith instrument's actinic flux measurements to improve alignment and ease of comparison between the TUV computations and HARP measurements.

4.2.3 Analysis of TUV Modeled Actinic Flux

We used HARP's direct measurements of zenith actinic flux to diagnose how well the F↓ modeled by TUV aligns with in situ conditions. For all points, we calculated the change in downwelling actinic flux (ΔF↓) at the aircraft altitude and the ground for each wavelength (380 nm, 550 nm) between the modeled smoke-free and smoke-impacted conditions as well as the smoke-free conditions and HARP observations. Data analysis was performed using Python 3.10.12. Although we focus on assessing ΔF↓ under smoke-impacted conditions, we also conducted initial tests of the methodology outlined herein using a segment of WE-CAN Research Flight 19 (RF19) that was cloud-free, smoke-free, and characterized by relatively low AODs (< 0.15). Results of the RF19 analysis are presented in Figures A3.1-A3.3.

4.2.4 California Central Valley Case Study

In this study, we provide a case study of ΔF↓ in the California Central Valley as observed during WE-CAN's RF08 and modeled by TUV. RF08 focused on extensive low-level sampling within and beneath a multilayered smoke plume stemming from emissions from the Carr Fire, Mendocino Complex Fires, and wildfires near Yosemite. A series of missed approaches provided vertical profiles through the boundary layer. Figure 4.3 presents a map of the flight path (Figure

4.3.a) and diagram of the flight altitude over time (Figure 4.3.c) relative to the ground, lidar data, clouds, and smoke. A photograph (Figure 4.3.b) from the aircraft is included for additional context.

RF08 took off out of Boise, ID on August 8, 2024 at 19:02 UTC (12:02 PDT) and descended into the smoke plume over the Central Valley from the north at approximately 20:35 UTC (13:35 PDT). Due to the proximity of active fires, the AOD at 550 nm (Figure 4.3.c) was highest (>1.0) in the northernmost region of the Central Valley and the initial descent time aligns closely (+~1hr) with the MAIAC AOD retrieval from Aqua. The aircraft proceeded south to areas where the AOD was lower (<1.0), and turned around south of Merced, CA at ~22:00 UTC (15:00 PDT) to return northbound along a similar transect. On both the southbound and northbound flight transects, the aircraft performed missed approaches at three airports (KCIC, KMHR, and KMER), capturing twelve vertical profiles. RF08 ascended out of the Central Valley smoke at around 23:26 UTC (16:26 PDT) between Redding and Chico, CA to return to Boise.

In total, the Central Valley portion of RF08 provided 2,684 smoke-impacted, cloud-free, complete samples for analysis. Of the 3,417 three-second observations from the Central Valley, 16% were excluded due to missing AOD or SSA values and 6% were removed due to cloud cover. Most cloudy locations occurred near the southern terminus of the flight and resulted in the exclusion of much of the data from the KMER missed approaches. All remaining 2,684 cloud-free locations were deemed smoke-impacted based on the HMS, and 25% of locations were characterized as in-plume given the onboard chemical composition measurements. On average,

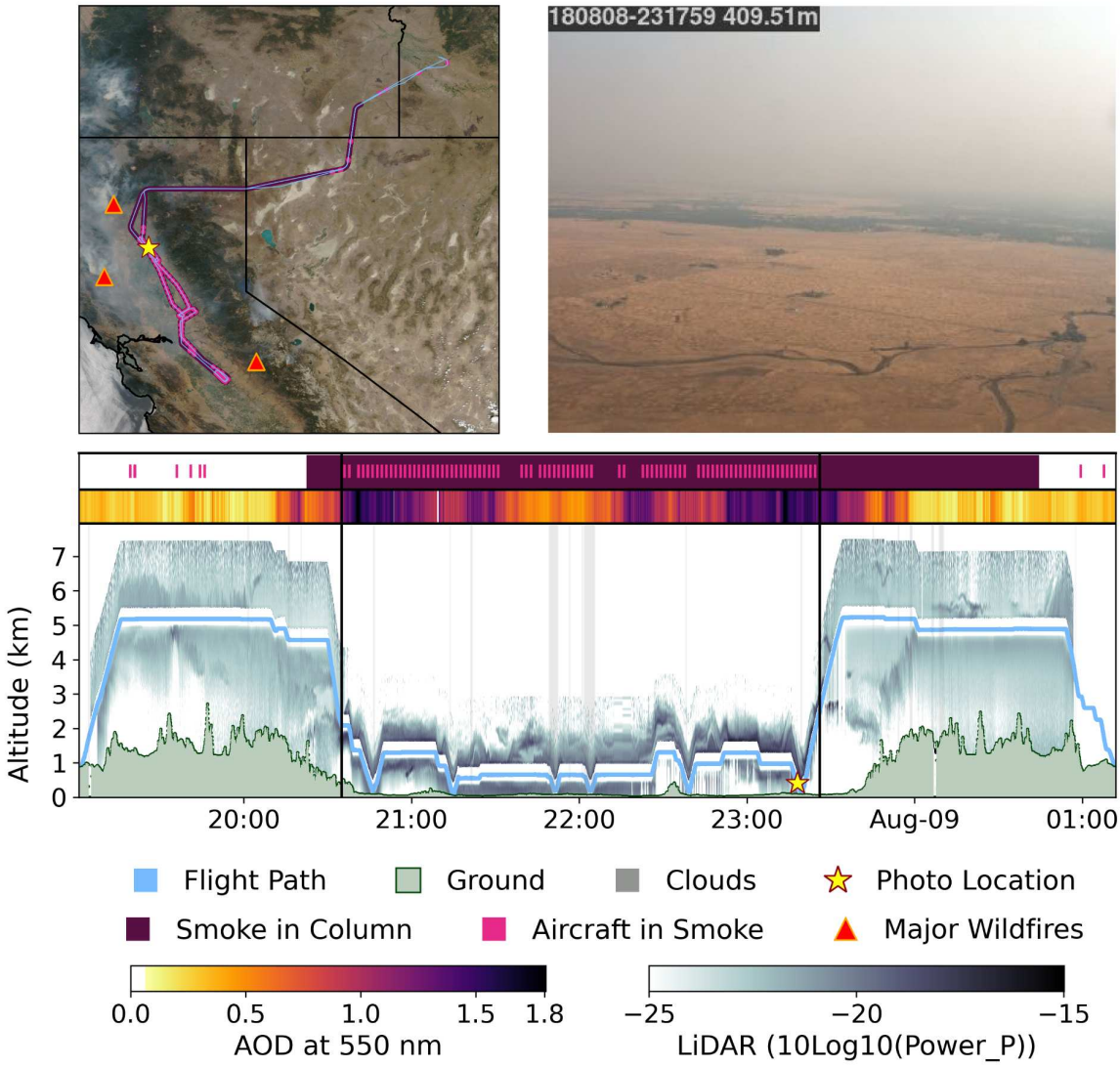

Figure 4.3: Map (a) showing the aircraft flight path (blue) for Research Flight 08 on August 8, 2018 that indicates when the aircraft was located within a smoke plume (pink) based on sampled chemical composition and when the HMS indicates smoke in the atmospheric column (brown). A photograph (b) from the front of the aircraft provides an example of the smoke conditions within the California Central Valley section of the flight. The photograph location (yellow star) is indicated on both the flight map (a) and flight path diagram (c). Diagram (c) of the aircraft (blue) and ground (green) altitude over time with clouds (gray vertical shading) and smoke indicated. Smoke is indicated along the upper bar showing smoke in the column (brown) and when the aircraft is within a plume (pink). AOD at 550 nm (range: 0.0-1.8) along the flight path is indicated in the upper bar beneath the smoke flags. Black vertical lines indicate the start and end of the California Central Valley section when the aircraft was largely located within and beneath the smoke plume, which is our focus in subsequent analyses.

the AOD along the flight path was 1.11 (median: 1.14) and ranged from 0.41-1.8 with higher AODs concentrated in the northern Central Valley. However, the high AODs in the north during the return transect likely provide a lower bound on actual AOD given the large time offset between MAIAC and WE-CAN in the late afternoon when fire activity increases.

4.3 Results and Discussion

4.3.1 Model Performance Relative to Direct Measurements

For modeling purposes, we relied on the MAIAC AOD at 550 nm to compute F↓, and as such, expect close alignment of the modeled and measured $F\downarrow_{550}$. At 550 nm, TUV does not need to scale the AOD according to an Angstrom α that can depend significantly on the aerosol composition and spectral absorption dependence. Figure 4.4 provides the ratio of TUV's modeled $F\downarrow_{550}$ and HARP's measured $F\downarrow_{550}$ along the flight path, highlighting the ratio's minimal variability around a one-to-one alignment. Overall, the modeled-to-measured ratio ranges from 0.80 to 1.15 with an average and median of 0.96, indicating a tendency for TUV to slightly underestimate HARP's measurements. The ratio is relatively stable near 1.0 along flight sections where the aircraft maintains a steady altitude, and the model is less able to reproduce observed fluxes during steep ascents and descents (i.e., missed approaches). Additionally, although infrequent during this flight, clouds can shade or brighten cloud-free observations even when observations are tens of kilometers away (Hall et al., 2018). Cloud brightening from increased scattering in the direction of the aircraft would result in higher measured $F\downarrow_{550}$ than TUV computes.

Figure 4.5b and d presents a more detailed comparison of the modeled and measured $F\downarrow_{550}$ and indicates that the TUV smoke-impacted configuration improves characterization of observed fluxes relative to the TUV smoke-free configuration. HARP measured a wide range of

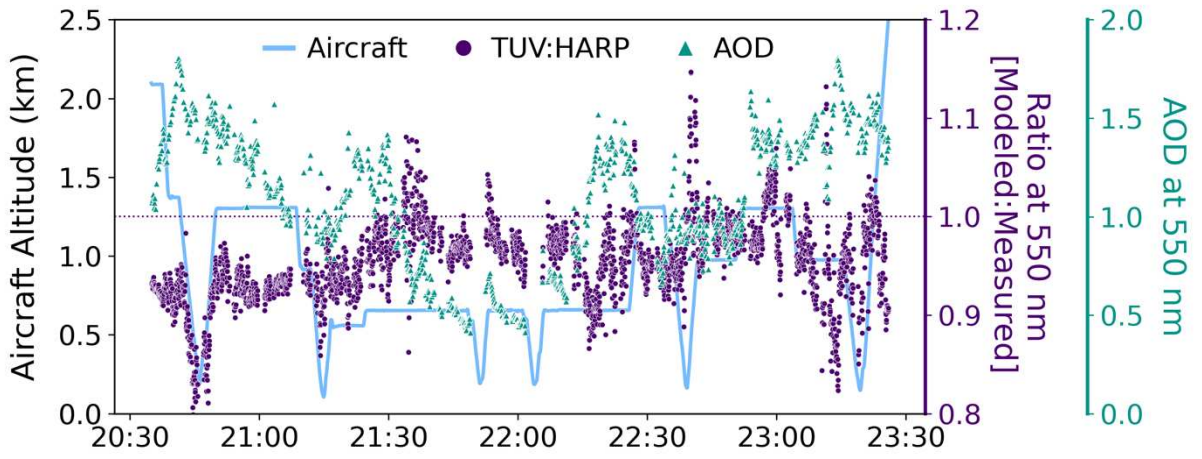

Figure 4.4: The purple points show the ratio of the TUV modeled to HARP measured downwelling actinic flux at 550 nm ($F\downarrow_{550}$) for all smoke-impacted and cloud-free locations as modeled by the aircraft-smoke-impacted model configuration.

fluxes throughout the Central Valley ranging from 3.97×10^{14} to 6.21×10^{14} photons cm^{-2} nm^{-1} s^{-1} and averaging 5.63×10^{14} photons cm^{-2} nm^{-1} s^{-1} (median: 5.73×10^{14} photons cm^{-2} nm^{-1} s^{-1}). $F\downarrow_{550}$ was smaller later in the flight as solar zenith angles increased with a noted decline at lower altitudes during the final missed approach near Chico, CA when smoke emissions and the AOD time offset were greatest. Under the smoke-free conditions, $F\downarrow_{550}$ values were narrowly constrained between 5.19×10^{14} and 5.53×10^{14} photons cm^{-2} nm^{-1} s^{-1} with an average of 5.40×10^{14} photons cm^{-2} nm^{-1} s^{-1} and median of 5.41×10^{14} photons cm^{-2} nm^{-1} s^{-1}. The smoke-free configuration failed to characterize the full range of observed $F\downarrow_{550}$, particularly when $F\downarrow_{550}$ was low ($< 5.19 \times 10^{14}$ photons cm^{-2} nm^{-1} s^{-1}). However, including smoke-specific inputs improved TUV's ability to recreate observed conditions. Under the smoke-impacted configuration, the modeled $F\downarrow_{550}$ variability increased to range from 3.57×10^{14} to 6.22×10^{14} photons cm^{-2} nm^{-1} s^{-1}, which more closely aligned with HARP's measurements. The average smoke-impacted $F\downarrow_{550}$ (5.38×10^{14} photons cm^{-2} nm^{-1} s^{-1}) was similar to that of the smoke-free condition while the median (5.50×10^{14} photons cm^{-2} nm^{-1} s^{-1}) exceeded the smoke-free median but was below the observed median. Fluxes computed via the smoke-impacted configuration align well with the

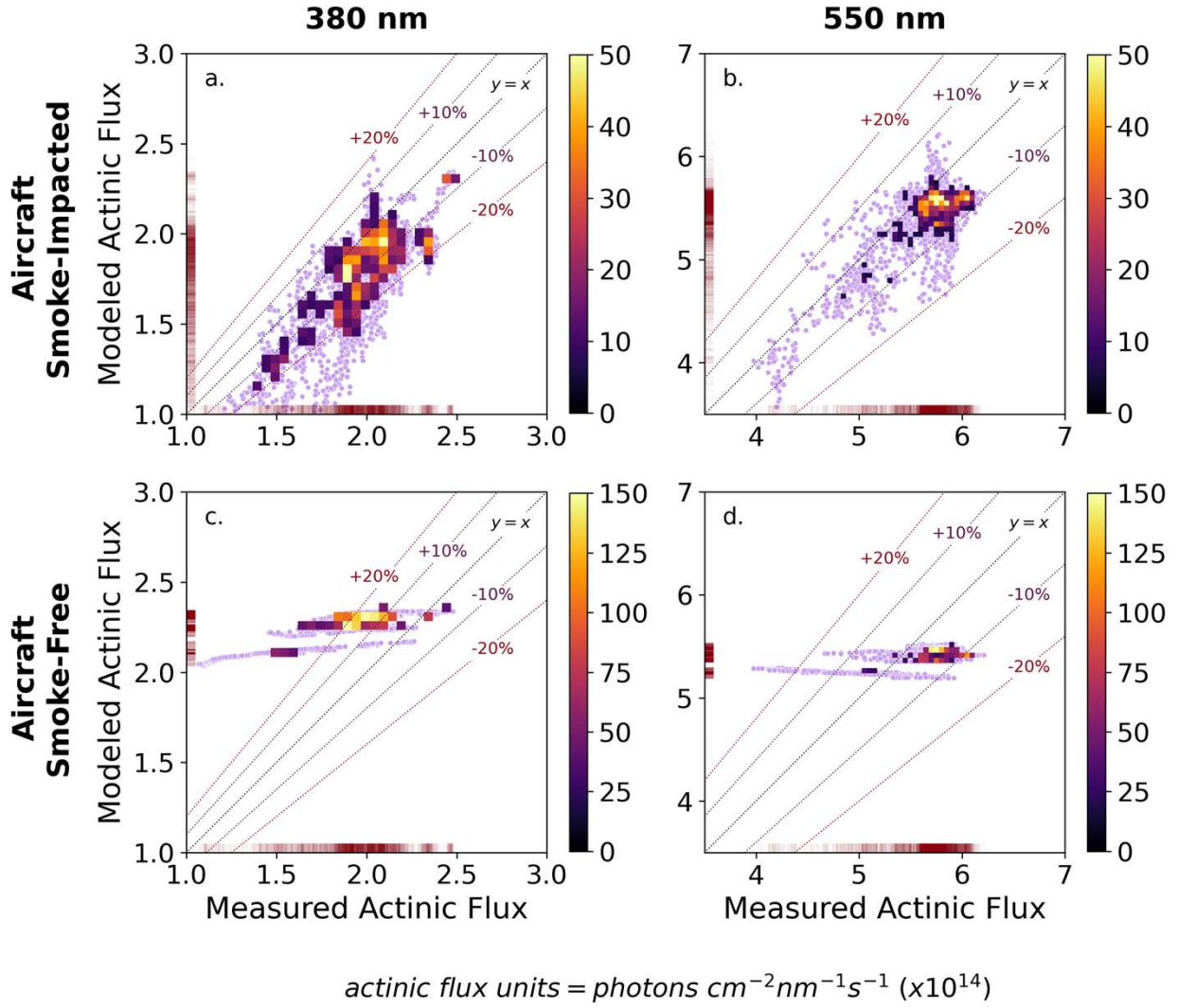

Figure 4.5: Comparison of TUV modeled and HARP measured F↓ (photons cm^{-2} nm^{-1} s^{-1}) for the aircraft-smoke-impacted (a, b) and aircraft-smoke-free (c, d) model configurations at 380 nm (a, c) and 550 nm (b, d). Only cloud-free, smoke-impacted locations along the California Central Valley section of RF08 are included (see black vertical lines Figure 4.3 for location bounds). Individual points are shown (purple) with an overlapping histogram heat map that indicates the point concentration in each plot position (colorbar). Rugplots (red) along the x and y axes display the distribution of measured and modeled values, respectively.

HARP measurements. Given the HARP error of ± 2-3%, 32% of TUV fluxes at 550 nm are not distinguishable from measured values (i.e., modeled values are within 3% of measurements). Additionally, 100%, 93%, and 55% of modeled values within 20%, 10%, and 5% of the measurements, respectively. Including observed smoke conditions improved the alignment with

measurements relative to smoke-free conditions under which 98%, 88%, and 44% of modeled values were within 20%, 10%, and 5% of the measurements, respectively. Additionally, smoke-impacted fluxes at 550 nm were more closely correlated with measurements ($r = 0.80$, $p < 0.0001$) than the smoke-free fluxes ($r = 0.61$, $p < 0.0001$).

Although the smoke-impacted $F\downarrow_{550}$ values closely correlate with HARP's measurements, TUV generally underestimates $F\downarrow_{550}$. The smoke-impacted fluxes only overestimated measurements at 10% of locations with 86% of overestimations staying within 5% of measurements and 96% within 10%. No modeled values exceeded the measurements by more than 15%. Alternatively, 90% of smoke-impacted fluxes underestimated observed $F\downarrow_{550}$, with 51% underestimated by less than 5%, 93% by less than 10%, and none by more than 20%. The $F\downarrow_{550}$ from TUV is biased low but including smoke optical properties substantially improves TUV's ability to characterize $F\downarrow_{550}$ under smoke conditions.

We also computed $F\downarrow$ at 380 nm (Figure 4.5.a and c)–a more photochemically relevant wavelength near the peak of NO_2 photolysis curve. Again, the smoke-impacted model captured much of the variability in $F\downarrow_{380}$, aligned closely with measurements, and tended to be biased slightly low. $F\downarrow_{380}$ as measured by HARP ranged from 1.07×10^{14} to 2.48×10^{14} photons cm^{-2} nm^{-1} s^{-1} with an average (median) of 1.93×10^{14} (1.95×10^{14}) photons cm^{-2} nm^{-1} s^{-1}. $F\downarrow_{380}$ is lower than $F\downarrow_{550}$ due to the reduced solar irradiance at 380 nm relative to a near peak at 550 nm as well as the increased absorption at shorter wavelengths by organic carbon in smoke. The smoke-free configuration predicted a relatively narrow range of $F\downarrow_{380}$ from 2.03×10^{14} to 2.34×10^{14} photons cm^{-2} nm^{-1} s^{-1} with an average and median $F\downarrow_{380}$ of 2.26×10^{14} photons cm^{-2} nm^{-1} s^{-1}. Most of the smoke-free fluxes (93%) overestimated the measurements with 80% in excess of 10% and 38% in excess of 20% of the measurements. The Angstrom exponent (α=1) used in the smoke-free

configuration failed to account for the increased spectral absorption at shorter wavelengths by finer smoke aerosols. The smoke-free conditions poorly characterize the observed $F\downarrow_{380}$.

Accounting for smoke in the aerosol properties, the smoke-impacted configuration exhibited substantially more variability than the smoke-free configuration and more closely aligned with observations. Overall, 14% of modeled fluxes at 380 nm matched HARP measurements with HARP's error (3%). The smoke-impacted $F\downarrow_{380}$ ranged from 6.81×10^{13} to 2.42×10^{14} photons cm^{-2} nm^{-1} s^{-1} with an average (median) of 1.72×10^{14} (1.79×10^{14}) photons cm^{-2} nm^{-1} s^{-1}. As observed at 550 nm, TUV tended to underestimate $F\downarrow_{380}$ by reporting lower fluxes than were measured. Only 9% of modeled values overestimated measurements while 91% underestimated measurements. Of the overestimates, 95% exceeded the measurements by less than 10% and none exceeded measurements by more than 20%. Of the underestimates, 41% underestimated measurements by less than 10%, 83% by less than 20%, and 17% by more than 20%. Overall, TUV performs well at approximating the measured F↓ at 380 nm, particularly given the increased complexity of smoke optical properties at shorter wavelengths compared to 550 nm. TUV captures trends in F↓ resulting from smoke but overestimates smoke's impact. As such, our results are an upper bound on the change in F↓ since TUV fluxes were biased low in this case.

Figure 4.6 provides additional context around the conditions influencing the alignment between the modeled and measured fluxes. While TUV largely reproduced the HARP measurements well, some extreme outliers existed. Examining the ratio of modeled-to-measured fluxes along the flight path (Figure 4.6.a/b) showed that the ratio was closest to one when the aircraft maintained a relatively stable altitude for prolonged periods of time. Model underestimates were particularly prevalent at the start of the transect in the northern part of the

Central Valley, which was closer to the smoke source. Model alignment and slight overestimates were more common in the middle and latter half of the flight when the aircraft was further south and during the return north. Locations where TUV strongly underestimated HARP were characterized by higher AOD (Figure 4.6.c/d), lower SSA (Figure 4.6.e/f), and lower altitudes

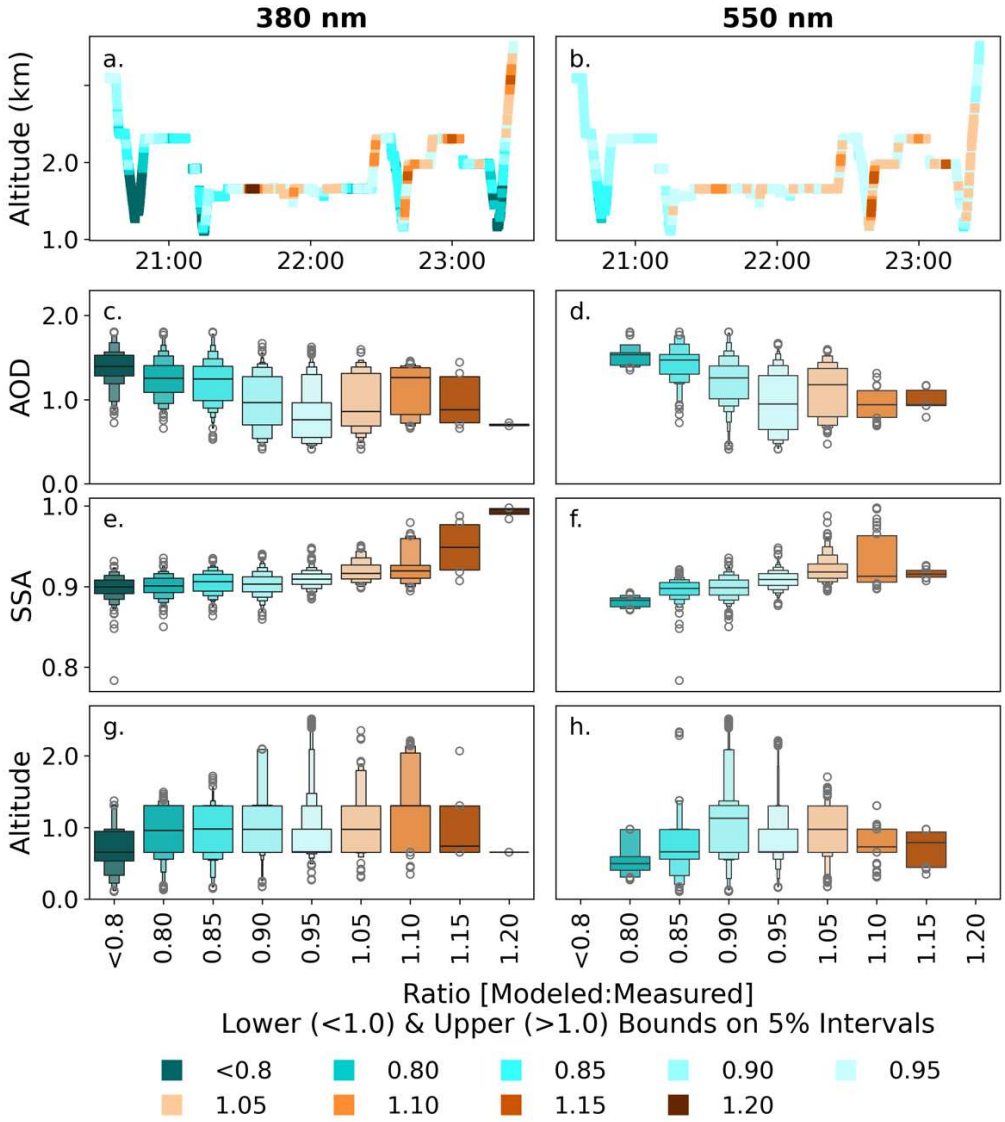

Figure 4.6: Flight paths (a, b) of the aircraft altitude over time showing the alignment of the TUV modeled and HARP measured downwelling actinic flux at 380 nm (a) and 550 nm (b). Letter-value plots (Hofmann et al., 2017) of the AOD at 550 nm (c, d), SSA (e, f), and altitude of the aircraft above sea-level (g, h) for different ratios (modeled F↓:measured F↓) showing underestimates (x: <0.8, 0.8-0.85, 0.85-0.9, 0.9-0.95, and 0.95-1.0) and overestimates (x: 1.0-1.05, 1.05-1.1, 1.1-1.15, and 1.5-1.2). Ratios are divided into bins of width 0.5 (5%) and indicated by the lower bound if an underestimate or upper bound if an overestimate. The left column (a, c, e, g) are results for 380 nm and the right column (b, d, f, h) are results for 550 nm.

Colors indicate the different ratio bins presented with cool tones indicating the model underestimated the measurements and warm tones indicating the model overestimated the measurements. Lighter shades indicate closer alignment between the model and measurements. Letter-Value plots describe a distribution via the central line indicating the median value and the upper and lower bounds indicating the first (25%) and third (75%) quantiles. Each subsequently smaller box represents additional quantiles of the remaining distribution and outliers are shown as open circles.

(Figure 4.6.g/h). On average, the model indicated that F↓ was lower than measured when the plane was flying close to the ground in optically dense (>1.4 AOD), highly absorbing (≤0.9 SSA) aerosols characteristic of fresh smoke plumes. Model performance improved as AOD decreased (0.5-1) and SSA increased slightly (≥0.91), on average. Locations where TUV overestimated HARP had similar AOD values and similar or higher SSA values compared to locations where TUV and HARP aligned; however, the model rarely overestimated the measurements. Most locations (100% at 550 nm; 85% at 380 nm) showed strong agreement (within 20%) between TUV and HARP, and examining AOD, SSA, and altitude inputs (Figure 4.6) revealed that close alignment was possible across a wide range of aerosol properties.

4.3.2 Smoke-Driven Changes in Downwelling Actinic Flux

We estimated the change in F↓ at 380 nm ($\Delta F\downarrow_{380}$; Figure 4.7) due to smoke relative to smoke-free conditions at the aircraft altitude (aircraft-smoke-impacted minus aircraft-smoke-free) and the ground (ground-smoke-impacted minus ground-smoke-free). Smoke-driven $\Delta F\downarrow_{380}$ at the ground generally exceeded the change at the aircraft altitude, except during airport missed approaches when the aircraft descended near to the ground (Figure 4.7.a). Regardless of altitude, $\Delta F\downarrow_{380}$ was smaller further south where the AOD was lower. The difference between ground and aircraft $F\downarrow_{380}$ reductions was also smaller toward the southern end of the flight. The largest separation between the magnitude of the ground and aircraft $\Delta F\downarrow_{380}$ occurred in the northern sections of the flight, particularly when the aircraft was at higher altitudes. The average percent

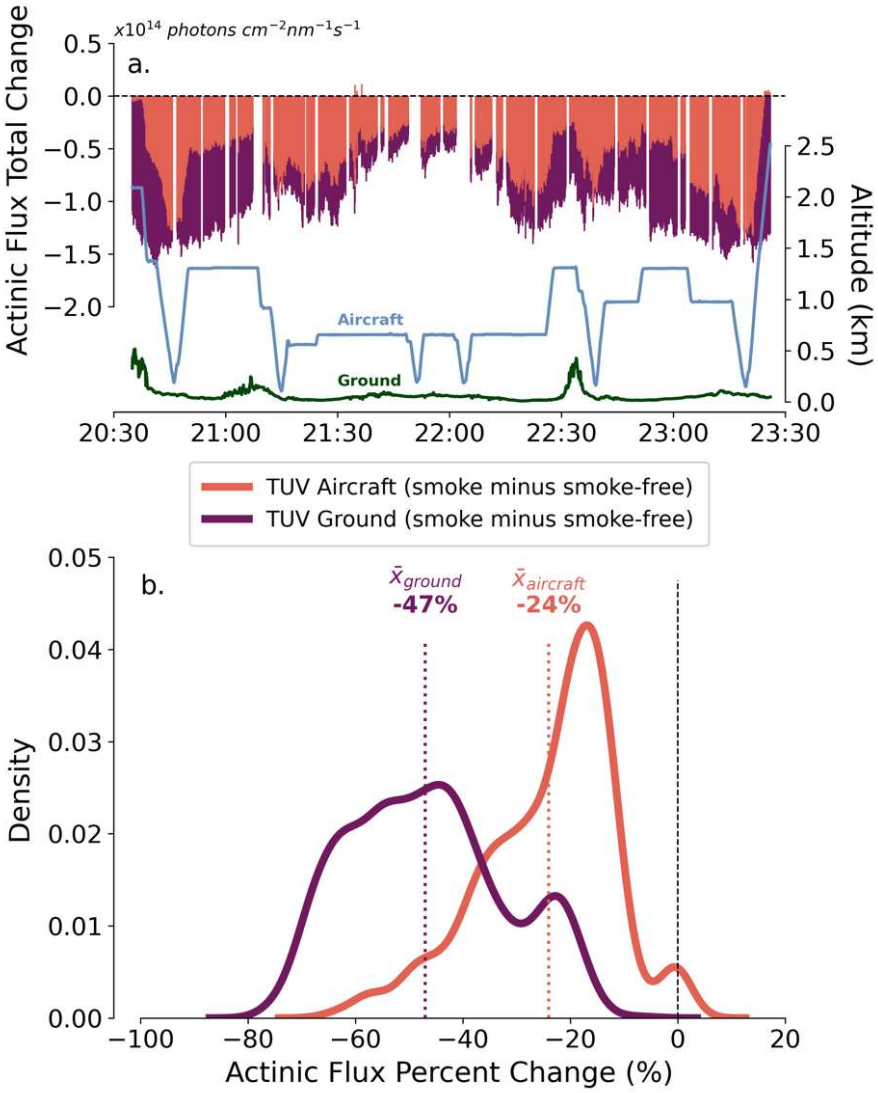

Figure 4.7: (a) Total change in $F\downarrow_{380}$ between the smoke-impacted and smoke-free TUV model calculations at the aircraft (orange) and ground (purple) altitude along the California Central Valley section of the RF08 flight path. The altitude of the aircraft (blue) and ground (green) over time provide context for where changes in actinic flux occur. (b) Kernel density estimate plot of the distribution of percent change in $F\downarrow_{380}$ at the aircraft (orange) and ground (purple) altitudes with the mean percent change indicated by vertical dashed lines of the same color, respectively. Mean $\Delta F\downarrow_{380}$ is -24% at the aircraft altitude ($\bar{x}_{\text{aircraft}}$) and -47% at the ground ($\bar{x}_{\text{ground}}$).

reduction in $F\downarrow_{380}$ given observed smoke properties was -24% at the aircraft's altitude (0.11-2.51 km) and -47% at the ground (Figure 4.7.b). At most, reductions in $F\downarrow_{380}$ reached -67% at the aircraft's altitude and -78% at the ground. Since TUV slightly underestimates $F\downarrow_{380}$ compared to observations, these percentages are likely upper bounds on the magnitude of $\Delta F\downarrow_{380}$. However, if

we increase $F\downarrow_{380}$ under the smoke-impacted configurations by 10%, average (max) losses in $F\downarrow_{380}$ due to smoke still reach -17% (-63%) at the aircraft altitude and -41% (-76%) at the ground.

Given the abundance of samples collected from altitudes 0.11-2.51 km, particularly during the six missed approaches, we constructed a vertical analysis of smoke-drive $\Delta F\downarrow_{380}$ throughout the boundary layer (< 2 km) and if the overlying 500 m (Figure 4.8). We computed the difference between the smoke-impacted and smoke-free configurations at the ground (ground-smoke-impacted minus ground-smoke-free) and at the aircraft (aircraft-smoke-impacted minus aircraft-smoke-free) at 500 m vertical intervals. We also computed $\Delta F\downarrow_{380}$ between the HARP measurements and the aircraft-smoke-free fluxes for the same 500 m intervals. The modeled percent $\Delta F\downarrow_{380}$ is greatest at the ground and decreases with increasing altitude. As noted, the decrease in $F\downarrow_{380}$ was -47% on average (-47% median) at the ground. The average (median) percent decrease is -41% (-39%) in the first 500 m, -26% (-24%) at 0.5-1 km, -19% (-18%) at 1-1.5 km, -3% (-1%) at 1.5-2 km, and +1% (+1%) at 2-2.5 km. The HARP observed vertical changes relative to the aircraft-smoke-free fluxes were lower, averaging (median) 26% (-22%) at 0-0.5 km, 17% (-15%) at 0.5-1 km, 9% (-9%) at 1-1.5 km, +1% (+5%) at 1.5-2 km, and -1% (+1%) at 2-2.5 km. The average smoke-driven percent change below 1.5 km is generally 1.5-2 times larger when computed using the TUV aircraft-smoke-impacted fluxes as compared to using the HARP observations. These disparities indicate that TUV may overestimate the decrease in $F\downarrow_{380}$ driven by smoke, especially near the ground. Developing a bias correction to better align TUV and observations could improve the overall estimates of smoke-driven $\Delta F\downarrow_{380}$ allowing for application of this method to additional areas not sampled by WE-CAN.

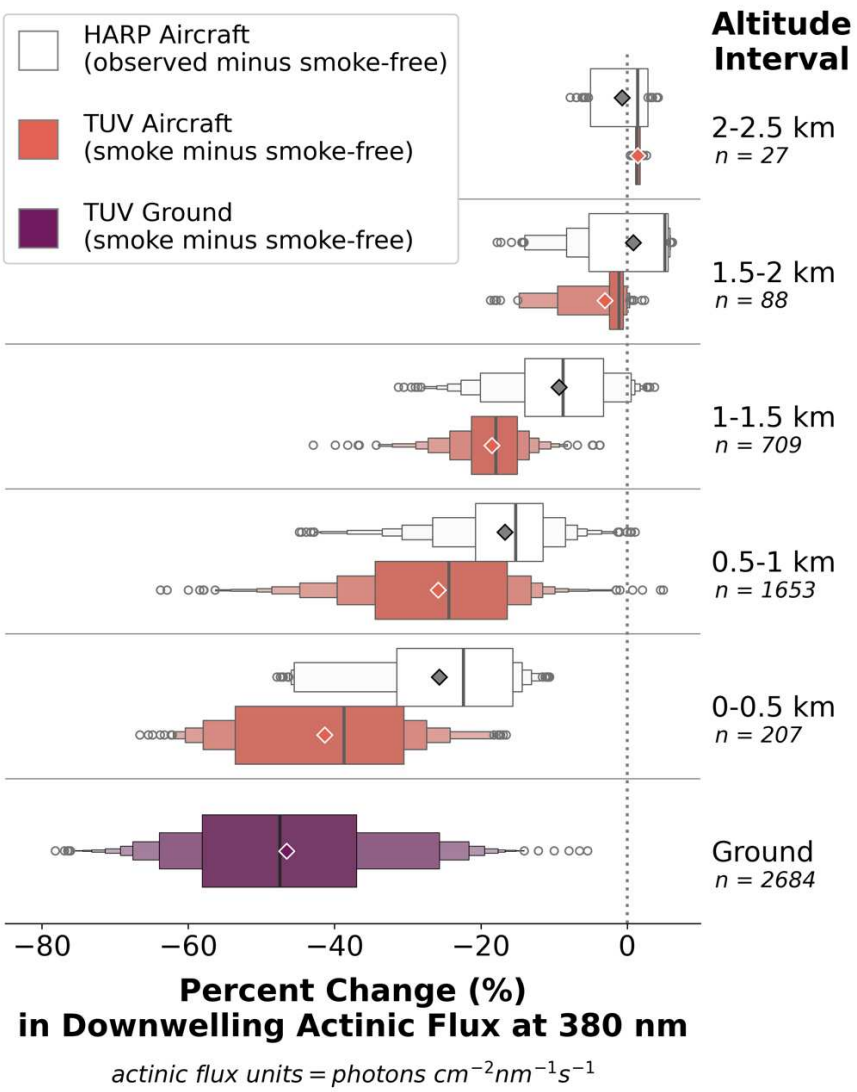

Figure 4.8: Letter-value plots showing the distribution of the percent change in $F\downarrow_{380}$ for six altitude bins. The "ground" values (purple) represent the percent change between the ground-smoke-impacted and ground-smoke-free model results to provide smoke-driven percent change at the surface. The subsequent y-values represent the percent change between 1) the aircraft-smoke-impacted and aircraft-smoke-free model results (orange) and 2) the HARP measurements and aircraft-smoke-free model results (white with grey outlines) at 0.5 km intervals. The center line indicates the median and the diamond point indicates the mean percent change. The central box represents the middle 50% of the distribution with subsequent small boxes showing the position of additional quantiles. Outliers are shown as open circles. The number of observations per box is listed along the y-axis.

4.4 Conclusions

We estimated smoke-driven changes in downwelling actinic flux throughout the boundary layer to better constrain the full impact of wildfire emissions on air quality at and near

the surface. We drew on aircraft and satellite observations to calculate downwelling actinic flux at 380 nm and 550 nm under smoke-free and smoke-impacted conditions in the California Central Valley during the WE-CAN field campaign. Relative to smoke-free conditions, we computed the change in downwelling actinic flux using HARP observations and TUV modeled fluxes under smoke-impacted conditions. We also tested a proposed method for replicating observed downwelling actinic flux using the NCAR TUV Radiation Model, which would allow for the assessment of smoke-driven changes in actinic flux at locations lacking ground or aircraft-based measurements. The key findings of this study are as follows:

1. During smoke events, downwelling actinic flux decreases at and beneath the plume at a key wavelength (380 nm) for NO_x photochemistry. Reductions are greatest at the surface and become smaller with increasing altitude through the boundary layer. Compared to modeled smoke-free conditions, WE-CAN observed a reduction of downwelling actinic flux at 380 nm in a smoke-filled boundary layer of 26%, 17%, and 9% at 0-0.5 km, 0.5-1 km, and 1-1.5 km, respectively. Minimal changes were observed above 1.5 km.
2. Using observed smoke aerosol conditions, TUV reproduces the progressively larger reductions in downwelling actinic flux near the surface, but TUV estimates are 1.5-2 times larger below 1.5 km compared to HARP observations. TUV suggests a decrease in downwelling actinic flux at 380 nm of 47% at the ground and 41%, 26%, 19%, and 3% at increasing 500-m intervals from 0-2 km. Again, minimal change is estimated above 2 km.
3. Smoke-impacted downwelling actinic fluxes computed by TUV align well with HARP's observations. At 550 nm, all modeled fluxes are within 20% of the measurements. At 380 nm, 85% of modeled fluxes are within 20% of the measurements. TUV generally underestimates the observed flux to a minor extent: the average modeled-to-measured

ratio is 0.96 for 550 nm and 0.89 for 380 nm. Smoke's stronger absorption and scattering at shorter wavelengths drive more dynamic changes in actinic flux at 380 nm than 550 nm. Even with these complexities, TUV continues to perform well at 380 nm. The persistent underestimates by TUV may stem from multiple sources of potential misalignment between modeled and observed conditions. For example, the adjusted vertical profile may lead TUV to insert more aerosols above a point than were present. Additionally, the complexities of the 3D radiation field captured by HARP observations may include additional scattered light from adjacent locations that TUV omits. TUV's largest underestimates occur near the ground under optically dense (AOD > 1.4), absorbing (SSA < 0.9) smoke, and alignment between TUV and HARP is better when AOD is lower (< 1).

Ultimately, reductions in downwelling actinic flux at 380 nm near the surface (0-0.5 km) of between 26% (HARP) and 41% (TUV) carry important implications for photochemical reactions and air quality assessments. Smoke-driven reductions in actinic flux are not currently included in many chemical transport models. Yet, taking into account smoke-driven changes in actinic flux alongside the introduction of additional VOC and nitrogen species from wildfire smoke is crucial for understanding air quality under a regime of increasing wildfire severity.

4.5 Data Availability Statement

WE-CAN data are available at https://data.eol.ucar.edu/master_lists/generated/we-can/. Smoke plume locations are available from the NOAA NESDIS HMS smoke product at https://www.ospo.noaa.gov/Products/land/hms.html#maps. NASA's MAIAC aerosol product (MCD19A2 MODIS/Terra + Aqua land aerosol optical depth daily L2G Global 1km SIN Grid V061) can be accessed at https://lpdaac.usgs.gov/products/mcd19a2v061/, GOES-16 binary

cloud mask (ABI-L2-ACMC) can be accessed at https://registry.opendata.aws/noaa-goes. The NCAR TUV Version 5.4 source code is available at https://www2.acom.ucar.edu/modeling/tuv-download. The final cleaned and merged data set used to produce the results and visualizations presented here will be available in a Dryad repository upon this article's publication in *JGR: Atmospheres*.

CHAPTER 5

SUMMARY, CONCLUSIONS, AND FUTURE WORK

5.1 SUMMARY AND CONCLUSIONS

This dissertation presents an assessment of how wildfire smoke alters incoming shortwave solar radiation at and near the Earth's surface in ways that are relevant for agriculture, energy, and air quality applications. Chapter 2 quantifies smoke-driven changes in the total amount and diffuse fraction of PAR in agricultural areas during the primary U.S. growing season. Chapter 3 contrasts the impact of local and transported wildfire smoke on DNI and GHI, important metrics for assessing solar energy potential. Chapter 4 quantifies changes in downwelling actinic flux within a smoke-filled boundary layer at the peak wavelength for NO_2 photolysis with implications for air quality. This chapter presents a summary of the main findings across these three studies and outlines the potential for future work to inform policy and management decisions within these three sectors.

In Chapter 2, I extended elements of the Brey et al. (2018) smoke climatology to include all years from 2006-2020. I highlighted the broad extent of peak smoke coverage across CONUS in the mid- to late summer as some northern Rocky Mountain and Great Plains areas experienced smoke overhead for up to 60% of August days. I demonstrated that smoke is present above major agricultural sites on one out of every five growing season days, on average, and that smoke frequency at these sites is increasing. These findings highlight the role that climate change and smoke transport patterns play in determining the prevalence of wildfire smoke both near active fires and far downwind. Regarding smoke-driven changes in PAR, I found that PAR DF increased on smoke-impacted days, primarily under conditions with minimal to no cloud cover. On clear-sky days, PAR DF increases by 50% due to smoke, meaning smoke promotes a shift

toward optimal light conditions for plants. However, smoke's impact on PAR DF became negligible as cloud cover increased. Although I observed decreases in total PAR, more work is needed to determine whether the loss of total PAR due to smoke outweighs the benefit of increased PAR DF.

In Chapter 3, I again demonstrated that key radiation metrics change with smoke but are more sensitive to changes in cloud cover. Optically thick smoke drove average changes in DNI and GHI on par with those from clouds of variable optical depths, but optically thick clouds overwhelmed the influence of smoke. Considering only clear-sky conditions, monthly mean DNI was more sensitive to the size of local, fresh, dense plumes than transported, aged, dilute plumes. Although smaller, meaningful losses in DNI also persisted into regions primarily affected by transported smoke. The projected loss of baseline DNI resources provides valuable information for citing new CSP plants or anticipating change to electricity loads, but CSP represents a relatively small percentage of U.S. solar energy production. On the other hand, while large reductions in monthly mean GHI occurred in areas close to large active wildfires, I found that transported smoke changes baseline GHI minimally (< 5%) even during an extreme wildfire season. Such results are promising for continued PV development across the U.S., but also highlight the need for increased battery storage to provide stability during local smoke events.

In Chapter 4, I estimated that, on average, smoke in the boundary layer reduced surface-level downwelling actinic flux by nearly half in this case study. The decline in actinic flux was greatest at the surface and progressively smaller with increasing altitude through the boundary layer. I found that a radiative transfer model reproduced measured downwelling actinic flux to within 20%, and largely to within 10%. The model was biased slightly low, resulting in a likely overestimate of the decline in actinic flux. However, the approach outlined provides a foundation

for expanding estimations of smoke-driven changes in actinic flux beyond the location of individual flight observations, particularly in cloud-free areas with lower AODs. Such areas include many regions affected by lofted, transported smoke.

5.2 Future Work

The following sections describe potential avenues for improvement and extension of the studies presented in this dissertation.

5.2.1 Smoke and agriculture

Chapter 2 sets a precedent for using the UVMRP data for studies of smoke-driven change in total PAR and PAR DF over agricultural regions. An initial step forward for this work would be to incorporate data from all 34 UVMRP sites to capture a wider range of smoke and irradiance conditions. This would allow us to better characterize regional differences in average values and intraregional variance, especially in the Great Plains and Midwest where understanding smoke's impact on PAR is essential for understanding smoke's impact on agriculture. One could further extend spatial coverage and allow for additional validation with collocated monitors by incorporating irradiance observations in the U.S. from the following networks: the Baseline Solar Radiation Network (BSRN), NOAA Surface Radiation Budget Monitoring (SURFRAD), NOAA Solar Radiation (SOLRAD), and DOE Atmospheric Radiation Measurement (ARM) programs. The larger volume of data would facilitate the use of regression and more sophisticated machine learning techniques to predict changes in PAR DF at the monitor sites based on cloud and aerosol conditions. Additionally, our findings demonstrate that changes in total PAR and PAR DF exhibit similar spectral patterns using ground or satellite-based AOD observations. This supports applying satellite AOD measurements as inputs to a PAR DF model to further scale this analysis to the regional and national level. Cloud

observations from CERES or the Modern-Era Retrospective analysis for Research and Applications, Version 2 (MERRA-2) would aid in the generalization of a PAR DF model to areas outside ground monitor locations.

A functional model of PAR DF throughout the growing season would create an opportunity to correlate agricultural crop productivity with the light conditions to which plants were exposed during growth. Smoke impacts could be segmented by plant functional type, plant species, timing of harvest, and timing of smoke exposure (i.e., the growth stage when most smoke exposure occurred). Examinations of changes in crop yield need to account for changes in meteorological (e.g., temperature, precipitation, relative humidity, vapor pressure deficit) and soil conditions (e.g., soil moisture content) as well as any significant changes in soil, crop, and water management practices. Model validation studies could then assess the projected crop yield changes in areas near ground monitors relative to areas far from monitors to validate greater reliance on satellite observations. I anticipate that a PAR DF model would be especially useful in relatively cloud-free areas and provide valuable insight regarding crop relocation into previously inhospitable areas (e.g., environments where the plants would have quickly reached light saturation or experienced leaf scorch). One limitation to a PAR DF and crops analysis is that many crop databases report productivity as a single measure at the end of the season. However, finer scale information on the impact of smoke at different growth stages may be less important for high-level management decisions. To avoid the challenge with sparse observations, another approach for future research could rely on the NSRDB or another nation-wide radiative transfer model to calculate PAR DF, however, there is additional value gained by relying on observational data in this analysis.

5.2.2 Smoke and solar energy

In Chapter 3, I characterized the historical influence of wildfire smoke on regional solar potential for both local and transported smoke while estimating the resulting change in PV output. I answered the questions, "how has spatial and seasonal exposure to wildfire smoke varied historically across U.S. regions of different solar resource potential?" as well as "which high potential areas are most vulnerable?" Additional lines of questioning that could be addressed in future work are as follows:

1. Given that PV panels operate more efficiently at lower temperatures, how do changes in temperature associated with wildfire smoke impact energy efficiency and PV output relative to changes in GHI?
2. Historically, where and to what degree has smoke reduced measured net generation and capacity factors at existing PV plants?
3. In the future, how will wildfire smoke change GHI and how will these changes intersect with suitable PV development areas under different fire emission scenarios? Will high and low-cost development areas be affected equally? How may net generation (MWh) change given future fire emissions?

To address Question 1, a similar analysis to that presented in Chapter 3 could compare observed surface temperatures with smoke to surface temperatures anticipated without smoke. The NOAA High Resolution Rapid Refresh-smoke model (HRRR-Smoke) provides one option for simulating smoke-impacted and smoke-free temperature conditions over CONUS. For clear-sky areas, change in surface temperature could be calculated for recent years and combined with smoke-driven changes in GHI computed in Chapter 3. Using these features as inputs to publicly available solar energy models, like the NREL System Advisor Model (SAM) or PVLIB, would

allow for the simulation of PV output given changing temperature and irradiance conditions. Simulating PV output under smoke-free conditions, smoke-impacted conditions with GHI and temperature changes, smoke-impacted conditions with GHI changes only, and smoke-impacted conditions with temperature changes only would help tease apart the direction and magnitude of smoke's impact on PV output. The ultimate impact would vary by region due to climatological differences in baseline irradiance and surface temperatures.

To address Questions 2 and 3, I outline the following detailed analysis with anticipated findings. Refining the historical impact (2006-2020) of smoke can be accomplished using publicly available data on utility-scale PV plants from the U.S. Energy Information Administration (EIA). The EIA collects monthly and annual data on solar energy capacity (Annual Electric Generator Report EIA-860) and generation (Power Plant Operations Report EIA-923) (EIA 2018). EIA-860 capacity data are available for all plants with a maximum capacity of 1 MW or greater, and panel design details (e.g., material) are provided for PV generators. Given the emerging nature of solar technologies and economies, few PV plants operated continually from 2006-2020, but combining data from multiple plants can create a longer record of changes in PV capacity and generation across the CONUS.

Co-locating individual PV plants with the HMS-MAIAC-NSRDB dataset produced in Chapter 3 would allow the calculation of smoke frequency at each plant on the monthly and annual scale of the EIA data. Net summer capacity (MW) and net generation (MWh) can then be used to calculate monthly capacity factors (CF). CFs account for changes in plant-level generation as new generators come online and old ones are retired. The EIA (2021) calculates CF using the formula

$$Capacity\ Factor = \frac{\Sigma Net\ Generation}{\Sigma Net\ Summer\ Capacity \times Available\ Time}.$$

CFs could be compared to monthly smoke frequency and AOD, and a regression model could be used to determine how CF varied at PV plants due to smoke. Such a regression model would benefit from calculating CF as a function of smoke-driven changes in irradiance and account for panel material, location, month, and year. Irradiance can be modeled for smoke-impacted and smoke-free conditions using the Spherical Harmonic Discrete Ordinate Method (SHDOM) (Evans, 1998) radiative transfer model with the correlated k-distribution from Fu and Liou (1992) and validated using the AErosol RObotic NETwork data (AERONET) (Holben et al., 1998). Smoke optical parameters, including refractive index and SSA, can vary according to Bian et al. (2020), and MAIAC AOD can provide a measure of plume thickness. Location effects can be included initially via the PV plant's balancing authority, which accounts for regional shifts in system-wide supply and demand (Hoff, 2016). Finer resolution spatial groupings could also be used to account for localized effects of severe events on power grids (e.g., heat waves).

Given the smoke optical properties in Bian et al. (2020) and findings in Chapter 3, I expect that the potential future analysis outlined in the preceding paragraphs would show larger declines in PV generation (i.e., CF) due to smoke at plants in the Western Interconnection than in the Eastern Interconnection. SSA is smaller and the imaginary component of the refractive index is larger for smoke over the West as western plumes are often optically thicker due to the proximity to large fires. The higher AOD coupled with more absorbing smoke should result in lower GHI values in the West. Chapter 3 demonstrates these larger declines in GHI around local smoke plumes. In the Eastern Interconnection, the prevalence of transported smoke is anticipated to result in smaller reductions in PV generation and CFs.

To address Question 3, one could use the GEOS-Chem and Renewable Energy Potential (reV) models to investigate how smoke-driven irradiance changes could affect potential solar

resources in the mid- and late 21st century. GEOS-Chem is a global chemical transport model (Bey et al., 2001) driven by assimilated meteorological observations from the NASA Global Modeling and Assimilation Office's (GMAO) Goddard Earth Observing System (GEOS). The model could be leveraged via a series of global full-chemistry simulations at 1° x 1° horizontal resolution with the online RRTMG radiative transfer model. To obtain present-day measures of smoke-driven irradiance changes for both high (2018, 2020, 2021) and low (2017, 2019) smoke years, one could conduct simulations for each year with and without fire emissions enabled. Fire emissions can be drawn from the Quick Fire Emissions Dataset (QFED).

Irradiance changes in the mid- and late-century could be estimated using fire emission projections for 2040-2050 and 2090-2100 from Val Martin et al. (2015) and refined by Pierce et al. (2017). These projections include landscape, agricultural, deforestation, and peat fires and account for the Representative Concentration Pathways (RCPs) (van Vuuren et al., 2011) and Shared Socioeconomic Pathways (SSPs) (O'Neill et al., 2017). RCPs and SSPs are coupled to bracket the range of air quality outcomes (Pierce et al., 2017). To calculate the percent increase in fire emissions from present for high- and low-smoke years, one could scale the 2017-2021 fire emissions to represent mid- and late-century conditions and re-run the GEOS-Chem simulations. This approach introduces fire emissions in locations and during meteorological conditions prone to burning. Results would allow the estimation of changes in surface irradiance from present-day smoke-impacted and smoke-free conditions.

To ensure policy-relevant findings, the analysis would assess the distribution of smoke exposure by PV capacity and cost, determining if smoke will impact high and low capacity/cost solar regions equally. Such an approach would benefit from grouping the analyses into different management jurisdictions. One could accomplish this using PV development projections from

the reV model, which is an open-source framework that assesses renewable energy capacity, generation, and cost across spatial and temporal domains (Maclaurin et al., 2019). The reV model accounts for resource availability from the NSRDB and uses SAM to predict generation and site-based levelized cost of energy (LCOE: revenue needed to recoup plant construction and operation costs). A spatial exclusion module identifies and excludes areas with technical, regulatory, or stakeholder restrictions that fully or partially prevent PV development. Projected capacity and LCOE are output at 90-m resolution, and supply curve estimates are reported for areas of 33.2 km^2.

Leveraging the expected reduction in CFs due to smoke (as modeled above), one could extrapolate the impact of fire emissions on future PV generation. One could scale reV's capacity (MW) output and compute net generation (MWh) under smoke-free and smoke-impacted conditions given an estimated baseline PV CF of 35% in 2050 (Ardani et al., 2021). These computations could be performed for each climate scenario and time period modeled by Val Martin et al. (2015).

Finally, beyond the three questions outlined above, further lines of research would benefit from examining how these historical and projected trends in smoke, GHI, and PV generation vary on the finer time scales that electricity markets rely on for load balancing. Electricity markets operate on the scale of minutes for selling, purchasing, and balancing electricity loads. Additionally, wildfire smoke abundance and properties change throughout the day with peak smoke production occurring in the late afternoon and early evening, which aligns with peak energy use hours (e.g., for air conditioning). Examining smoke-driven changes in GHI at an hourly, or preferably 5-minute, scale would provide more actionable information for operating PV plants and utilities. Such analyses could continue to leverage the NSRDB but make full use

of their diurnal projections. However, these studies would likely need to use geostationary satellite data rather than polar-orbiting observations. Continued advancements in smoke AOD retrievals could facilitate the use of geostationary satellite observations in lieu of MAIAC's AOD, which has limited temporal resolution.

5.2.3 Smoke and integrated food-energy systems

In addition to finding locations with suitable GHI levels, another challenge facing PV expansion is land acquisition. Up to 10% of suitable disturbed lands in the CONUS are needed to meet U.S. solar energy goals by 2050 (Ardani et al., 2021). Novel configurations like agrivoltaic systems—the collocation of solar energy and agricultural production—seek to address the demand for land. Given current and new technology, most states could receive 100% of their electricity from local solar energy by converting less than 10% of agricultural land to agrivoltaics (Miskin et al., 2019). The feasibility of agrivoltaics rests on the reduction of surface degradation by PV panels and the enhancement of PV and crop output. PV panels shade crops and create microclimate and moisture conditions beneficial to crop growth, particularly in dryland agricultural systems at risk of drought and high temperatures (Barron-Gafford et al., 2019). In turn, plants reduce panel temperatures to improve operational efficiency. Compared to traditional settings, Barron-Gafford et al. (2019) recorded higher or equivalent fruit production in an agrivoltaic system and a nearly 9ºC decrease in PV panel temperatures, which would result in a 3% increase in May-June PV output.

To date, agrivoltaics and the effects of smoke on agricultural crops have been examined separately. As such, research on the impact of wildfire smoke on agrivoltaics, specifically, is needed from both a solar energy and crop production perspective. Some outstanding questions that this research could address include the following:

1. How do changes in temperature associated with wildfire smoke impact energy efficiency and output in agrivoltaic settings?
2. How do smoke-driven changes in total PAR and PAR DF affect crop production in agrivoltaic settings and how do production changes (if any) vary by crop type and planting location?

The DOE Innovative Solar Practices Integrated with Rural Economies and Ecosystems (InSPIRE) project investigates the effectiveness of low-impact solar development approaches like agrivoltaics to meet growing solar demand. InSPIRE partners with operational agrivoltaic testbeds like Jack's Solar Garden outside Longmont, CO and the CSU Agricultural Research, Development and Education Center (ARDEC) in Fort Collins, CO. Additionally, the University of Arizona's Agricultural Learning Lab (ALL) (Barron-Gafford et al., 2019) is a long-running and heavily instrumented agrivoltaics test site with data available for at least five growing seasons, including low (2017, 2019) and high (2018, 2020, 2021) smoke years. The ALL has PV control, agricultural control, and agrivoltaic sites (9.1 m × 18.2 m) spaced 6 m apart. Precision integrated-circuit temperature sensors (LM35CA thermistor, Texas Instruments) measure daytime panel temperature. LI-190R Quantum Sensors (LI-COR) measure total incoming PAR on the agricultural and agrivoltaic sites. Tomato and pepper fruit production is measured at the agricultural and agrivoltaic sites at the end of each growing season (August). Data from these test sites, in combination with satellite observations, could be leveraged to study changes in irradiance, energy generation, microclimate, and crop productivity.

As in Chapters 2 and 3, observations and radiative transfer models could be used to quantify and compare total PAR and PAR DF on smoke-impacted and smoke-free days given changes in AOD and the HMS smoke densities. Analyses could compare temperature and PV

output across high and low smoke months and years to examine interannual and seasonal variation. The change in PV output can be examined directly via the panel output, if available (not all utilities provide this data), or estimated using SAM. Direct measurements of panel temperatures are typical components of agrivoltaic research sites, allowing assessment of PV output (or SAM-predicted output) and plant productivity relative to smoke-induced temperature changes. Satellite-derived cloud fraction, cloud optical depth, cloud height, AOD, and aerosol index can be drawn upon to develop detailed models of PV output and plant productivity across the control and agrivoltaic settings. Additional research needs to account for the plant location near the edge or centered beneath a panel because the exact position affects the diffuse light conditions experienced by the plant. Future work can evaluate the impact of wildfire smoke on the feasibility of agrivoltaic systems by assessing changes in solar energy and agricultural crop productivity resulting from smoke-driven variations in surface-level solar radiation and temperature.

5.2.4 Smoke and actinic flux

Future work will improve the constraints on the TUV smoke-free condition through location-specific aerosol climatologies or comparison to relatively low smoke years. While an AOD of 0.1-0.15 provides a reasonable estimate of continental aerosol conditions, typical AODs along the flight path can vary by time of day, season, year, and source. Creating more precise smoke-free conditions will improve the observation-driven computation of the change in downwelling actinic flux and allow for better calibration of model-driven results. Additionally, although TUV largely recreates the HARP observations to within 20%, the tendency to underestimate measurements necessitates the development of a bias correction to bring the modeled fluxes into greater alignment with the measured fluxes. Such correction could be

accomplished using statistical bias correction or machine learning methods to account for offsets between TUV and observations. Such methods could also prove useful for determining the optimal optical conditions under which to employ a TUV-based approach. However, identifying and accounting for the drivers of extreme values can be challenging. Finally, integration of additional satellite-derived cloud position, cloud optical depth, and surface albedo observations are needed to expand this analysis beyond the downwelling component to include changes in total actinic flux. Similarly, where available, geostationary aerosol observations may improve the smoke model in the late afternoon and evening when the MAIAC time offset is longer. However, MAIAC's improved handling of AOD retrievals under smoke conditions makes MAIAC a valuable model input.

All these incremental improvements support the ability to generalize Chapter 4's methodology to areas not sampled during WE-CAN. Ideally, this application of TUV would allow for the calculation of smoke-driven changes in surface actinic flux across more of the U.S. and especially in urban areas with complex photochemistry. By better constraining smoke-impacted photolysis rates, chemical transport models will be better able to anticipate shifts in air quality due to wildfire smoke.

5.2.5 Mapping smoke globally

I focus exclusively on North American wildfires and impacts on CONUS in this dissertation, but the expansion of fire weather and risk is a global phenomenon (Abatzoglou et al., 2019). I limited my analysis to CONUS due to each article's fundamental reliance on the HMS product, which is only available over North America. Yet, the same questions about smoke-radiation interactions and the impact on human systems are valid world-wide. As such, a global version of an HMS-like product would greatly aid a multidisciplinary research community

in answering questions about smoke-driven changes in air quality, plant productivity, solar energy production, and more.

Machine learning techniques such as random forest (RF), artificial neural networks (ANN), and convolutional neural networks (CNN) offer a potential path for developing a global HMS-like product using global satellite observing networks. Polar-orbiting satellites provide daily global coverage of AOD (e.g., MAIAC onboard Terra and Aqua), fire hot spots (e.g., MODIS onboard Terra and Aqua; VIIRS onboard the JPSS satellites), and atmospheric chemical composition (e.g., TROPOMI onboard Sentinel-5P) as well as band-specific reflectance at fine spatial resolution. Additionally, a diverse network of geostationary satellites (e.g., GOES-East, GOES-West, Himawari, GEO-KOMPSAT, and Meteosat) provide nearly global coverage at finer temporal scales, but some coverage gaps exist. Initial analyses using MAIAC and TROPOMI data to reproduce the HMS smoke classification over CONUS yield promising results. Given limited timeframes, a RF on data from August 20-22, 2018 classified smoke-impacted locations with an accuracy of 0.90, and an ANN using data from all August days from 2018-2022 achieved variable accuracy levels of 0.57 and 0.66 depending on the training-validation-test set splitting method. Further tuning and incorporation of spatial and temporal context variables is needed to improve classification accuracy. Use of band-specific radiances will also be beneficial by filling data gaps in the level 2 derived feature products. Ultimately, classifying smoke plume locations globally opens the doors to conduct much needed transdisciplinary research across historically underserved areas.

REFERENCES

Abatzoglou, J. T., Battisti, D. S., Williams, A. P., Hansen, W. D., Harvey, B. J., & Kolden, C. A. (2021). Projected increases in western US forest fire despite growing fuel constraints. *Communications Earth & Environment 2021 2:1*, *2*(1), 1–8. https://doi.org/10.1038/s43247-021-00299-0

Abatzoglou, J. T., & Williams, A. P. (2016). Impact of anthropogenic climate change on wildfire across western US forests. *Proc. Natl Acad. Sci.*, *113*(42), 11770–11775. https://doi.org/10.1073/pnas.1607171113

Abatzoglou, J. T., Williams, A. P., & Barbero, R. (2019). Global Emergence of Anthropogenic Climate Change in Fire Weather Indices. *Geophysical Research Letters*, *46*(1), 326–336. https://doi.org/10.1029/2018GL080959

Alonso-Blanco, E., Calvo, A. I., Pont, V., Mallet, M., Fraile, R., & Castro, A. (2014). Impact of biomass burning on aerosol size distribution, aerosol optical properties and associated radiative forcing. *Aerosol and Air Quality Research*, *14*, 708–724. https://doi.org/10.4209/AAQR.2013.05.0163

Apel, E. C., Hills, A. J., Lueb, R., Zindel, S., Eisele, S., & Riemer, D. D. (2003). A fast-GC/MS system to measure C_2 to C_4 carbonyls and methanol aboard aircraft. *Journal of Geophysical Research*, *108*(D20). https://doi.org/10.1029/2002jd003199

Apel, E. C., Hornbrook, R. S., Hills, A. J., Blake, N. J., Barth, M. C., Weinheimer, A., Cantrell, C., Rutledge, S. A., Basarab, B., Crawford, J., Diskin, G., Homeyer, C. R., Campos, T., Flocke, F., Fried, A., Blake, D. R., Brune, W., Pollack, I., Peischl, J., … Riemer, D. D. (2015). Upper tropospheric ozone production from lightning NO_x-impacted convection: Smoke ingestion case study from the DC3 campaign. *Journal of Geophysical Research*, *120*(6), 2505–2523. https://doi.org/10.1002/2014jd022121

Appelbaum, J., & Maor, T. (2020). Dependence of PV Module Temperature on Incident Time-Dependent Solar Spectrum. *NATO Advanced Science Institutes Series E: Applied Sciences*,

10(3), 914. https://doi.org/10.3390/app10030914

Ardani, K., Denholm, P., Mai, T., Margolis, R., Silverman, T., & Zuboy, J. (2021). *Solar Futures Study*. U.S. Department of Energy Office of Energy Efficiency & Renewable Energy. https://www.energy.gov/sites/default/files/2021-09/Solar Futures Study.pdf

Baker, K. R., Koplitz, S. N., Foley, K. M., Avey, L., & Hawkins, A. (2019). Characterizing grassland fire activity in the Flint Hills region and air quality using satellite and routine surface monitor data. *The Science of the Total Environment*, *659*, 1555–1566. https://doi.org/10.1016/J.SCITOTENV.2018.12.427

Barbieri, F., Rajakaruna, S., & Ghosh, A. (2017). Very short-term photovoltaic power forecasting with cloud modeling: A review. In *Renewable and Sustainable Energy Reviews* (Vol. 75, pp. 242–263). Elsevier Ltd. https://doi.org/10.1016/j.rser.2016.10.068

Barron-Gafford, G. A., Pavao-Zuckerman, M. A., Minor, R. L., Sutter, L. F., Barnett-Moreno, I., Blackett, D. T., Thompson, M., Dimond, K., Gerlak, A. K., Nabhan, G. P., & Macknick, J. E. (2019). Agrivoltaics provide mutual benefits across the food-energy-water nexus in drylands. *Nature Sustainability*, *2*, 848–855. https://doi.org/10.1038/s41893-019-0364-5

Baylon, P., Jaffe, D. A., Hall, S. R., Ullmann, K., Alvarado, M. J., & Lefer, B. L. (2018). Impact of Biomass Burning Plumes on Photolysis Rates and Ozone Formation at the Mount Bachelor Observatory. *Journal of Geophysical Research, D: Atmospheres*, *123*(4), 2272–2284. https://doi.org/10.1002/2017JD027341

Bian, Q., Ford, B., Pierce, J. R., & Kreidenweis, S. M. (2020). A Decadal Climatology of Chemical, Physical, and Optical Properties of Ambient Smoke in the Western and Southeastern United States. *Journal of Geophysical Research, D: Atmospheres*, *125*. https://doi.org/10.1029/2019JD031372

Bigelow, D. S., Slusser, J. R., Beaubien, A. F., & Gibson, J. H. (1998). The USDA Ultraviolet Radiation Monitoring Program. *Bulletin of the American Meteorological Society*, *79*(4), 601–615. https://doi.org/10.1175/1520-0477(1998)079<0601:TUURMP>2.0.CO;2

Brey, S. J., Ruminski, M., Atwood, S. A., & Fischer, E. V. (2018). Connecting smoke plumes to sources using Hazard Mapping System (HMS) smoke and fire location data over North

America. *Atmospheric Chemistry and Physics*, *18*(3), 1745–1761. https://doi.org/10.5194/acp-18-1745-2018

Buchholz, R. R., Park, M., Worden, H. M., Tang, W., Edwards, D. P., Gaubert, B., Deeter, M. N., Sullivan, T., Ru, M., Chin, M., Levy, R. C., Zheng, B., & Magzamen, S. (2022). New seasonal pattern of pollution emerges from changing North American wildfires. *Nature Communications*, *13*. https://doi.org/10.1038/s41467-022-29623-8

Chakrabarty, R. K., Shetty, N. J., Thind, A. S., Beeler, P., Sumlin, B. J., Zhang, C., Liu, P., Idrobo, J. C., Adachi, K., Wagner, N. L., Schwarz, J. P., Ahern, A., Sedlacek, A. J., 3rd, Lambe, A., Daube, C., Lyu, M., Liu, C., Herndon, S., Onasch, T. B., & Mishra, R. (2023). Shortwave absorption by wildfire smoke dominated by dark brown carbon. *Nature Geoscience*, *16*(8), 683–688. https://doi.org/10.1038/s41561-023-01237-9

Coop, J. D., Parks, S. A., Stevens-Rumann, C. S., Ritter, S. M., & Hoffman, C. M. (2022). Extreme fire spread events and area burned under recent and future climate in the western USA. *Global Ecology and Biogeography: A Journal of Macroecology*, *31*(10), 1949–1959. https://doi.org/10.1111/geb.13496

Corr, C. A., Hall, S. R., Ullmann, K., Anderson, B. E., Beyersdorf, A. J., Thornhill, K. L., Cubison, M. J., Jimenez, J. L., Wisthaler, A., & Dibb, J. E. (2012). Spectral absorption of biomass burning aerosol determined from retrieved single scattering albedo during ARCTAS. *Atmospheric Chemistry and Physics*, *12*(21), 10505–10518. https://doi.org/10.5194/acp-12-10505-2012

Corwin, K. A., Corr, C. A., Burkhardt, J., & Fischer, E. V. (2022a). *Data from: Smoke-driven changes in photosynthetically active radiation during the U.S. agricultural growing season* (Dryad) [dataset]. https://doi.org/10.5061/dryad.d51c5b06j

Corwin, K. A., Corr, C. A., Burkhardt, J., & Fischer, E. V. (2022b). Smoke-driven changes in photosynthetically active radiation during the U.s. agricultural growing season. *Journal of Geophysical Research Atmospheres*, *127*(23). https://doi.org/10.1029/2022jd037446

Department of Energy. (n.d.). *Cadmium Telluride*. Retrieved 2024, from https://www.energy.gov/eere/solar/cadmium-telluride

Dirnberger, D., Blackburn, G., Müller, B., & Reise, C. (2015). On the impact of solar spectral irradiance on the yield of different PV technologies. *Solar Energy Materials & Solar Cells*, *132*, 431–442. https://doi.org/10.1016/j.solmat.2014.09.034

Donaldson, D. L., Piper, D. M., & Jayaweera, D. (2021). Temporal Solar Photovoltaic Generation Capacity Reduction from Wildfire Smoke. *IEEE Access*, *9*, 79841–79852. https://doi.org/10.1109/ACCESS.2021.3084528

Dubey, S., Sarvaiya, J. N., & Seshadri, B. (2013). Temperature dependent photovoltaic (PV) efficiency and its effect on PV production in the world - A review. *Energy Procedia*, *33*, 311–321. https://doi.org/10.1016/j.egypro.2013.05.072

Dubovik, O., Holben, B., Eck, T., Smirnov, A., Kaufman, Y., King, M., Tanré, D., & Slutsker, I. (2002). Variability of absorption and optical properties of key aerosol types observed in worldwide locations. *Journal of the Atmospheric Sciences*, *59*, 590–608.

Elterman, L. (1968). UV, visible, and IR attenuation for Altitudes to 50 km. *AFCRL-68-0153, Environmental Research Paper 285, Air Force Cambridge Research Laboratories*. https://www.semanticscholar.org/paper/4fc55516c570ba62fccbb077ffcac1db30ce2b91

Evans, F. K. (1998). The Spherical Harmonics Discrete Ordinate Method for Three-Dimensional Atmospheric Radiative Transfer. *Journal of the Atmospheric Sciences*, *55*(3), 429–446. https://doi.org/10.1175/1520-0469(1998)055<0429:TSHDOM>2.0.CO;2

Feldman, D., Ramasamy, V., Fu, R., Ramdas, A., Desai, J., & Margolis, R. (2020). *U.S. Solar Photovoltaic System and Energy Storage Cost Benchmark: Q1 2020*.

Field, H. (1997). *Solar Cell Spectral Response Measurement Errors Related to Spectral Band Width and Chopped Light Waveform*. 26th IEEE Photovoltaic Specialists Conference, Anaheim, California.

Ford, B., Martin, M. V., Zelasky, S. E., Fischer, E. V., Anenberg, S. C., Heald, C. L., & Pierce, J. R. (2018). Future Fire Impacts on Smoke Concentrations, Visibility, and Health in the Contiguous United States. *GeoHealth*, *2*, 229–247. https://doi.org/10.1029/2018GH000144

Forster, P., Ramaswamy, V., Artaxo, P., Berntsen, T., Betts, R., Fahey, D., Haywood, J., Lean,

J., Lowe, D., Myhre, G., Nganga, J., Prinn, R., Raga, G., Schulz, M., & Dorland, R. (2007). Changes in Atmospheric Constituents and in Radiative Forcing. Chapter 2. In S. Solomon, D. Qin, M. Manning, Z. Chen, M. Marquis, K. B. Averyt, M. Tignor, & H. L. Miller (Eds.), *Climate Change 2007: The Physical Science Basis. Contribution of Working Group I to the Fourth Assessment Report of the Intergovernmental Panel on Climate Change*. Cambridge University Press. https://www.ipcc.ch/site/assets/uploads/2018/02/ar4-wg1-chapter2-1.pdf

Fu, Q., & Liou, K. N. (1992). On the Correlated k-Distribution Method for Radiative Transfer in Nonhomogeneous Atmospheres. *Journal of the Atmospheric Sciences*, *49*(22), 2139–2156. https://doi.org/10.1175/1520-0469(1992)049<2139:OTCDMF>2.0.CO;2

Gómez-Amo, J. L., Estellés, V., Marcos, C., Segura, S., Esteve, A. R., Pedrós, R., Utrillas, M. P., & Martínez-Lozano, J. A. (2017). Impact of dust and smoke mixing on column-integrated aerosol properties from observations during a severe wildfire episode over Valencia (Spain). *The Science of the Total Environment*, *599-600*, 2121–2134.

Gómez-Amo, J. L., Freile-Aranda, M. D., Camarasa, J., Estellés, V., Utrillas, M. P., & Martínez-Lozano, J. A. (2019). Empirical estimates of the radiative impact of an unusually extreme dust and wildfire episode on the performance of a photovoltaic plant in Western Mediterranean. *Applied Energy*, *235*, 1226–1234. https://doi.org/10.1016/J.APENERGY.2018.11.052

Grand View Research. (n.d.). *Solar Cell Market Size, Share | Industry Report, 2022*. Retrieved 2024, from https://www.grandviewresearch.com/industry-analysis/solar-cell-market

Green, M. A., Dunlop, E. D., Siefer, G., Yoshita, M., Kopidakis, N., Bothe, K., & Hao, X. (2023). Solar cell efficiency tables (Version 61). *Progress in Photovoltaics: Research and Applications*, *31*(1), 3–16. https://doi.org/10.1002/PIP.3646

Greenwald, R., Bergin, M. H., Xu, J., Cohan, D., Hoogenboom, G., & Chameides, W. L. (2006). The influence of aerosols on crop production: A study using the CERES crop model. *Agricultural Systems*, *89*(2-3), 390–413. https://doi.org/10.1016/j.agsy.2005.10.004

Gueymard, C. A. (2008). REST2: High-performance solar radiation model for cloudless-sky irradiance, illuminance, and photosynthetically active radiation - Validation with a

benchmark dataset. *Solar Energy*, *82*(3), 272–285. https://doi.org/10.1016/j.solener.2007.04.008

Hallar, A. G., Molotch, N. P., Hand, J. L., Livneh, B., McCubbin, I. B., Petersen, R., Michalsky, J., Lowenthal, D., & Kunkel, K. E. (2017). Impacts of increasing aridity and wildfires on aerosol loading in the intermountain Western US. *Environmental Research Letters: ERL [Web Site]*, *12*(1), 014006. https://doi.org/10.1088/1748-9326/AA510A

Hall, S. R., Ullmann, K., Prather, M. J., Flynn, C. M., Murray, L. T., Fiore, A. M., Correa, G., Strode, S. A., Steenrod, S. D., Lamarque, J.-F., Guth, J., Josse, B., Flemming, J., Huijnen, V., Abraham, N. L., & Archibald, A. T. (2018). Cloud impacts on photochemistry: building a climatology of photolysis rates from the Atmospheric Tomography mission. *Atmospheric Chemistry and Physics*, *18*(22), 16809–16828. https://doi.org/10.5194/acp-18-16809-2018

Harrison, L., Michalsky, J., & Berndt, J. (1994). Automated multifilter rotating shadow-band radiometer: an instrument for optical depth and radiation measurements. *Applied Optics*, *33*(22), 5118. https://doi.org/10.1364/ao.33.005118

Hemes, K. S., Verfaillie, J., & Baldocchi, D. D. (2020). Wildfire-Smoke Aerosols Lead to Increased Light Use Efficiency Among Agricultural and Restored Wetland Land Uses in California's Central Valley. *Journal of Geophysical Research: Biogeosciences*, *125*(2), 1–21. https://doi.org/10.1029/2019JG005380

He, S., & Carmichael, G. R. (1999). Sensitivity of photolysis rates and ozone production in the troposphere to aerosol properties. *Journal of Geophysical Research*, *104*(D21), 26307–26324. https://doi.org/10.1029/1999jd900789

Higuera, P. E., & Abatzoglou, J. T. (2021). Record-setting climate enabled the extraordinary 2020 fire season in the western United States. *Global Change Biology*, *27*, 1–2. https://doi.org/10.1111/gcb.15388

Hodshire, A. L., Akherati, A., Alvarado, M. J., Brown-Steiner, B., Jathar, S. H., Jimenez, J. L., Kreidenweis, S. M., Lonsdale, C. R., Onasch, T. B., Ortega, A. M., & Pierce, J. R. (2019). Aging Effects on Biomass Burning Aerosol Mass and Composition: A Critical Review of Field and Laboratory Studies. *Environmental Science and Technology*, *53*, 10007–10022.

https://doi.org/10.1021/acs.est.9b02588

Hodshire, A. L., Bian, Q., Ramnarine, E., Lonsdale, C. R., Alvarado, M. J., Kreidenweis, S. M., Jathar, S. H., & Pierce, J. R. (2019). More Than Emissions and Chemistry: Fire Size, Dilution, and Background Aerosol Also Greatly Influence Near-Field Biomass Burning Aerosol Aging. *Journal of Geophysical Research, D: Atmospheres*, *124*, 5589–5611. https://doi.org/10.1029/2018JD029674

Hoff, S. (2016). *U.S. electric system is made up of interconnections and balancing authorities - Today in Energy - U.S. Energy Information Administration (EIA)*. https://www.eia.gov/todayinenergy/detail.php?id=27152

Hofmann, H., Wickham, H., & Kafadar, K. (2017). Letter-Value Plots: Boxplots for Large Data. *Journal of Computational and Graphical Statistics*, *26*(3), 469–477. https://doi.org/10.1080/10618600.2017.1305277

Holben, B. N., Eck, T. F., Slutsker, I., Tanré, D., Buis, J. P., Setzer, A., Vermote, E., Reagan, J. A., Kaufman, Y. J., Nakajima, T., Lavenu, F., Jankowiak, I., & Smirnov, A. (1998). AERONET - A federated instrument network and data archive for aerosol characterization. *Remote Sensing of Environment*, *66*(1), 1–16. https://doi.org/10.1016/S0034-4257(98)00031-5

Jaffe, D. A., O'Neill, S. M., Larkin, N. K., Holder, A. L., Peterson, D. L., Halofsky, J. E., & Rappold, A. G. (2020). Wildfire and prescribed burning impacts on air quality in the United States. *Journal of the Air & Waste Management Association* , *70*(6), 583–615. https://doi.org/10.1080/10962247.2020.1749731

Jethva, H., Torres, O., & Yoshida, Y. (2019). Accuracy assessment of MODIS land aerosol optical thickness algorithms using AERONET measurements over North America. *Atmospheric Measurement Techniques*, *12*, 4291–4307. https://doi.org/10.5194/AMT-12-4291-2019

Juliano, T. W., Jiménez, P. A., Kosović, B., Eidhammer, T., Thompson, G., Berg, L. K., Fast, J., Motley, A., & Polidori, A. (2022). Smoke from 2020 United States wildfires responsible for substantial solar energy forecast errors. *Environmental Research Letters: ERL [Web Site]*, *17*(3), 034010. https://doi.org/10.1088/1748-9326/AC5143

Juncosa Calahorrano, J. F., Lindaas, J., O'Dell, K., Palm, B. B., Peng, Q., Flocke, F., Pollack, I. B., Garofalo, L. A., Farmer, D. K., Pierce, J. R., Collett, J. L., Weinheimer, A., Campos, T., Hornbrook, R. S., Hall, S. R., Ullmann, K., Pothier, M. A., Apel, E. C., Permar, W., … Fischer, E. V. (2021). Daytime Oxidized Reactive Nitrogen Partitioning in Western U.S. Wildfire Smoke Plumes. *Journal of Geophysical Research, D: Atmospheres*, *126*(4). https://doi.org/10.1029/2020JD033484

Kankiewicz, A., Sengupta, M., & Moon, D. (2010). Observed impacts of transient clouds on utility-scale PV fields. *American Solar Energy Society*.

Kanniah, K. D., Beringer, J., North, P., & Hutley, L. (2012). Control of atmospheric particles on diffuse radiation and terrestrial plant productivity: A review. *Progress in Physical Geography*, *36*(2), 209–237. https://doi.org/10.1177/0309133311434244

Kaulfus, A. S., Nair, U., Jaffe, D., Christopher, S. A., & Goodrick, S. (2017). Biomass Burning Smoke Climatology of the United States: Implications for Particulate Matter Air Quality. *Environmental Science & Technology*, *51*(20), 11731–11741. https://doi.org/10.1021/acs.est.7b03292

Kern, E. C., Jr, Gulachenski, E. M., & Kern, G. A. (1989). Cloud effects on distributed photovoltaic generation slow transients at the Gardner Massachusetts photovoltaic experiment. *IEEE Transactions on Energy Conversion*, *4*(2), 184–190.

Kirchstetter, T. W., Novakov, T., & Hobbs, P. V. (2004). Evidence that the spectral dependence of light absorption by aerosols is affected by organic carbon. *Journal of Geophysical Research, D: Atmospheres*, *109*(21). https://doi.org/10.1029/2004JD004999

Knohl, A., & Baldocchi, D. D. (2008). Effects of diffuse radiation on canopy gas exchange processes in a forest ecosystem. *Journal of Geophysical Research: Biogeosciences*, *113*(2), 1–17. https://doi.org/10.1029/2007JG000663

Lappalainen, K., & Valkealahti, S. (2015). Recognition and modelling of irradiance transitions caused by moving clouds. *Solar Energy*, *112*, 55–67. https://doi.org/10.1016/j.solener.2014.11.018

Lappalainen, K., & Valkealahti, S. (2016). Apparent velocity of shadow edges caused by moving clouds. *Solar Energy*, *138*, 47–52. https://doi.org/10.1016/j.solener.2016.09.008

Lau, C. Y., Gan, C. K., Baharin, K. A., & Sulaima, M. F. (2015). A review on the impacts of passing-clouds on distribution network connected with solar photovoltaic system. *International Review of Electrical Engineering*, *10*(3), 449–457. https://doi.org/10.15866/iree.v10i3.5817

Lebegue, B., Schmidt, M., Ramonet, M., Wastine, B., Kwok, C. Y., Laurent, O., Belviso, S., Guemri, A., Philippon, C., Smith, J., & Conil, S. (2016). Comparison of nitrous oxide (NO) analyzers for high-precision measurements of atmospheric mole fractions. *Atmospheric Measurement Techniques*, *9*, 1221–1238. https://doi.org/10.5194/amt-8-3867-2015

Lee, S. C., Knox, S. H., McKendry, I., & Black, T. A. (2022). Biogeochemical and biophysical responses to episodes of wildfire smoke from natural ecosystems in southwestern British Columbia, Canada. *Atmospheric Chemistry and Physics*, *22*(4), 2333–2349. https://doi.org/10.5194/ACP-22-2333-2022

Lewis, K., Arnott, W. P., Moosmüller, H., & Wold, C. E. (2008). Strong spectral variation of biomass smoke light absorption and single scattering albedo observed with a novel dual-wavelength photoacoustic instrument. *Journal of Geophysical Research*, *113*(D16). https://doi.org/10.1029/2007jd009699

Lill, E., Lindaas, J., Juncosa Calahorrano, J. F., Campos, T., Flocke, F., Apel, E. C., Hornbrook, R. S., Hills, A., Jarnot, A., Blake, N., Permar, W., Hu, L., Weinheimer, A., Tyndall, G., Montzka, D. D. e., Hall, S. R., Ullmann, K., Thornton, J., Palm, B. B., … Fischer, E. V. (2022). Wildfire-driven changes in the abundance of gas-phase pollutants in the city of Boise, ID during summer 2018. *Atmospheric Pollution Research*, *13*(1), 101269. https://doi.org/10.1016/j.apr.2021.101269

Lin, C.-A., Zhang, Y., Heath, G., Henze, D. K., Sengupta, M., & Lu, C.-H. (2023). Improvement of aerosol optical depth data for localized solar resource assessment. *Solar Energy*, *249*, 457–466. https://doi.org/10.1016/j.solener.2022.11.047

Lindaas, J., Farmer, D. K., Pollack, I. B., Abeleira, A., Flocke, F., Roscioli, R., Herndon, S., & Fischer, E. V. (2017). Changes in ozone and precursors during two aged wildfire smoke events in the Colorado Front Range in summer 2015. *Atmospheric Chemistry and Physics*, *17*(17), 10691–10707. https://doi.org/10.5194/acp-17-10691-2017

Lindaas, J., Pollack, I. B., Garofalo, L. A., Pothier, M. A., Farmer, D. K., Kreidenweis, S. M., Campos, T. L., Flocke, F., Weinheimer, A. J., Montzka, D. D., Tyndall, G. S., Palm, B. B., Peng, Q., Thornton, J. A., Permar, W., Wielgasz, C., Hu, L., Ottmar, R. D., Restaino, J. C., … Fischer, E. V. (2021). Emissions of Reactive Nitrogen From Western U.S. Wildfires

During Summer 2018. *Journal of Geophysical Research, D: Atmospheres*, *126*(2). https://doi.org/10.1029/2020JD032657

Liou, K. N. (2002). *An Introduction to Atmospheric Radiation*. Elsevier. https://play.google.com/store/books/details?id=mQ1DiDpX34UC

Li, X., Mauzerall, D. L., & Bergin, M. H. (2020). Global reduction of solar power generation efficiency due to aerosols and panel soiling. *Nature Sustainability*, *3*(9), 720–727. https://doi.org/10.1038/s41893-020-0553-2

Li, X., Wagner, F., Peng, W., Yang, J., & Mauzerall, D. L. (2017). Reduction of solar photovoltaic resources due to air pollution in China. *Proceedings of the National Academy of Sciences of the United States of America*, *114*(45), 11867–11872. https://doi.org/10.1073/pnas.1711462114

Lopes, F. M., Silva, H. G., Salgado, R., Cavaco, A., Canhoto, P., & Collares-Pereira, M. (2018). Short-term forecasts of GHI and DNI for solar energy systems operation: assessment of the ECMWF integrated forecasting system in southern Portugal. *Solar Energy*, *170*, 14–30. https://doi.org/10.1016/j.solener.2018.05.039

Lyapustin, A., & Wang, Y. (2018a). *MCD19A2 MODIS/Terra + Aqua land aerosol optical depth daily L2G Global 1km SIN Grid V006* [dataset]. NASA EOSDIS Land Processes DAAC. https://doi.org/10.5067/MODIS/MCD19A2.006

Lyapustin, A., & Wang, Y. (2018b). *MODIS Multi-Angle Implementation of Atmospheric Correction (MAIAC) Data User's Guide Collection 6 (ver. of June 2018) Version 2.0*.

Lyapustin, A., & Wang, Y. (2022). *MODIS Multi-Angle Implementation of Atmospheric Correct (MAIAC) Data User's Guide Collection 6.1 Version 3.1*. https://lpdaac.usgs.gov/documents/1500/MCD19_User_Guide_V61.pdf

Lyapustin, A., Wang, Y., Korkin, S., & Huang, D. (2018). MODIS Collection 6 MAIAC algorithm. *Atmospheric Measurement Techniques*, *11*(10), 5741–5765. https://doi.org/10.5194/amt-11-5741-2018

Maclaurin, G., Grue, N. W., Lopez, A., & Heimiller, D. (2019). *The renewable energy potential (reV) model: A geospatial platform for technical potential and supply curve modeling*. https://doi.org/10.2172/1563140

Madronich, S., & Flocke, S. (1999). The Role of Solar Radiation in Atmospheric Chemistry. In P. Boule (Ed.), *The Handbook of Environmental Chemistry Vol. 2 Part L Environmental Photochemistry*. Springer-Verlag.

McClure, C. D., & Jaffe, D. A. (2018). US particulate matter air quality improves except in wildfire-prone areas. *Proceedings of the National Academy of Sciences of the United States of America*, *115*(31), 7901–7906. https://doi.org/10.1073/pnas.1804353115

McKendry, I. G., Christen, A., Lee, S.-C., Ferrara, M., Strawbridge, K. B., O'Neill, N., & Black, A. (2019). Impacts of an intense wildfire smoke episode on surface radiation, energy and carbon fluxes in southwestern British Columbia, Canada. *Atmospheric Chemistry and Physics*, *19*(2), 835–846. https://doi.org/10.5194/acp-19-835-2019

Minnis, P., Sun-Mack, S., Young, D. F., Heck, P. W., Garber, D. P., Chen, Y., Spangenberg, D. A., Arduini, R. F., Trepte, Q. Z., Smith, W. L., Ayers, J. K., Gibson, S. C., Miller, W. F., Hong, G., Chakrapani, V., Takano, Y., Liou, K. N., Xie, Y., & Yang, P. (2011). CERES edition-2 cloud property retrievals using TRMM VIRS and Terra and Aqua MODIS data-Part I: Algorithms. *IEEE Transactions on Geoscience and Remote Sensing: A Publication of the IEEE Geoscience and Remote Sensing Society*, *49*(11), 4374–4400. https://doi.org/10.1109/TGRS.2011.2144601

Miskin, C. K., Li, Y., Perna, A., Ellis, R. G., Grubbs, E. K., Bermel, P., & Agrawal, R. (2019). Sustainable co-production of food and solar power to relax land-use constraints. *Nature Sustainability*, *2*(10), 972–980. https://doi.org/10.1038/s41893-019-0388-x

Möhler, R. L., & Goodin, D. G. (2012). Mapping Burned Areas in the Flint Hills of Kansas and Oklahoma, 2000—2010. *Great Plains Research*, *22*, 15–25. https://about.jstor.org/terms

Munshi, A. H., Sasidharan, N., Pinkayan, S., Barth, K. L., Sampath, W. S., & Ongsakul, W. (2018). Thin-film CdTe photovoltaics – The technology for utility scale sustainable energy generation. *Solar Energy*, *173*, 511–516. https://doi.org/10.1016/j.solener.2018.07.090

NASA Goddard Space Flight Center. (2016, July 13). *Aerosol Optical Thickness, MODIS, 2000-2016*. NASA Scientific Visualization Studio. https://svs.gsfc.nasa.gov/12302/#section_credits

National Oceanic and Atmospheric Administration ESRL Global Monitoring Laboratory. (2005). *Global Radiation and Aerosols - SURFRAD Aerosol Optical Depth*. https://gml.noaa.gov/grad/surfrad/aod/

National Oceanic and Atmospheric Administration National Environmental Satellite, Data, and Information Service. (n.d.). *Hazard Mapping System fire and smoke product* [dataset]. https://www.ospo.noaa.gov/Products/land/hms.html

NOAA. (2022). *GOES-R Series Product Definition and Users' Guide (PUG) - Volume 5: Level 2+ Products*. https://www.ospo.noaa.gov/Organization/Documents/PUG/GS%20Series%20416-R-PUG-L2%20Plus-0349%20Vol%205%20v2.4.pdf

Nominal Operating Cell Temperature. (n.d.). PVEducation. https://www.pveducation.org/pvcdrom/modules-and-arrays/nominal-operating-cell-temperature#footnote2_udgxwr4

Nuvolone, D., Petri, D., & Voller, F. (2018). The effects of ozone on human health. *Environmental Science and Pollution Research International*, *25*(9), 8074–8088. https://doi.org/10.1007/s11356-017-9239-3

O'Dell, K., Bilsback, K., Ford, B., Martenies, S. E., Magzamen, S., Fischer, E. V., & Pierce, J. R. (2021). Estimated Mortality and Morbidity Attributable to Smoke Plumes in the United States: Not Just a Western US Problem. *GeoHealth*, *5*(9), e2021GH000457. https://doi.org/10.1029/2021GH000457

O'Dell, K., Ford, B., Fischer, E. V., & Pierce, J. R. (2019). Contribution of Wildland-Fire Smoke to US PM 2.5 and Its Influence on Recent Trends. *Environmental Science and Technology*, *53*, 1797–1804. https://doi.org/10.1021/acs.est.8b05430

O'Dell, K., Hornbrook, R. S., Permar, W., Levin, E. J. T., Garofalo, L. A., Apel, E. C., Blake, N. J., Jarnot, A., Pothier, M. A., Farmer, D. K., Hu, L., Campos, T., Ford, B., Pierce, J. R., &

Fischer, E. V. (2020). Hazardous Air Pollutants in Fresh and Aged Western US Wildfire Smoke and Implications for Long-Term Exposure. *Environmental Science & Technology*, *54*(19), 11838–11847. https://doi.org/10.1021/acs.est.0c04497

O'Neill, B. C., Kriegler, E., Ebi, K. L., Kemp-Benedict, E., Riahi, K., Rothman, D. S., van Ruijven, B. J., van Vuuren, D. P., Birkmann, J., Kok, K., Levy, M., & Solecki, W. (2017). The roads ahead: Narratives for shared socioeconomic pathways describing world futures in the 21st century. *Global Environmental Change: Human and Policy Dimensions*, *42*, 169–180. https://doi.org/10.1016/J.GLOENVCHA.2015.01.004

Osterwald, C. R. (2003). Standards, Calibration and Testing of PV Modules and Solar Cells. *Practical Handbook of Photovoltaics: Fundamentals and Applications*, 793–816. https://doi.org/10.1016/B978-185617390-2/50034-9

Park, R. J., Jacob, D. J., Chin, M., & Martin, R. V. (2003). Sources of carbonaceous aerosols over the United States and implications for natural visibility. *Journal of Geophysical Research*, *108*(D12). https://doi.org/10.1029/2002jd003190

Park, Y. H., Sokolik, I. N., & Hall, S. R. (2020). The Impact of Smoke on the Ultraviolet and Visible Radiative Forcing Under Different Fire Regimes. *Air, Soil and Water Research*, *11*(1). https://doi.org/10.1177/1178622118774803

Peppler, R. A., Bahrmann, C. P., Barnard, J. C., Campbell, J. R., Cheng, M. D., Ferrare, R. A., Halthore, R. N., Heilman, L. A., Hlavka, D. L., Laulainen, N. S., Lin, C. J., Ogren, J. A., Poellot, M. R., Remer, L. A., Sassen, K., Spinhirne, J. D., Splitt, M. E., & Turner, D. D. (2000). ARM Southern Great Plains Site Observations of the Smoke Pall Associated with the 1998 Central American Fires. *Bulletin of the American Meteorological Society*, *81*(11), 2563–2591. https://doi.org/10.1175/1520-0477(2000)081<2563:ASGPSO>2.3.CO;2

Permar, W., Wang, Q., Selimovic, V., Wielgasz, C., Yokelson, R. J., Hornbrook, R. S., Hills, A. J., Apel, E. C., Ku, I.-T., Zhou, Y., Sive, B. C., Sullivan, A. P., Collett, J. L., Jr, Campos, T. L., Palm, B. B., Peng, Q., Thornton, J. A., Garofalo, L. A., Farmer, D. K., … Hu, L. (2021). Emissions of trace organic gases from western U.s. wildfires based on WE-CAN aircraft measurements. *Journal of Geophysical Research*, *126*(11). https://doi.org/10.1029/2020jd033838

Perry, M., & Troccoli, A. (2015). Impact of a fire burn on solar irradiance and PV power. *Solar Energy*, *114*, 167–173. https://doi.org/10.1016/J.SOLENER.2015.01.005

Petty, G. W. (2006). *A First Course in Atmospheric Radiation*. Sundog Pub. https://play.google.com/store/books/details?id=YpspAQAAMAAJ

Pierce, J. R., Val Martin, M., & Heald, C. L. (2017). *Estimating the Effects of Changing Climate on Fires and Consequences for U.S. Air Quality, Using a Set of Global and Regional Climate Models*.

Platnick, S. et al. (2015). MODIS Atmosphere L3 Daily Product. In *NASA MODIS Adaptive Processing System*. Goddard Space Flight Center. https://doi.org/10.5067/MODIS/MYD08_D3.061

Ramnarine, E., Kodros, J. K., Hodshire, A. L., Lonsdale, C. R., Alvarado, M. J., & Pierce, J. R. (2019). Effects of near-source coagulation of biomass burning aerosols on global predictions of aerosol size distributions and implications for aerosol radiative effects. *Atmospheric Chemistry and Physics*, *19*, 6561–6577. https://doi.org/10.5194/ACP-19-6561-2019

Rangel-Cárdenas, J., & Sobral, H. (2017). Optical Absorption Enhancement in CdTe Thin Films by Microstructuration of the Silicon Substrate. *Materials*, *10*(607). https://doi.org/10.3390/ma10060607

Reid, J. S., Eck, T. F., Christopher, S. A., Koppmann, R., Dubovik, O., Eleuterio, D. P., Holben, B. N., Reid, E. A., & Zhang, J. (2005). A review of biomass burning emissions part III: intensive optical properties of biomass burning particles. *Atmospheric Chemistry and Physics*, *5*, 827–849.

Ridley, D. A., Heald, C. L., Ridley, K. J., & Kroll, J. H. (2018). Causes and consequences of decreasing atmospheric organic aerosol in the United States. *Proceedings of the National Academy of Sciences of the United States of America*, *115*(2), 290–295. https://doi.org/10.1073/pnas.1700387115

Roderick, M. L., Farquhar, G. D., Berry, S. L., & Noble, I. R. (2001). On the direct effect of clouds and atmospheric particles on the productivity and structure of vegetation. *Oecologia*, *129*, 21–30. https://doi.org/10.1007/s004420100760

Rogers, C. M., & Bowman, K. P. (2001). Transport of smoke from the Central American fires of 1998. *Journal of Geophysical Research, D: Atmospheres*, *106*(D22), 28357–28368. https://doi.org/10.1029/2000JD000187

Rolph, G. D., Draxler, R. R., Stein, A. F., Taylor, A., Ruminski, M. G., Kondragunta, S., Zeng, J., Huang, H.-C., Manikin, G., McQueen, J. T., & Davidson, P. M. (2009). Description and Verification of the NOAA Smoke Forecasting System: The 2007 Fire Season. *Weather and Forecasting*, *24*(2), 361–378. https://doi.org/10.1175/2008WAF2222165.1

Ross, R. G., Jr. (1980). *Flat-plate photovoltaic array design optimization*. https://ui.adsabs.harvard.edu/abs/1980pvsp.conf.1126R

Ross, J. L., & Hobbs, P. V. (1998). Radiative characteristics of regional hazes dominated by smoke from biomass burning in Brazil: Closure tests and direct radiative. *Journal of Geophysical Research*, *103*(D24), 31,925–931,941.

Ross, R., & Smokler, M. (1986). *Flat-Plate Solar Array Project: Final report: Volume 6, Engineering sciences and reliability*. https://www.osti.gov/biblio/6802984

Ruminski, M., Kondragunta, S., Draxler, R., & Zeng, J. (2006). Recent changes to the hazard mapping system. *Proceedings of the 15th International Emission Inventory Conference*, *15*, 18. https://gaftp.epa.gov/air/nei/ei_conference/EI15/session10/ruminiski.pdf

Rutan, D. A., Kato, S., Doelling, D. R., Rose, F. G., Nguyen, L. T., Caldwell, T. E., & Loeb, N. G. (2015). CERES Synoptic Product: Methodology and Validation of Surface Radiant Flux. *Journal of Atmospheric and Oceanic Technology*, *32*(6), 1121–1143. https://doi.org/10.1175/JTECH-D-14-00165.1

Safford, H. D., Paulson, A. K., Steel, Z. L., Young, D. J. N., & Wayman, R. B. (2022). The 2020 California fire season: A year like no other, a return to the past or a harbinger of the future? *Global Ecology and Biogeography: A Journal of Macroecology*, *31*(10), 2005–2025. https://doi.org/10.1111/geb.13498

Sarver, T., Al-Qaraghuli, A., & Kazmerski, L. L. (2013). A comprehensive review of the impact of dust on the use of solar energy: History, investigations, results, literature, and mitigation approaches. *Renewable and Sustainable Energy Reviews*, *22*, 698–733.

https://doi.org/10.1016/J.RSER.2012.12.065

Schiferl, L. D., & Heald, C. L. (2018). Particulate matter air pollution may offset ozone damage to global crop production. *Atmospheric Chemistry and Physics*, *18*(8), 5953–5966. https://doi.org/10.5194/acp-18-5953-2018

Schroedter-Homscheidt, M., Benedetti, A., & Killius, N. (2017). Verification of ECMWF and ECMWF/MACC's global and direct irradiance forecasts with respect to solar electricity production forecasts. *Meteorologische Zeitschrift*, *26*(1), 1–19. https://doi.org/10.1127/metz/2016/0676

Sengupta, M., Xie, Y., Lopez, A., Habte, A., Maclaurin, G., & Shelby, J. (2018). The National Solar Radiation Data Base (NSRDB). *Renewable and Sustainable Energy Reviews*, *89*, 51–60. https://doi.org/10.1016/J.RSER.2018.03.003

Shen, Y., Pokhrel, R. P., Sullivan, A. P., Levin, E. J. T., Garofalo, L. A., Farmer, D. K., Permar, W., Hu, L., Toohey, D. W., Campos, T., Fischer, E. V., & Murphy, S. M. (2024). Understanding absorption by black versus brown carbon in biomass burning plumes from the WE-CAN campaign. In *EGUsphere*. https://doi.org/10.5194/egusphere-2023-3114

Sinclair, T. R., Shiraiwa, T., & Hammer, G. L. (1992). Variation in Crop Radiation-Use Efficiency with Increased Diffuse Radiation. *Crop Science*, *32*(5), 1281–1284. https://doi.org/10.2135/CROPSCI1992.0011183X003200050043X

Skoplaki, E., & Palyvos, J. A. (2009). On the temperature dependence of photovoltaic module electrical performance: A review of efficiency/power correlations. *Solar Energy*, *83*(5), 614–624. https://doi.org/10.1016/j.solener.2008.10.008

Tahir, Z. R., Kanwal, A., Asim, M., Bilal, M., Abdullah, M., Saleem, S., Mujtaba, M. A., Veza, I., Mousa, M., & Kalam, M. A. (2022). Effect of Temperature and Wind Speed on Efficiency of Five Photovoltaic Module Technologies for Different Climatic Zones. *Sustainability: Science Practice and Policy*, *14*. https://doi.org/10.3390/su142315810

U.S. Department of Agriculture. (n.d.). *The Ultraviolet Radiation Monitoring and Research Program* [dataset]. https://uvb.nrel.colostate.edu/UVB/

U.S. Energy Information Administration. (2018). *A Guide to EIA Electric Power Data*. U.S. Department of Energy. https://www.eia.gov/electricity/data/guide/pdf/guide.pdf

U.S. Energy Information Administration. (2021). *Electric Power Monthly - U.S. Energy Information Administration (EIA)*. https://www.eia.gov/electricity/monthly/epm_table_grapher.php?t=epmt_1_01_a

U.S. Environmental Protection Agency. (2017). *Integrated science assessment for sulfur oxides: Health criteria* (No. EPA/600/R-17/451). U.S. Environmental Protection Agency, Office of Research and Development, National Center for Environmental Assessment-RTP.

U.S. Environmental Protection Agency. (2019). *Integrated Science Assessment for Particulate Matter* (No. EPA/600/R-19/188).

Val Martin, M., Heald, C. L., Lamarque, J.-F., Tilmes, S., Emmons, L. K., & Schichtel, B. A. (2015). How emissions, climate, and land use change will impact mid-century air quality over the United States: a focus on effects at national parks. *Atmospheric Chemistry and Physics*, *15*(5), 2805–2823. https://doi.org/10.5194/acp-15-2805-2015

Val Martin, M., Kahn, R. A., & Tosca, M. G. (2018). A Global Analysis of Wildfire Smoke Injection Heights Derived from Space-Based Multi-Angle Imaging. *Remote Sensing 2018, Vol. 10, Page 1609*, *10*(10), 1609. https://doi.org/10.3390/RS10101609

van Vuuren, D. P., Edmonds, J., Kainuma, M., Riahi, K., Thomson, A., Hibbard, K., Hurtt, G. C., Kram, T., Krey, V., Lamarque, J.-F., Masui, T., Meinshausen, M., Nakicenovic, N., Smith, S. J., & Rose, S. K. (2011). The representative concentration pathways: an overview. *Climatic Change*, *109*(1), 5–31. https://doi.org/10.1007/S10584-011-0148-Z

Wang, J., Van Den Heever, S. C., & Reid, J. S. (2009). A conceptual model for the link between Central American biomass burning aerosols and severe weather over the south central United States. *Environmental Research Letters: ERL [Web Site]*, *4*(1), 015003. https://doi.org/10.1088/1748-9326/4/1/015003

Wang, S. C., Wang, Y., Estes, M., Lei, R., Talbot, R., Zhu, L., & Hou, P. (2018). Transport of Central American Fire Emissions to the U.S. Gulf Coast: Climatological Pathways and Impacts on Ozone and PM2.5. *Journal of Geophysical Research, D: Atmospheres*, *123*(15),

8344–8361. https://doi.org/10.1029/2018JD028684

Westerling, A. L. (2016). Increasing western US forest wildfire activity: sensitivity to changes in the timing of spring. *Philosophical Transactions of the Royal Society of London. Series B, Biological Sciences*, *371*(20150178). https://doi.org/10.1098/rstb.2015.0178

Westerling, A. L., Gershunov, A., Brown, T. J., Cayan, D. R., & Dettinger, M. D. (2003). Climate and Wildfire in the Western United States. *Bulletin of the American Meteorological Society*, *84*(5), 595–604. https://doi.org/10.1175/BAMS-84-5-595

Westerling, A. L., Hidalgo, H. G., Cayan, D. R., & Swetnam, T. W. (2006). Warming and Earlier Spring Increase Western U.S. Forest Wildfire Activity. *Science*, *313*(5789), 940–943. https://doi.org/10.1126/SCIENCE.1128834

Wielicki, B. A., Barkstrom, B. R., Harrison, E. F., Lee, R. B., Smith, G. L., & Cooper, J. E. (1996). Clouds and the Earth's Radiant Energy System (CERES): An Earth Observing System Experiment. *Bulletin of the American Meteorological Society*, *77*, 853–868.

Xie, Y., Sengupta, M., & Dudhia, J. (2016). A Fast All-sky Radiation Model for Solar applications (FARMS): Algorithm and performance evaluation. *Solar Energy*, *135*, 435–445. https://doi.org/10.1016/j.solener.2016.06.003

Xue, Z., Gupta, P., & Christopher, S. (2021). Satellite-based estimation of the impacts of summertime wildfires on PM 2.5 concentration in the United States. *Atmospheric Chemistry and Physics*, *21*, 11243–11256. https://doi.org/10.5194/acp-21-11243-2021

Yue, X., Mickley, L. J., Logan, J. A., & Kaplan, J. O. (2013). Ensemble projections of wildfire activity and carbonaceous aerosol concentrations over the western United States in the mid-21st century. *Atmospheric Environment*, *77*, 767–780. https://doi.org/10.1016/J.ATMOSENV.2013.06.003

Zengir, B., Bayhan, M., & Kavasoğlu, S. (2006). Optical Absorption in Polycrystalline CdTe Thin Films. *Çankaya Üniversitesi Fen-Edebiyat Fakültesi Journal of Arts and Sciences*, *5*.

APPENDIX A1

SUPPLEMENTAL INFORMATION FOR CHAPTER 2

Introduction

Materials in the SI include four additional figures, one table, and a text section that shows the results of a sensitivity study referenced within the main article text. The first figure (Figure A1.1) presents a comparison between the PAR values calculated via a linear interpolation across six adjacent MFRSR wavelength bands and those measured by a collocated pyranometer. This figure is referenced within the methods section. The second figure (Figure A1.2) shows how many three-minute observations are available per day across the 10 sites and 15 years after initial data cleaning. The third figure (Figure A1.3) provides a summary of monthly trends across all 10 UVMPR sites analyzed. Site-specific trends are shown in Figure 2.3 in Section 2.3.1 of the article. The fourth figure (Figure A1.4) shows site-specific linear regressions comparing daily CF and PAR DF on smoke-free and smoke-impacted days. An aggregate version of Figure A1.4 is presented and discussed in Figure 2.6 in Section 2.3.3 of the article. Table A1.1 describes the distribution of smoke-free and smoke-impacted clear-sky days that are displayed in Figure 2.7 of Section 2.3.4. Text A1.1 examines the sensitivity of the results in Section 2.3.3 to the number of smoke-impacted days at the SE site where smoke-haze mixing is most likely to occur. Such mixing can pose a challenge for plume edge detection in the HMS smoke product, which is why we consider the HMS product a conservative estimate of smoke-impacted days.

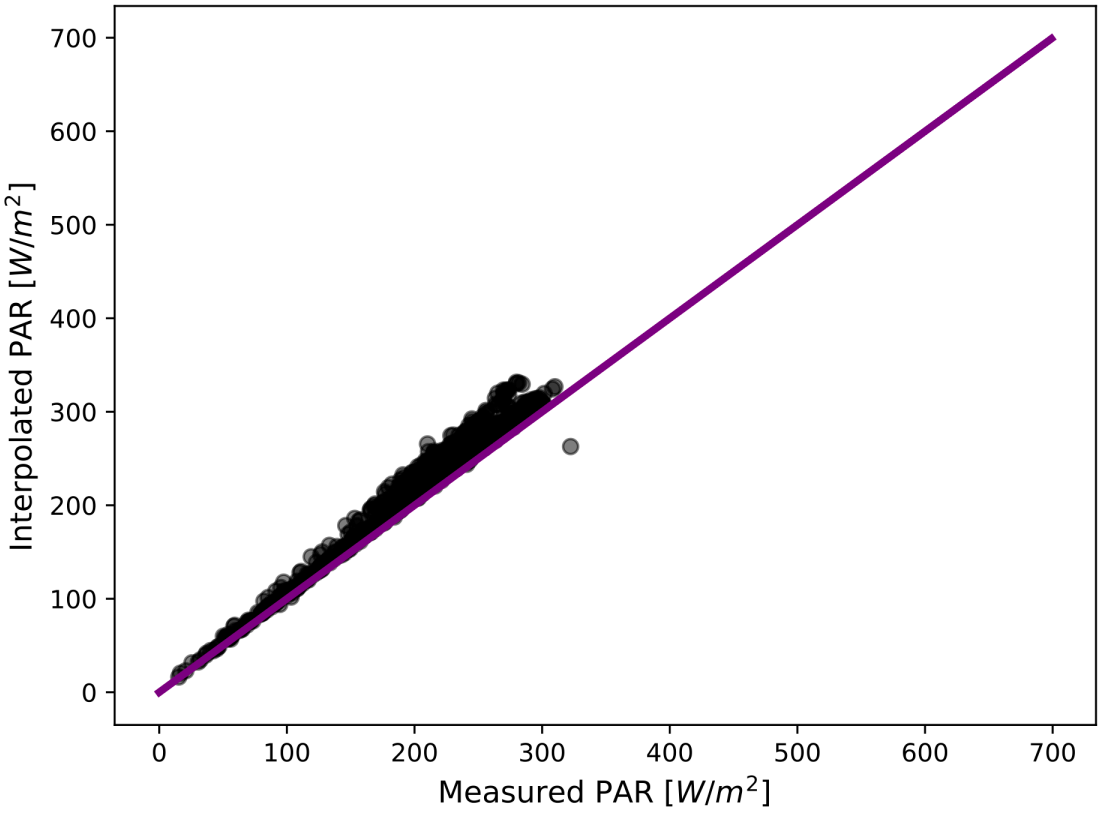

Figure A1.1: Scatter plot showing a direct comparison of the measured and interpolated PAR values at the Pawnee, Colorado UVMRP site from 2015-2019. The equality line (y = x) is shown in purple.

To validate the PAR interpolation method, we compared the interpolated total PAR values to total PAR measured by a collocated broadband (400-700 nm) PAR LI-190SA Quantum Sensor from LI-COR for a subset of years (2015-2019) at the Pawnee, CO site. Interpolated PAR values were calculated using six adjacent wavelengths from 368-870 nm measured by the MFRSR monitors on-site. Measured PAR values were converted to irradiance units of W/m^2 by dividing by a factor of 4.6 (Biggs, 1986).

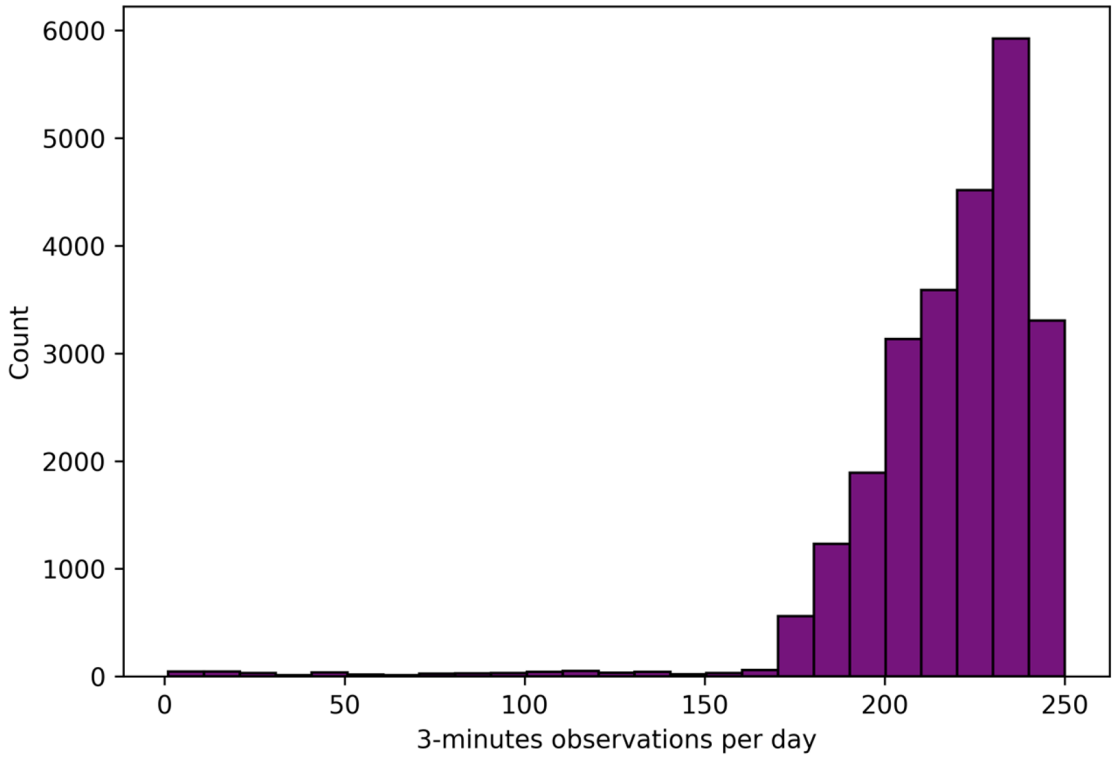

Figure A1.2: Histogram showing the number of three-minute irradiance observations remaining after initial data cleaning and quality control. The histogram includes observations from the 10 UVMRP sites studied and uses 25 bins of width 10. The maximum number of observations possible per day is 250, which equals 12.5 hours of data. Nearly all days had between 170 and 250 observations (8.5-12.5 hours), but 2.25% of days had less than 170 observations. We remove the days with less than 170 observations under the assumption that we lack sufficient data to characterize daily irradiance.

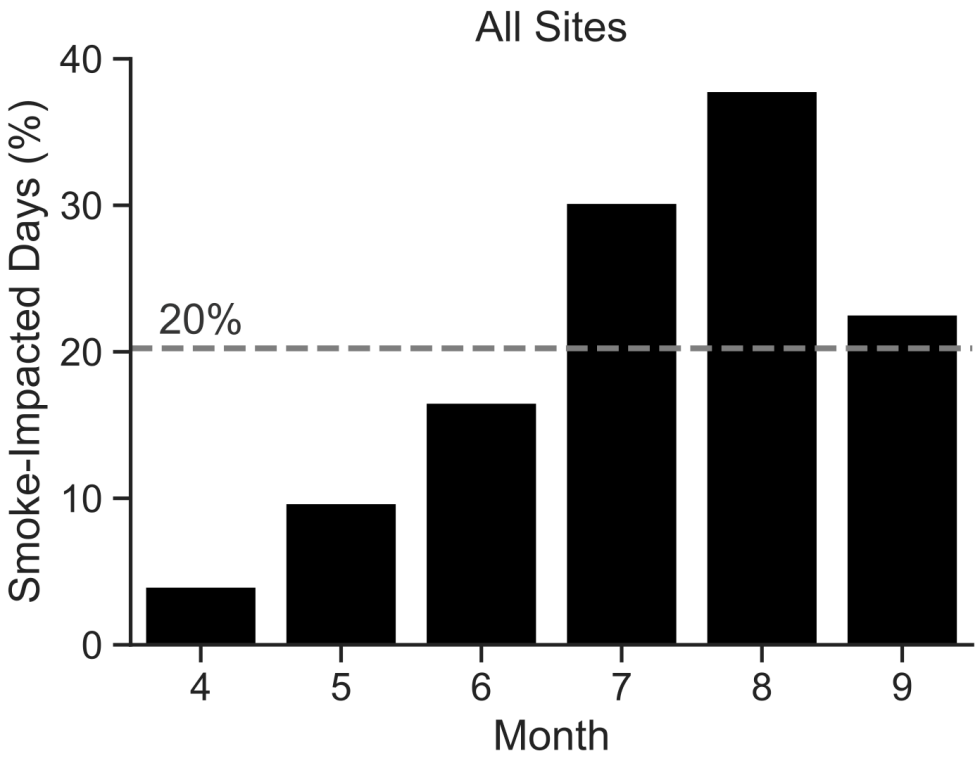

Figure A1.3: Percentage of days in each month (black bars) during the growing season (April-September) from 2006-2020 when smoke was present in the atmospheric column above the 10 UVMRP sites. The overall percentage of smoke-impacted days across the growing season at these sites is indicated via the dashed line.

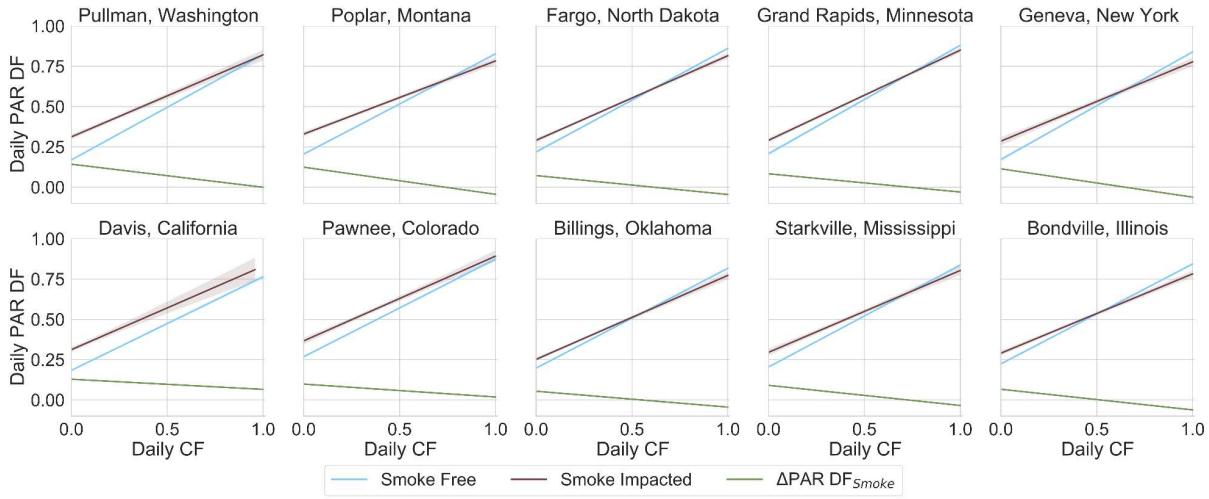

Figure A1.4: Linear regressions showing daily PAR DF by CF for all growing season days at each UVMRP site analyzed from 2006-2020 on smoke-impacted (brown) and smoke-free (blue) days. Shading of the same color indicates the 95% confidence intervals. Narrow confidence intervals means that shading is not visible on all lines. The change in PAR DF (ΔPAR DF$_{Smoke}$) between smoke-impacted and smoke-free days is presented in green.

Table A1.1: Site-specific distribution of clear-sky days showing the number and percentage identified as smoke-free and smoke-impacted.

Site location	Total clear-sky days at site	Percent of clear-sky days (all sites) from this site	Number of smoke-free clear-sky days at this site	Number of smoke-impacted clear-sky days at this site	Percent of smoke-free clear-sky days (all sites) from this site	Percent of smoke-impacted clear-sky day (all sites) from this site	Percent of days at site that are smoke-impacted
Davis, CA	1270	36%	1043	227	41%	23%	18%
Pawnee, CO	317	9%	241	76	10%	8%	24%
Bondville, IL	156	4%	112	44	4%	4%	28%
Grand Rapids, MN	176	5%	97	79	4%	8%	45%
Starkville, MS	187	5%	168	19	7%	2%	10%
Poplar, MT	323	9%	183	140	7%	14%	43%
Geneva, NY	111	3%	92	19	4%	2%	17%
Fargo, ND	191	5%	90	101	4%	10%	53%
Billings, OK	296	8%	202	94	8%	10%	32%
Pullman, WA	479	14%	290	189	12%	19%	39%
Total	3506	100%	2518	988	101%	100%	N/A

Text A1.1:

As noted in Section 2.2.2, accurately detecting smoke plume edges in areas with high levels of anthropogenic haze is a limitation of the HMS smoke product. This limitation is the primary reason why we consider the HMS smoke product a conservative estimate of smoke-impacted days. Eight of the ten UVMRP sites selected (Pullman, WA; Pawnee Nunn, CO; Poplar, MT; Fargo, ND; Bondville, IL; Billings, OK; Geneva, NY; Grand Rapids, MN) are not

located in areas with high levels of anthropogenic haze where such issues would pose a problem. The Davis, CA site is located near sources of anthropogenic haze; however, Davis is mainly impacted by dense local smoke plumes that present easier targets for accurate edge detection. The SE site in Starkville, MS is the site where issues with plume edge detection due to smoke-haze mixing would have the highest likelihood of leading to an underestimation of smoke-impacted days.

We performed a sensitivity analysis focused on the SE site to see how increasing the number of smoke-impacted days at the SE site affects the overall DF values calculated in Sections 2.3.3 and 2.3.4. We examined this using a lagged smoke approach wherein we reclassified smoke-free days into smoke-impacted days if the smoke-free day immediately followed an HMS-indicated smoke-impacted day. The inclusion of lagged smoke days results in little to no change in the trends or DF values we report. Below we include a side-by-side comparison of Figure 2.6 from Section 2.3.3 (left) and a version including the lagged smoke days at the SE site (right). In both cases, there is a 10-percentage point increase in clear-sky PAR DF and the linear regression parameters remain the same. This highlights the consistency of the results and lack of sensitivity to potential plume edge detection issues with the HMS smoke product at the SE site. The results in Figures 2.7 and 2.8 in Section 2.3.4 similarly showed a lack of sensitivity to increasing smoke-impacted days at the SE site.

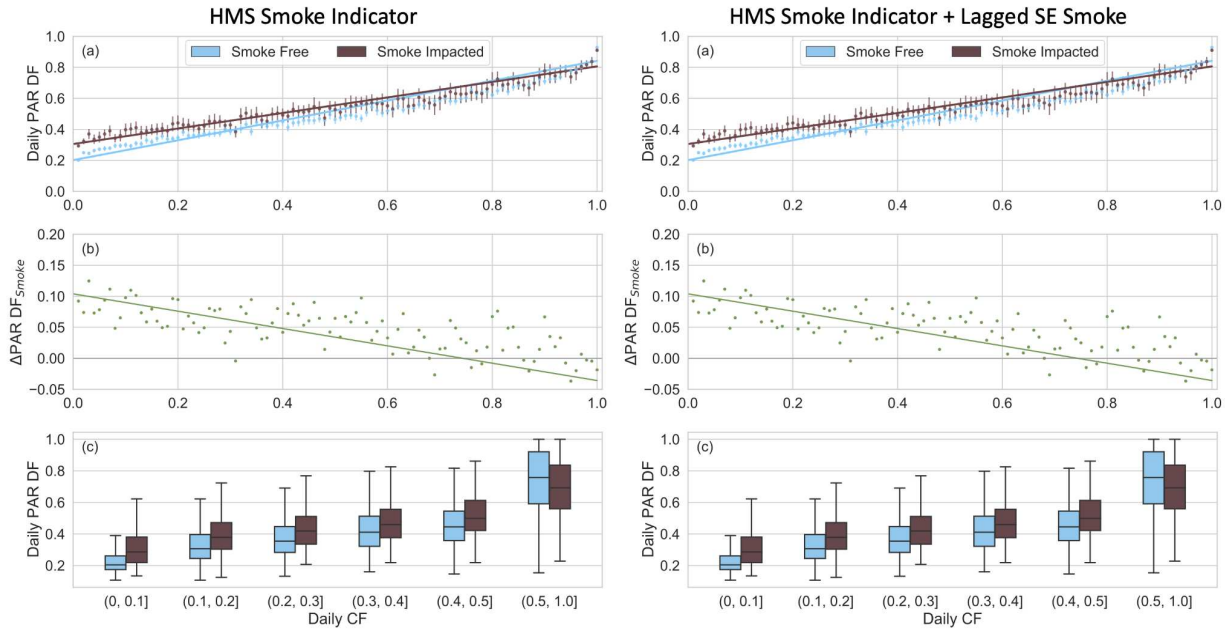
HMS Smoke Indicator
HMS Smoke Indicator + Lagged SE Smoke
(a)
Smoke Free
Smoke Impacted
Daily PAR DF
(b)
ΔPAR DF$_{smoke}$
(c)
(0, 0.1]
(0.1, 0.2]
(0.2, 0.3]
(0.3, 0.4]
(0.4, 0.5]
(0.5, 1.0]
Daily CF

APPENDIX A2

SUPPLEMENTAL INFORMATION FOR CHAPTER 3

Table A2.1: Mean daily clear-sky DNI and GHI for September 2019 and 2020 that were used as inputs to a model of PV output for a 1 MW stationary PV installation located in the listed 13 cities across CONUS.

			September 2019		**September 2020**	
Location	***Latitude***	***Longitude***	***Clear-sky DNI***	***Clear-sky GHI***	***Clear-sky DNI***	***Clear-sky GHI***
Los Angeles, CA	34.13	-118.42	827.06	645.79	585.65	585.41
Modesto, CA	37.65	-121.02	820.23	620.17	558.45	554.70
Phoenix, AZ	33.57	-112.10	813.01	638.75	732.39	626.27
Denver, CO	39.77	-104.86	891.35	628.10	771.77	609.40
Portland, OR	45.53	-122.66	791.96	550.54	641.40	516.39
Spokane, WA	47.65	-117.42	819.35	543.15	717.18	520.87
Bozeman, MT	45.69	-111.06	833.00	569.06	764.10	555.85
Omaha, NE	41.25	-96.06	765.94	573.25	691.74	565.20
Minneapolis, MN	44.97	-93.26	763.37	547.59	680.39	536.92
Dallas, TX	32.81	-96.78	753.52	621.05	688.55	610.09
Atlanta, GA	33.77	-84.42	781.72	631.57	773.25	627.46
New York, NY	40.73	-73.90	755.11	579.16	729.04	572.73
Portland, ME	43.69	-70.26	806.74	570.34	758.08	558.68

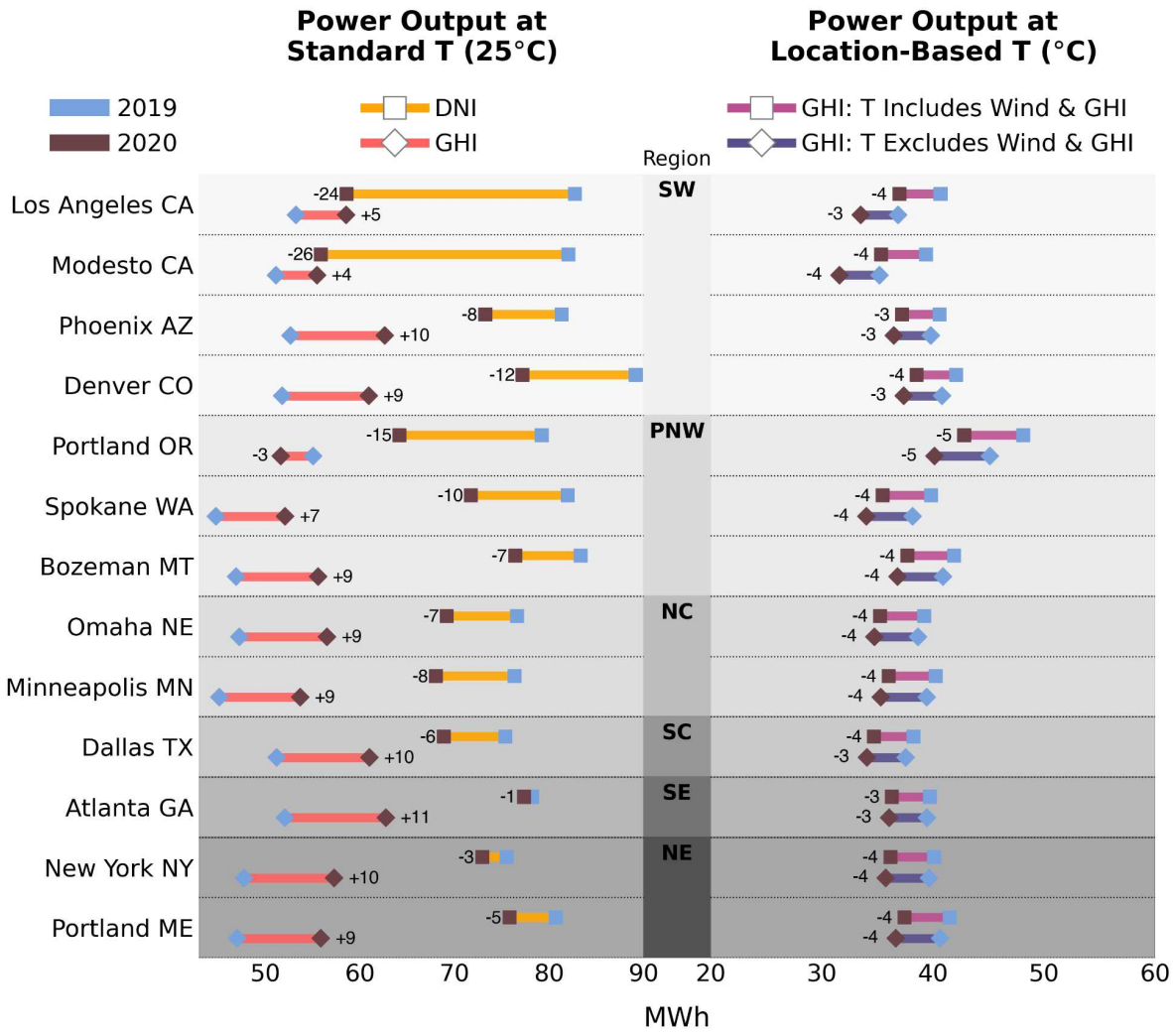

Figure A2.1: Comparison of modeled average daytime power output (MWh) in September for 1 MW PV installations of CdTe panels at 13 locations across CONUS in a low (blue; 2019) and high (brown; 2020) smoke year. Each site's region is indicated with grayscale shading consistent with the map in Figure 3.4. Power output was modeled using four approaches: two with panel temperatures set to a standard temperature of 25°C (left panel) and two with panel temperatures determined by location (right panel). At 25°C, power output was modeled using clear-sky DNI (orange) and clear-sky GHI (red) as the irradiance input. At location-based temperatures, power output was modeled using clear-sky GHI as the irradiance input, but temperature was determined either including (light purple) or excluding (dark purple) the cooling effects of wind and warming effects of radiation. The clear-sky DNI and GHI for each location were determined using the data underlying Figure 3.3 and are reported in Table A2.1.

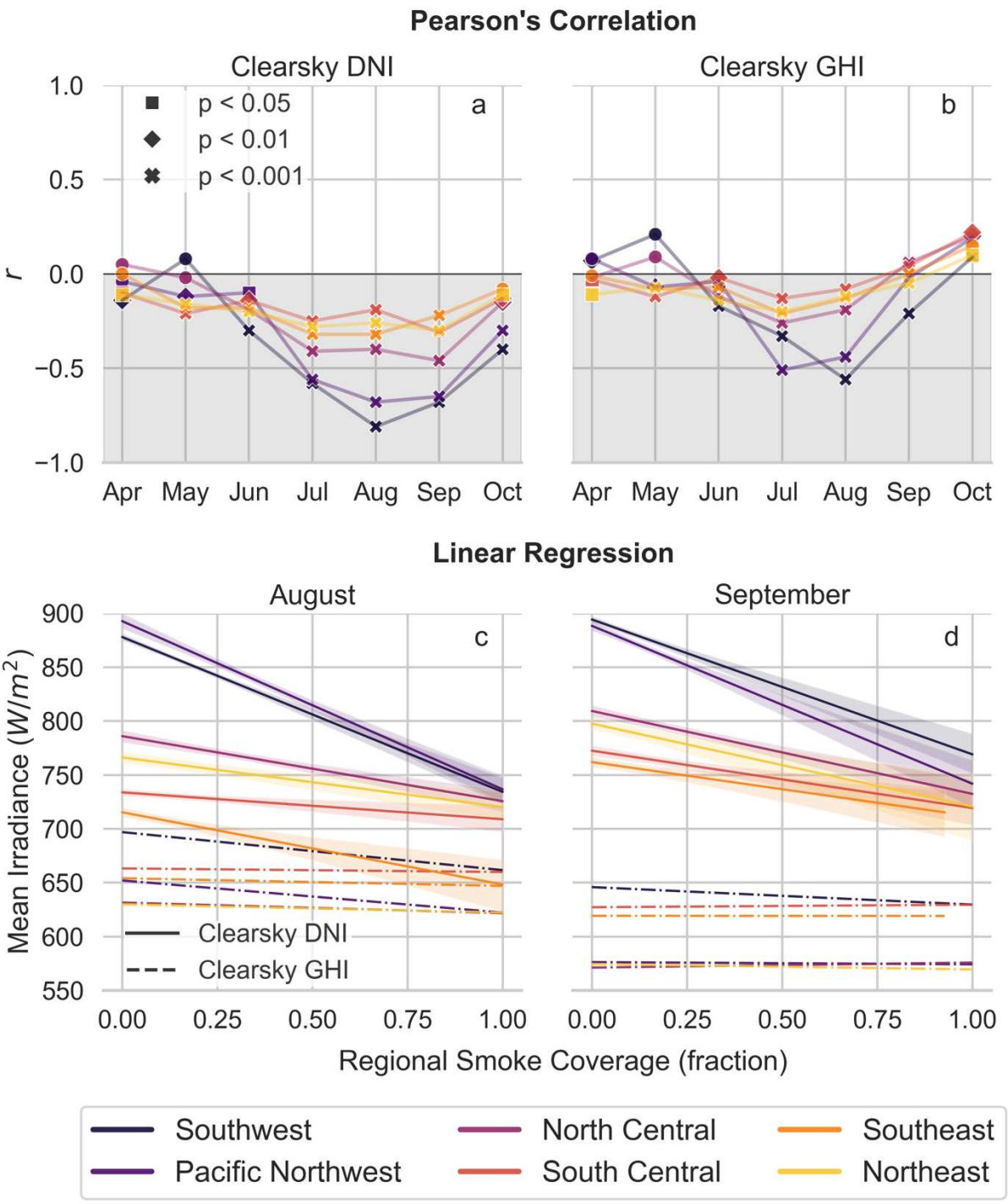

Figure A2.2: Comparison of daily regional smoke coverage (i.e., the percent of each region that is smoke-impacted) to daily mean regional irradiance for all April-October CONUS days from 2006-2021. Pearson's correlation coefficients (top row) are displayed for each month from April-October for clear-sky DNI (a) and clear-sky GHI (b). Simple linear regression results (bottom row) are displayed for clear-sky DNI (solid) and clear-sky GHI (dashed) independent variables for August (c) and September (d). Shading represents the 95% confidence interval.

Table A2.2: Monthly Pearson's correlation (*r*) and simple linear regression (a_1 = slope, a_0 = intercept) results comparing daily regional smoke coverage (fraction from 0-1) and clear-sky DNI and GHI (W/m^2) from April-October of 2006-2021.

		Clear-sky DNI					Clear-sky GHI				
Region	***Month***	***a_1***	***a_0***	***r***	***R^2***	***significance***	***Slope***	***Intercept***	***r***	***R2***	***significance***
Southwest	April	-48.0	897.9	-0.14	0.02	$p < 0.01$	14.6	710.3	0.07	0.00	
Southwest	May	36.9	880.1	0.08	0.01		38.2	734.2	0.21	0.04	$p < 0.001$
Southwest	June	-44.1	884.7	-0.30	0.09	$p < 0.001$	-10.7	739.6	-0.17	0.03	$p < 0.001$
Southwest	July	-97.1	862.6	-0.58	0.33	$p < 0.001$	-21.6	717.1	-0.33	0.11	$p < 0.001$
Southwest	August	-143.7	878.0	-0.81	0.65	$p < 0.001$	-35.3	696.9	-0.56	0.31	$p < 0.001$
Southwest	September	-125.1	894.3	-0.68	0.46	$p < 0.001$	-16.2	645.9	-0.21	0.04	$p < 0.001$
Southwest	October	-77.6	911.5	-0.40	0.16	$p < 0.001$	16.1	569.1	0.09	0.01	$p < 0.05$
Pacific Northwest	April	-9.7	872.4	-0.04	0.00		14.8	651.6	0.08	0.01	
Pacific Northwest	May	-29.6	862.9	-0.12	0.02	$p < 0.01$	-6.4	688.4	-0.07	0.01	
Pacific Northwest	June	-15.7	875.8	-0.10	0.01	$p < 0.05$	-2.4	699.1	-0.04	0.00	
Pacific Northwest	July	-79.3	882.8	-0.56	0.31	$p < 0.001$	-22.7	689.2	-0.51	0.26	$p < 0.001$
Pacific Northwest	August	-156.1	892.7	-0.68	0.46	$p < 0.001$	-29.8	652.1	-0.44	0.19	$p < 0.001$
Pacific Northwest	September	-146.6	888.4	-0.65	0.43	$p < 0.001$	-2.0	576.3	-0.02	0.00	
Pacific Northwest	October	-59.1	877.5	-0.30	0.09	$p < 0.001$	46.2	482.5	0.19	0.04	$p < 0.001$
North Central	April	19.1	796.4	0.05	0.00		-2.7	643.0	-0.02	0.00	
North Central	May	-3.4	784.9	-0.02	0.00		6.1	670.5	0.09	0.01	$p < 0.05$

North Central	June	-25.6	785.8	-0.19	0.04	p < 0.001	-4.9	675.9	-0.12	0.02	p < 0.01
North Central	July	-55.3	790.5	-0.41	0.17	p < 0.001	-9.3	664.3	-0.26	0.07	p < 0.001
North Central	August	-60.4	786.0	-0.40	0.16	p < 0.001	-9.8	631.5	-0.19	0.04	p < 0.001
North Central	September	-76.9	809.4	-0.46	0.21	p < 0.001	4.6	571.2	0.06	0.00	
North Central	October	-38.5	833.9	-0.15	0.02	p < 0.01	40.4	491.3	0.20	0.04	p < 0.001
South Central	April	-38.5	789.9	-0.10	0.01	p < 0.05	-4.5	687.8	-0.03	0.00	
South Central	May	-49.9	759.9	-0.21	0.05	p < 0.001	-8.0	698.7	-0.12	0.01	p < 0.01
South Central	June	-17.4	745.3	-0.14	0.02	p < 0.01	-0.7	691.2	-0.02	0.00	
South Central	July	-34.8	730.3	-0.25	0.06	p < 0.001	-4.7	681.1	-0.13	0.02	p < 0.01
South Central	August	-24.9	733.8	-0.19	0.04	p < 0.001	-3.3	663.2	-0.08	0.01	
South Central	September	-53.2	772.5	-0.31	0.09	p < 0.001	2.4	627.2	0.04	0.00	
South Central	October	-29.6	829.4	-0.13	0.02	p < 0.01	28.7	571.9	0.22	0.05	p < 0.001
Northeast	April	-92.9	803.4	-0.11	0.01	p < 0.05	-35.4	646.2	-0.11	0.01	p < 0.05
Northeast	May	-47.6	788.1	-0.16	0.03	p < 0.001	-6.5	672.0	-0.07	0.00	
Northeast	June	-48.8	779.2	-0.20	0.04	p < 0.001	-10.3	676.0	-0.14	0.02	p < 0.01
Northeast	July	-54.6	759.6	-0.28	0.08	p < 0.001	-11.0	659.7	-0.20	0.04	p < 0.001
Northeast	August	-46.0	766.2	-0.26	0.07	p < 0.001	-7.6	629.9	-0.12	0.02	p < 0.01
Northeast	September	-77.0	797.6	-0.30	0.09	p < 0.001	-5.0	574.5	-0.05	0.00	
Northeast	October	-45.1	824.9	-0.11	0.01	p < 0.05	27.4	491.4	0.10	0.01	p < 0.05
Southeast	April	-1.4	782.5	0.00	0.00		-2.3	679.4	-0.01	0.00	
Southeast	May	-55.4	755.5	-0.18	0.03	p < 0.001	-7.1	691.8	-0.08	0.01	
Southeast	June	-34.5	725.4	-0.18	0.03	p < 0.001	-3.5	683.0	-0.07	0.00	
Southeast	July	-66.9	707.4	-0.32	0.10	p < 0.001	-10.5	672.3	-0.21	0.04	p < 0.001
Southeast	August	-67.0	715.3	-0.32	0.11	p < 0.001	-7.1	654.1	-0.13	0.02	p < 0.01
Southeast	September	-50.3	761.9	-0.22	0.05	p < 0.001	-0.1	619.2	0.00	0.00	
Southeast	October	-29.0	813.0	-0.08	0.01		30.2	561.1	0.15	0.02	p < 0.01

APPENDIX A3

SUPPLEMENTAL INFORMATION FOR CHAPTER 4

The analysis presented in Chapter 4 focuses on a single WE-CAN research flight (RF08); however, I conducted similar initial analyses on three additional flights: RF02 (July 26, 2018), RF05 (August 2, 2018), and RF06 (August 3, 2018). Figures A3.1-A3.3 provide results for a subset of RF19 that was cloud-free, smoke-free, and characterized by low AODs. This flight segment demonstrates the strength of the methodology used in Chapter 4 under ideal atmospheric conditions. Figures A3.4-A3.8 provide initial results of the TUV model and HARP measurement comparisons for these three flights. Additionally, I investigated RF06 in greater detail for a presentation at the 2024 American Meteorological Society (AMS) conference in Baltimore, MD. Figures A3.9-A3.13 were included in my AMS presentation.

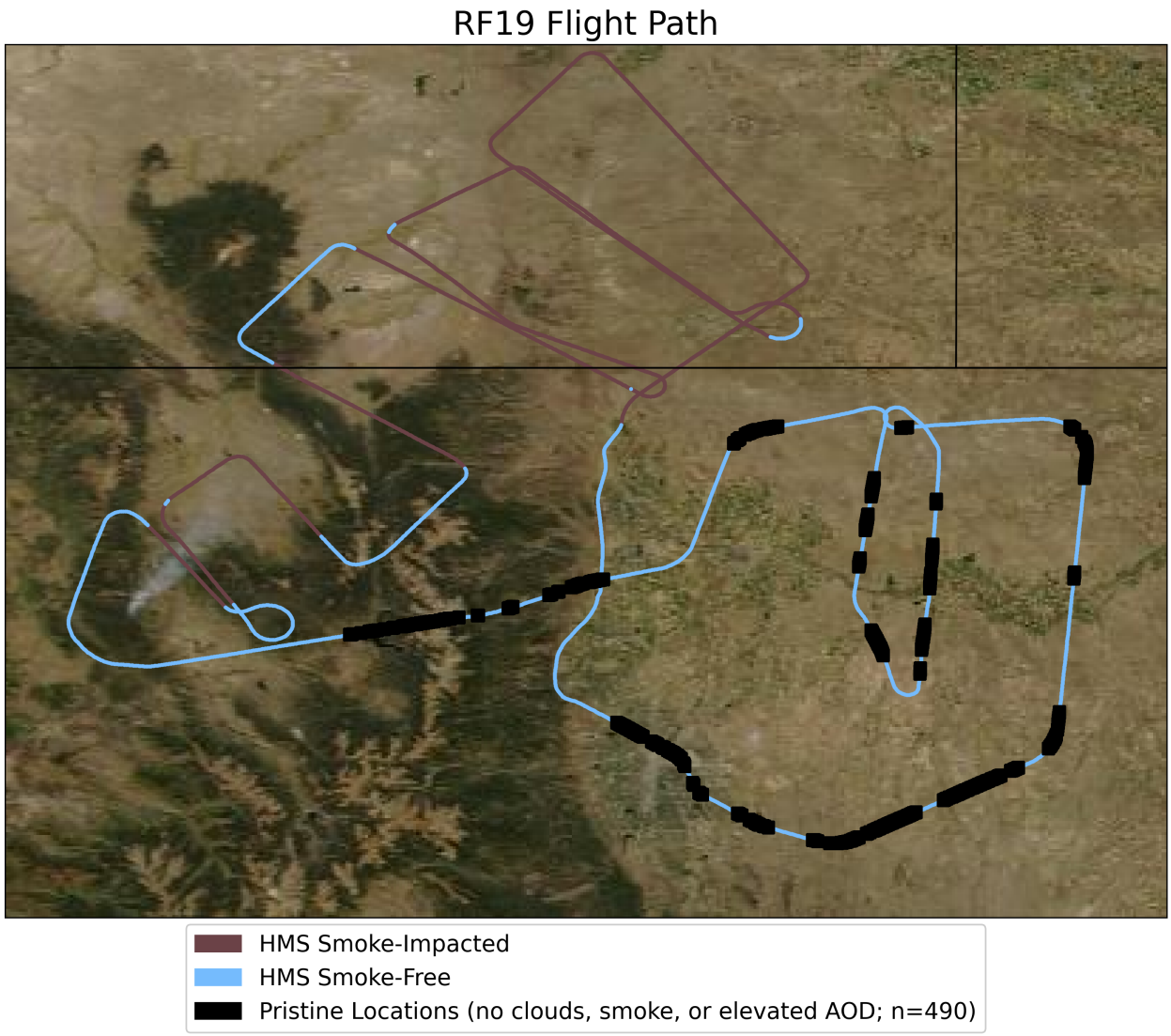

Figure A3.1: Map of the RF19 flight path showing smoke-free (blue) and smoke-impacted (brown) locations as determined using the HMS. Pristine locations (black) are indicated and defined as cloud-free and smoke-free areas characterized by low AODs (i.e.,< 0.15).

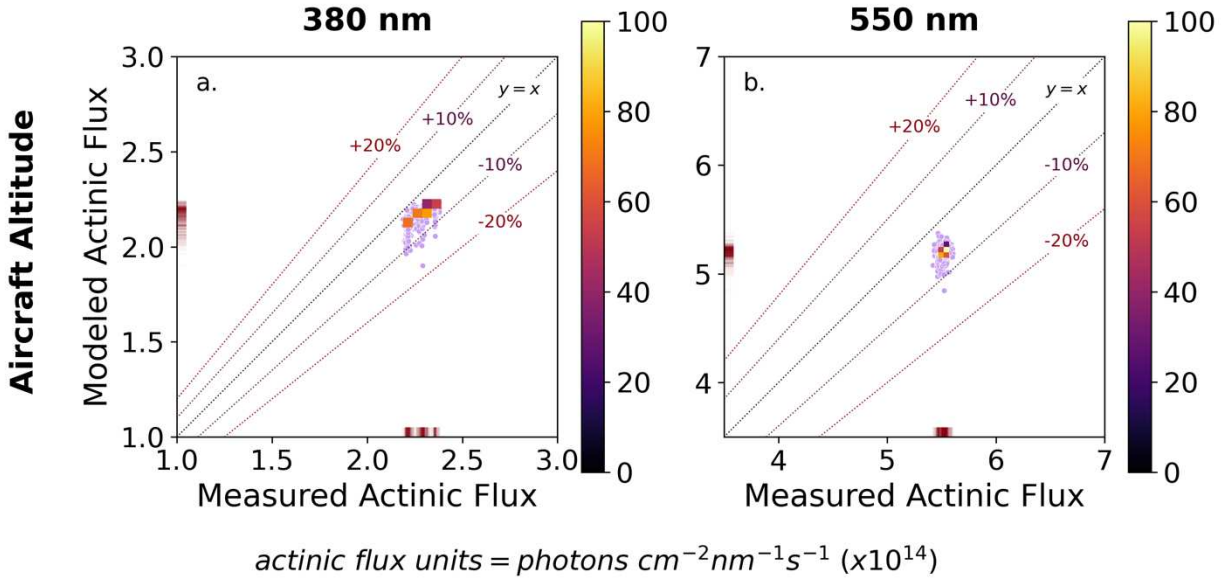

Figure A3.2: Comparison of TUV modeled and HARP measured F↓ (photons cm^{-2} nm^{-1} s^{-1}) for the RF19 pristine locations at 380 nm (a) and 550 nm (b) at the altitude of the aircraft. Individual points are shown (purple) with an overlapping histogram heat map that indicates the point concentration in each plot position (colorbar). Rugplots (red) along the x and y axes display the distribution of measured and modeled values, respectively. TUV nearly reproduces HARP measurements under pristine conditions with a slight bias low given the designated inputs.

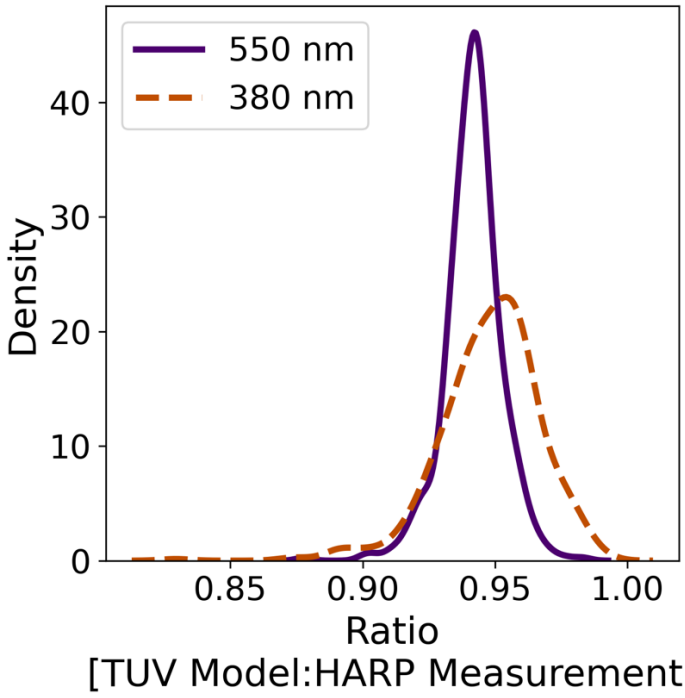

Figure A3.3: Kernel density estimate plot of the distribution of the ratio of the TUV modeled fluxes to HARP measurements at 380 nm (orange dashed line) and 550 nm (purple solid line) for RF19 pristine locations. F↓ from TUV and HARP align closely under pristine conditions (i.e., near 1) with TUV slightly underestimating the HARP measurements given the designated inputs.

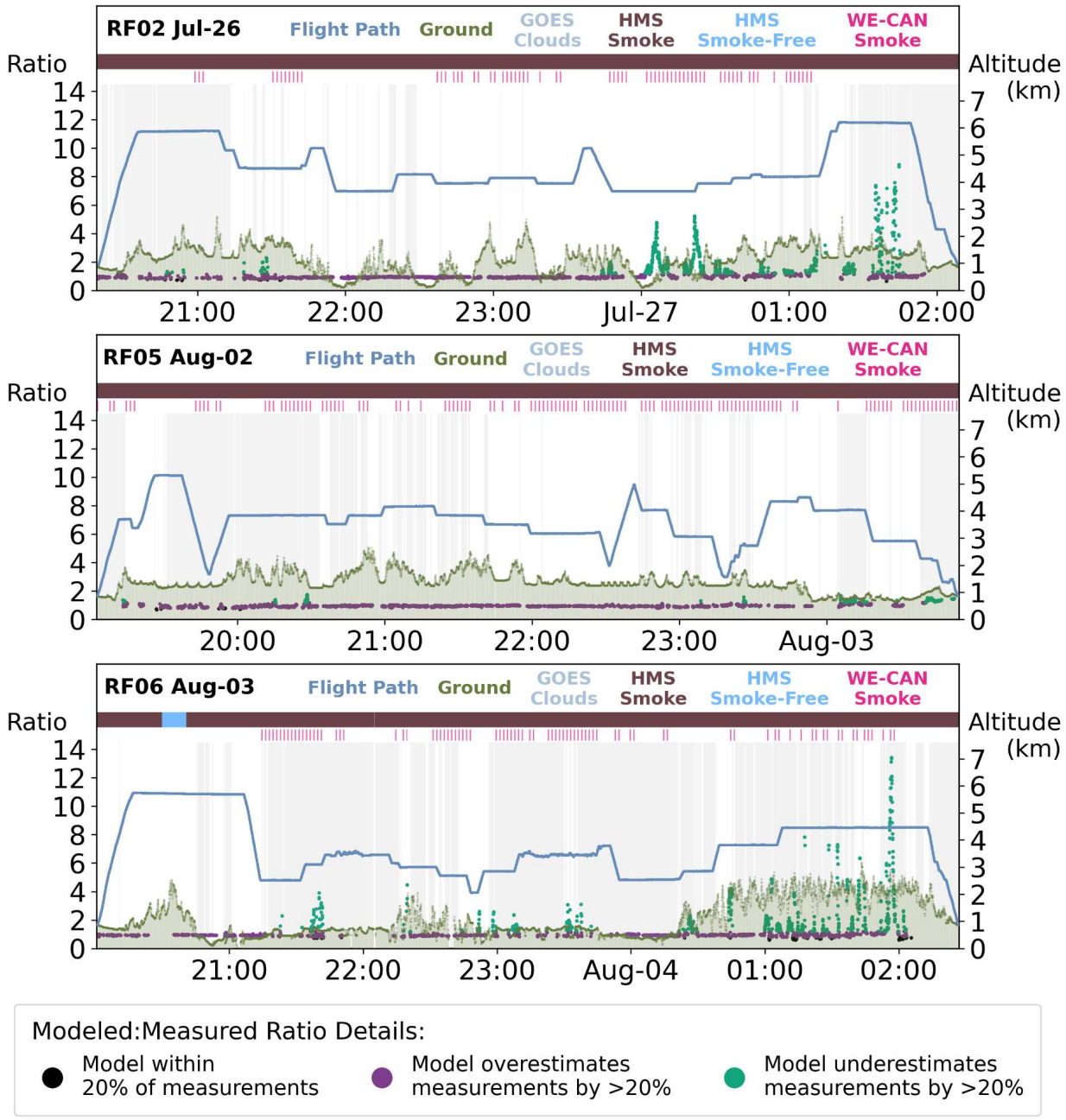

Figure A3.4: Diagram of each flight path with the altitude of the aircraft (blue) and ground (green) over time. The location of HMS smoke plumes (brown), WE-CAN smoke composition markers (pink), and clouds (grey) are indicated. The scatter points show the ratio of TUV modeled to HARP measured downwelling actinic flux at 550 nm. Points where the model agrees with the measurements to within 20% are indicated in black alongside points where large overestimates (purple) and underestimates (teal) occur.

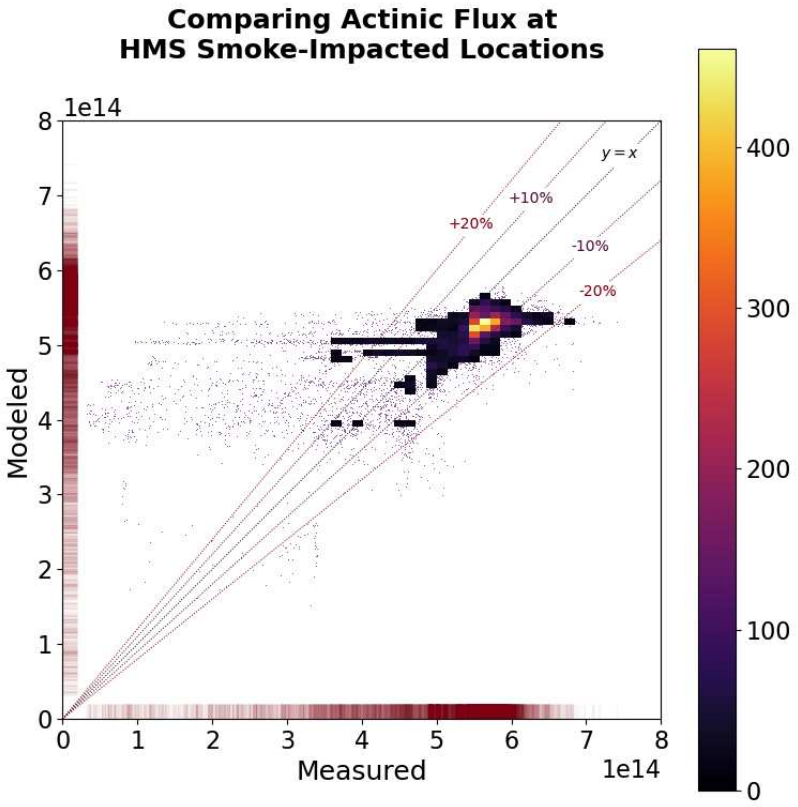

Figure A3.5: Comparison of TUV modeled and HARP measured $F\downarrow_{550}$ (photons cm^{-2} nm^{-1} s^{-1}) for the aircraft-smoke-impacted model configuration. This initial figure includes cloudy, cloud-free, smoke-impacted, and smoke-free locations along the three flight paths. Individual points are shown (purple) with an overlapping histogram heat map that indicates the point concentration in each plot position (colorbar). Rugplots (red) along the x and y axes display the distribution of measured and modeled values, respectively.

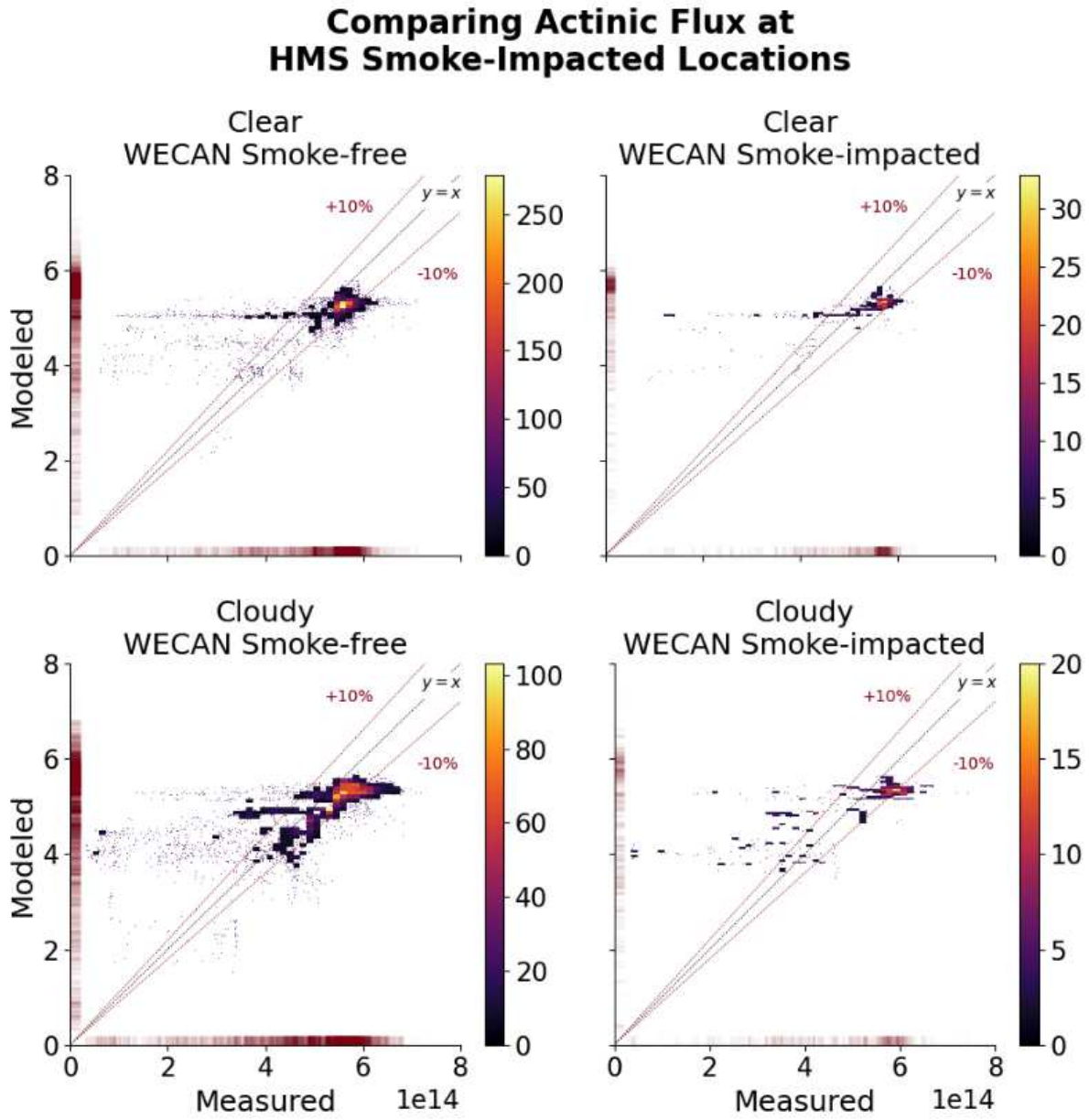

Figure A3.6: Version of Figure A3.2 that splits the visualization by smoke and cloud conditions.

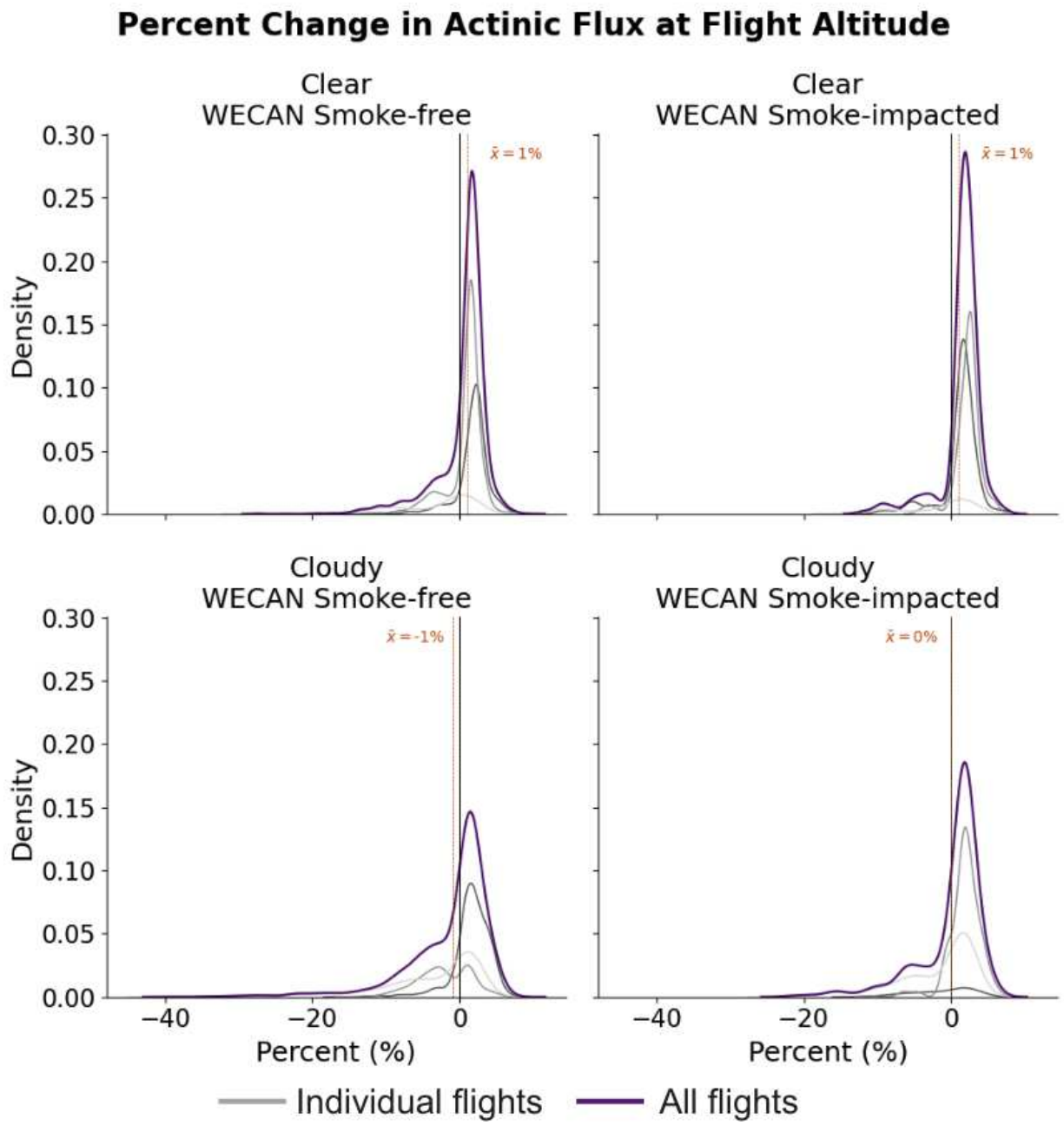

Figure A3.7: Kernel density plots of the percent change in downwelling actinic flux at 550 nm at the altitude of the aircraft due to smoke (TUV smoke-impacted minus TUV smoke-free) given different smoke (columns) and cloud (rows) conditions. Individual flights are indicated in shades of grey and the collective distribution is indicated in purple. The average percent change is recorded using a vertical orange line and corresponding text ($\bar{x}$).

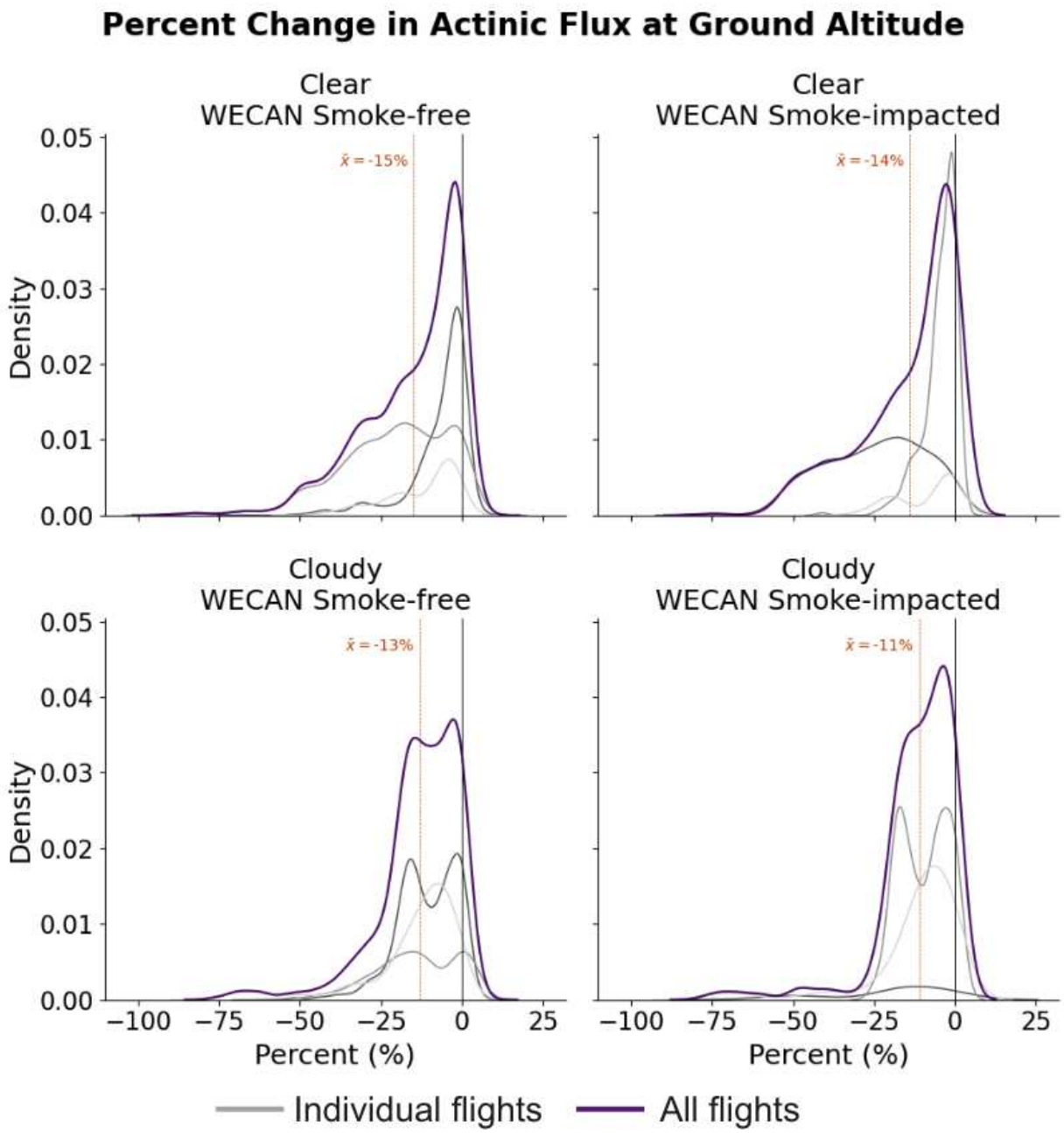

Figure A3.8: Kernel density plots of the percent change in downwelling actinic flux at 550 nm at the ground due to smoke (TUV smoke-impacted minus TUV smoke-free) given different smoke (columns) and cloud (rows) conditions. Individual flights are indicated in shades of grey and the collective distribution is indicated in purple. The average percent change is recorded using a vertical orange line and corresponding text ($\bar{x}$).

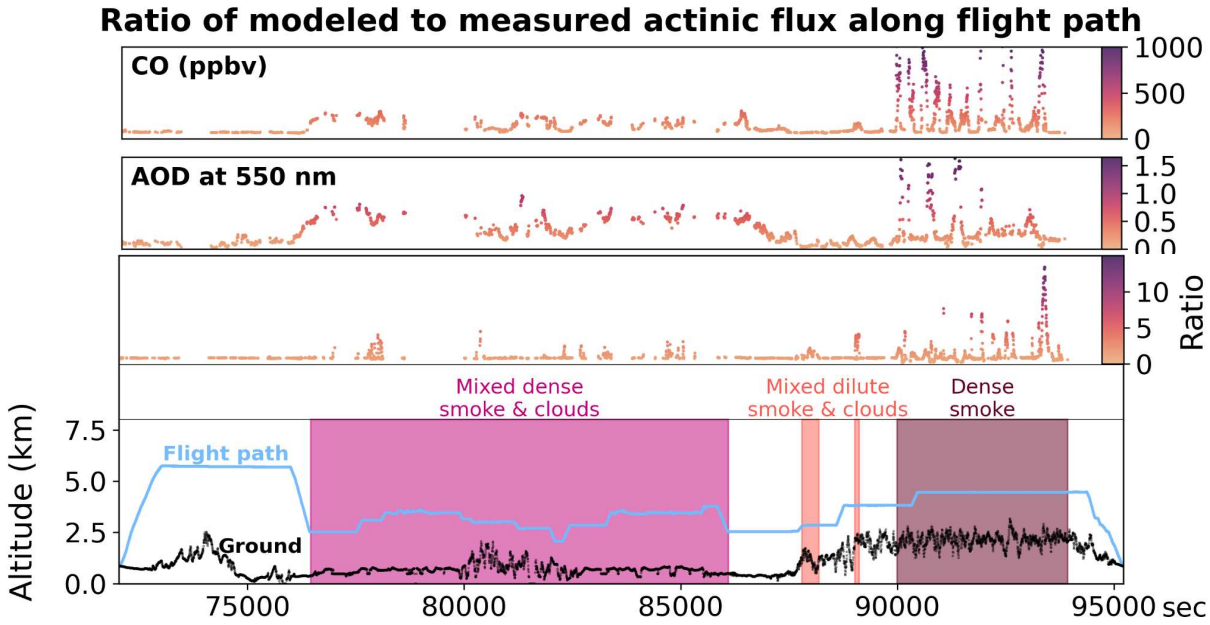

Figure A3.9: RF06 flight path (bottom row) showing the location (shaded areas) of potentially challenging conditions for aligning the TUV model output and HARP measurements. The top two plots show the change in CO concentration and AOD at 550 nm along the flight path, respectively. The third plot indicates the ratio of modeled to measured downwelling actinic flux at 550 nm.

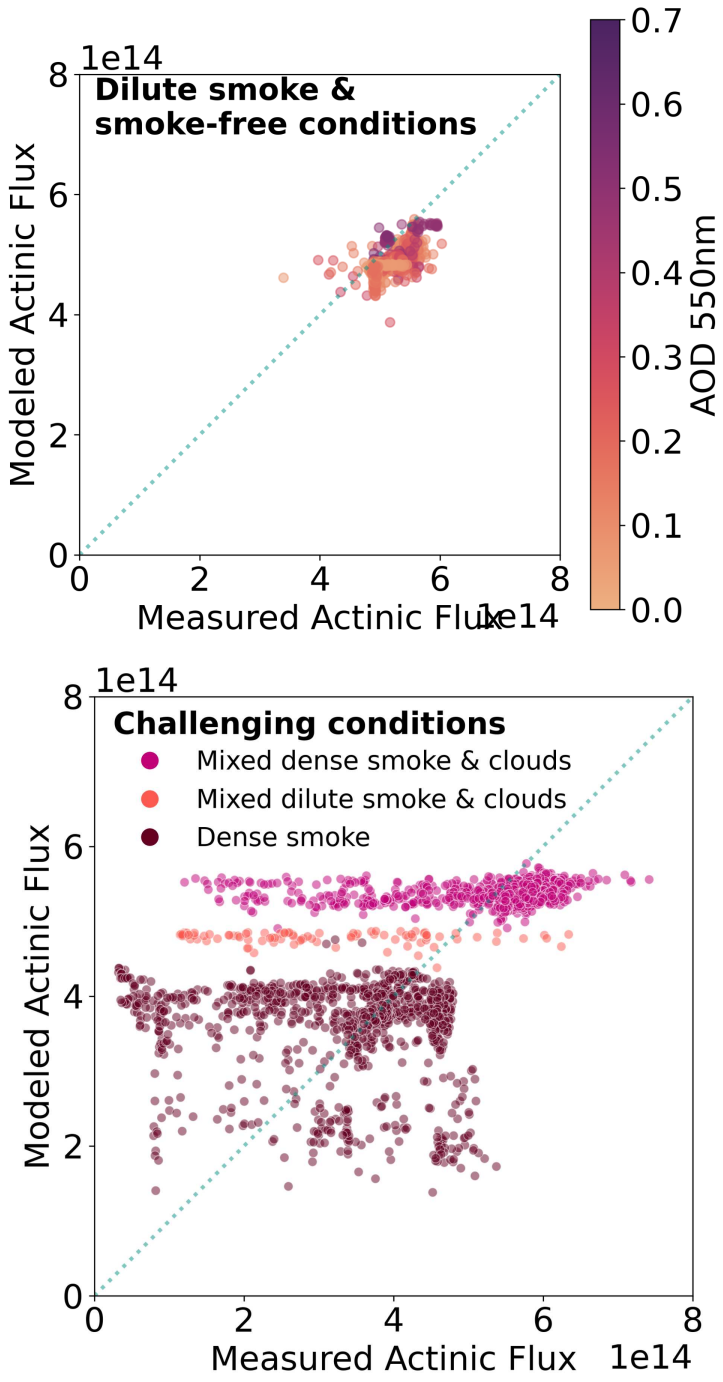

Figure A3.10: Comparison of the measured (x) and modeled (y) downwelling actinic flux at 550 nm for conditions thought to be more compatible with using TUV for this methodology (top panel) and conditions that pose challenges for modeling actinic flux with TUV (bottom panel). In the top panel, the points are colored by AOD at 550 nm, and in the bottom panel, the colors indicate the section of the flight path (matches color shading from Figure A3.6) represented by each point.

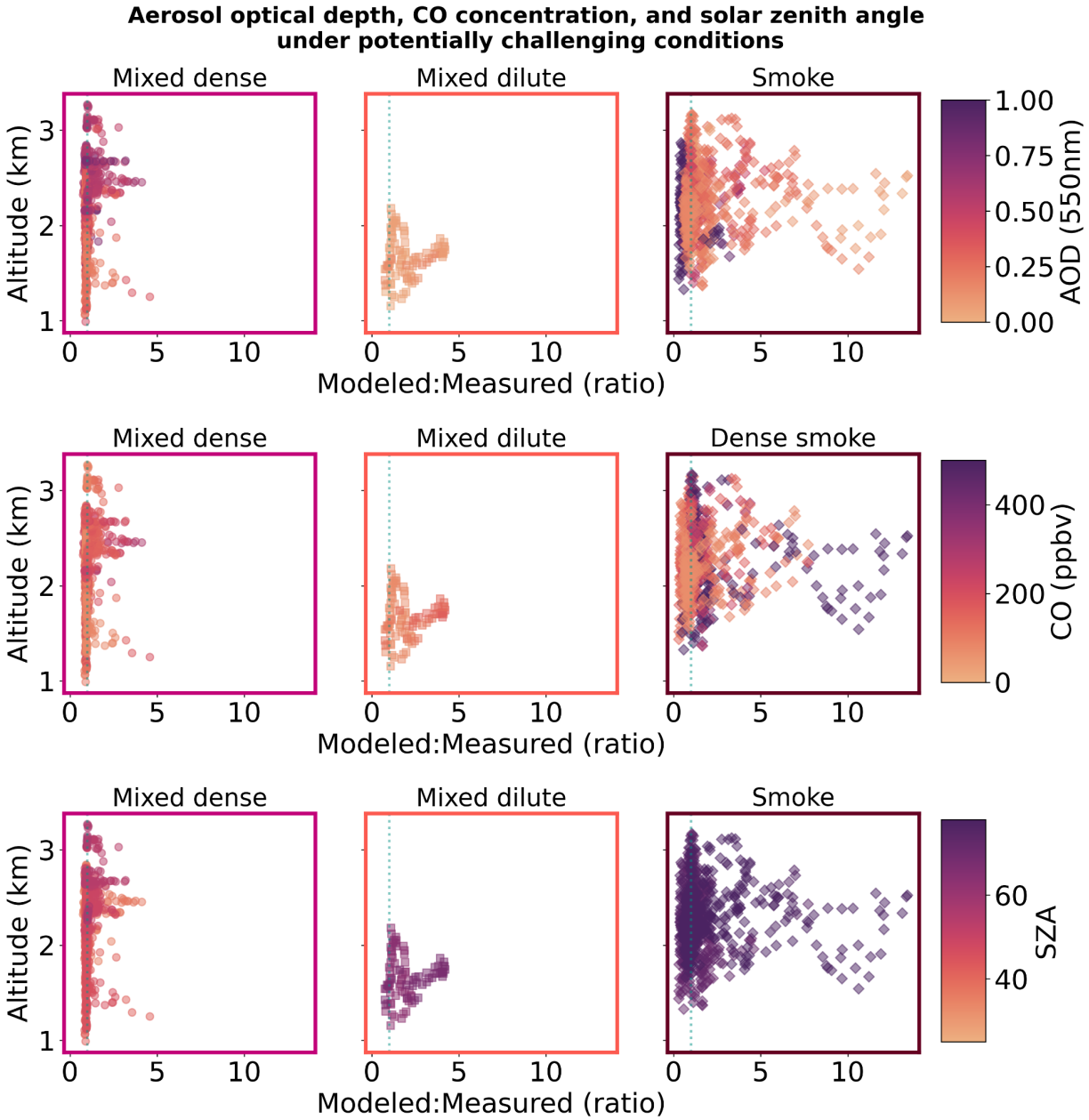

Figure A3.11: Comparison of the modeled-to-measured ratio for downwelling actinic flux at 550 nm by altitude. Columns indicate the section of the flight path represented (border color follows shading in Figure A3.6). Rows indicate the variable by which points are colored: AOD at 550 nm, CO in ppbv, and SZA.

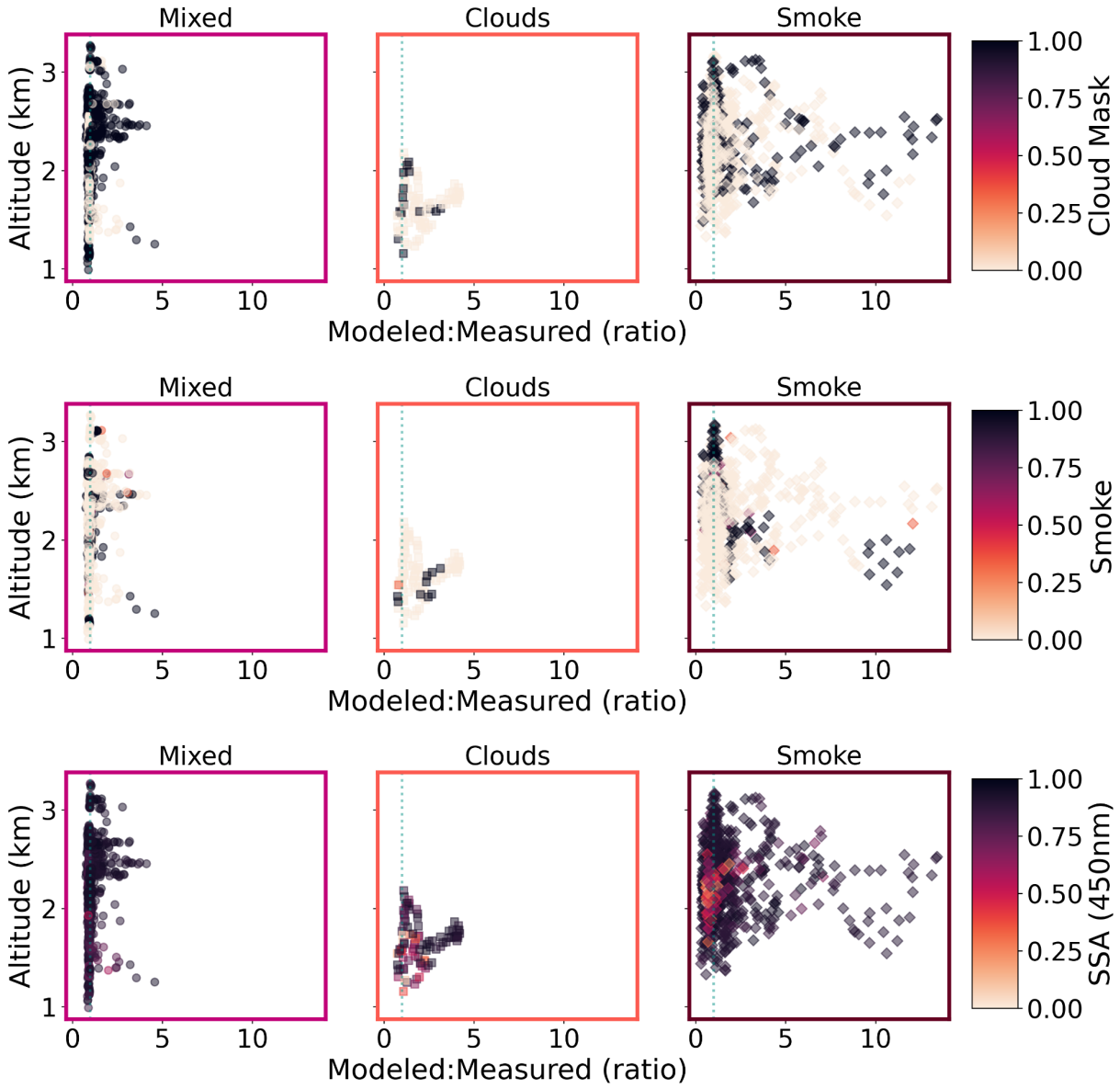

Figure A3.12: As above, comparison of the modeled-to-measured ratio for downwelling actinic flux at 550 nm by altitude. Columns indicate the section of the flight path represented (border color follows shading in Figure A3.6). Rows indicate the variable by which points are colored: GOES binary cloud mask, WE-CAN smoke flag, and SSA at 450 nm.

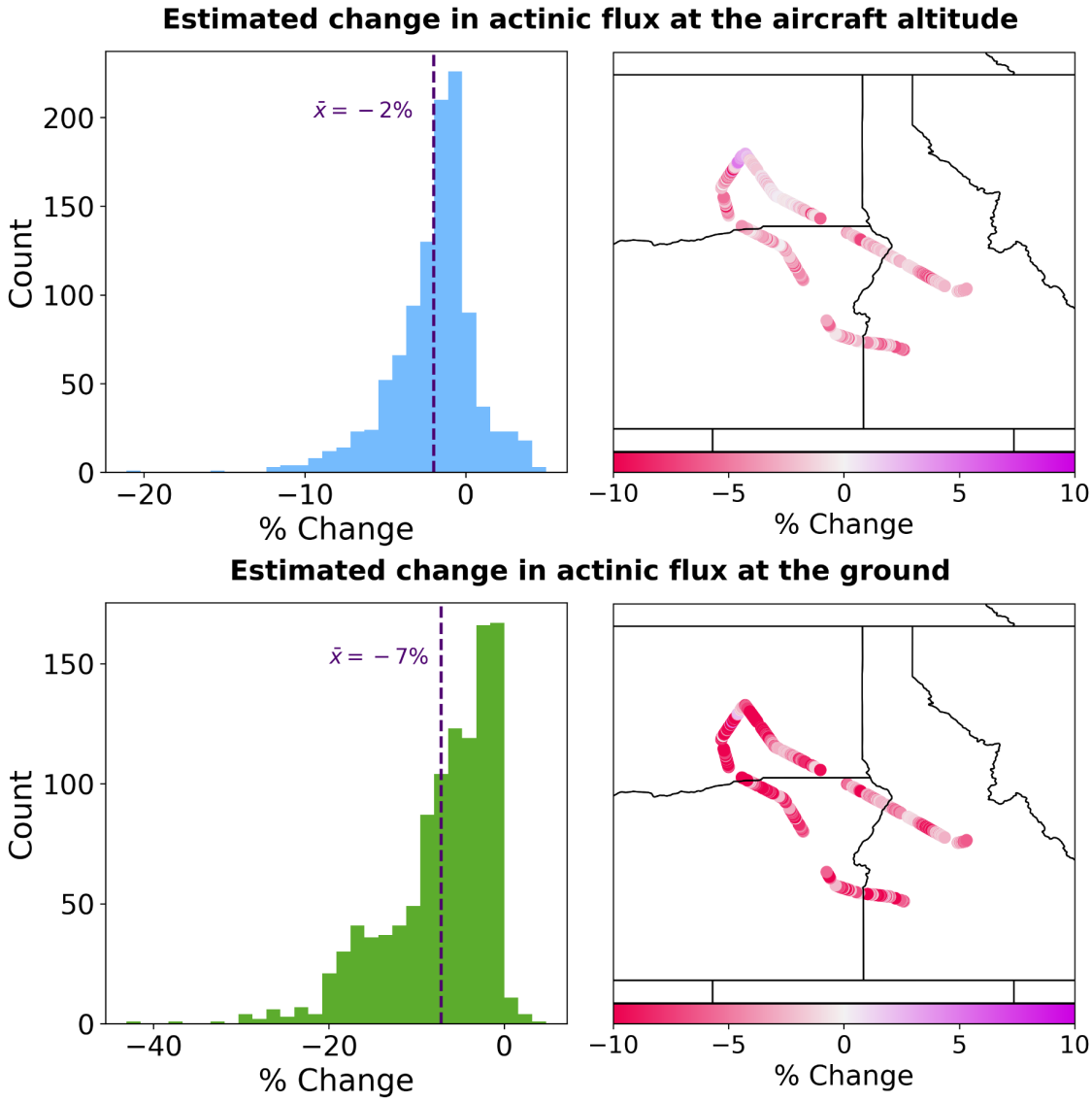

Figure A3.13: Estimated change in downwelling actinic flux at 550 nm at the altitude of the aircraft (top row) and at the ground beneath the aircraft (bottom row). The left column presents a histogram of the percent change and the right column presents the change spatially along the flight path. The average percent change is indicated by the vertical line on the histogram and associated text ($\bar{x}$).